



Copyright Undertaking

This thesis is protected by copyright, with all rights reserved.

By reading and using the thesis, the reader understands and agrees to the following terms:

1. The reader will abide by the rules and legal ordinances governing copyright regarding the use of the thesis.
2. The reader will use the thesis for the purpose of research or private study only and not for distribution or further reproduction or any other purpose.
3. The reader agrees to indemnify and hold the University harmless from and against any loss, damage, cost, liability or expenses arising from copyright infringement or unauthorized usage.

IMPORTANT

If you have reasons to believe that any materials in this thesis are deemed not suitable to be distributed in this form, or a copyright owner having difficulty with the material being included in our database, please contact lbsys@polyu.edu.hk providing details. The Library will look into your claim and consider taking remedial action upon receipt of the written requests.

**NON-VOLATILE FIELD EFFECT MODULATION
OF MAGNETISM IN DILUTE MAGNETIC OXIDE
THIN FILMS**

WONG HON FAI

PhD

The Hong Kong Polytechnic University

2018

The Hong Kong Polytechnic University
Department of Applied Physics

**Non-volatile Field Effect Modulation of Magnetism in
Dilute Magnetic Oxide Thin Films**

Wong Hon Fai

A thesis submitted in partial fulfillment of the
requirements for the degree of Doctor of Philosophy

November 2017



Certificate of originality

I hereby declare that this thesis is my own work and that, to the best of my knowledge and belief, it reproduces no material previously published or written, nor material that has been accepted for the award of any other degree or diploma, except where due acknowledgement has been made in the text.

WONG Hon Fai



Abstract

In this work I studied the electric-field manipulation of transport and magnetic properties in $\text{La}_{0.66}\text{Sr}_{0.33}\text{MnO}_3$ (LSMO) and $\text{Zn}_{0.92}\text{Mn}_{0.08}\text{O}$ thin films, through the geometry of field-effect transistors. In such field-effect devices, the application of electric field through the gate dielectric attracts or repels charge carriers in the ferromagnetic channel, leading to charge accumulation and depletion at the gating interfaces and hence modulating the transport and magnetic properties of the channel layer. Usually the strength of modulation depends on the thickness of the ferromagnet and the electrostatic screening depth within the channel. In this thesis, the modulation of magnetic properties in the ferromagnetic layer, as induced by the application of gate voltage via ferroelectric polymer or ionic liquid gating, were described.

Several related investigations were performed in this thesis. Firstly, the electric-field manipulation of carrier transport and magnetism in the LSMO (7.5 nm) channel was studied, using ferroelectric copolymer of poly[(vinylidene fluoride-co-trifluoroethylene)] [P(VDF-TrFE)] as the dielectric gate. Upon the polarization reversal of P(VDF-TrFE), the LSMO channel exhibited a 15 % change in resistance at room temperature (and less than 1% change at 20 K). Experimental results in the resistance-temperature (R - T) measurement showed insignificant change of Curie Temperature (T_C) of LSMO upon switching the polarization direction of P(VDF-TrFE), which was attributed to the short screening depth in the LSMO channel.

Apart from controlling the LSMO behavior by reversal of P(VDF-TrFE) polarization, electric-field manipulation of the transport and magnetic properties of LSMO films was also examined through the application of low-voltage pulse chains across the P(VDF-TrFE) gate, using the same device structure. With the increase of positive-pulsing cycles from 0 to 36 k, the LSMO channel exhibited a gradual decrease in T_C from 280 K to 265 K and showed suppression of low-field magnetoresistance at 20 K. The results also indicated that T_C and magnetoresistance at 20 K could be reversibly controlled through the application of gate pulses of different polarities, as well as the number of pulses applied. X-ray photoelectron spectroscopy (XPS) and transport measurements in the LSMO channel under different gas environment revealed that low electric-field pulse switching with positive gate pulses favored oxygen vacancy (O_v) creation in LSMO layer



under vacuum environment, while the O_v annihilation in LSMO channel was more favorable under oxygen environment. By comparing the pristine and gated samples, a change in the ratio between Mn^{3+} and Mn^{4+} ions was observed. Such results indicated that the manipulation of transport and magnetic properties in LSMO during the low-voltage-pulse cycles were due to electrochemical reactions (namely O_v creation/annihilation) in the LSMO, rather than electrostatic accumulation or depletion of charge carriers.

The final study involved the electric-field manipulation of transport and magnetic properties in the dilute magnetic semiconductor (DMS) of $Zn_{0.92}Mn_{0.08}O$, using an electric-double-layer gating through ionic liquid. In addition to modulation of ZnO channel resistance, the electrostatically-controlled $Zn_{0.92}Mn_{0.08}O$ films exhibited a tunable magnetoresistance below 100 K, indicating that the application of gate voltage effectively manipulated the charge carriers of the ZnO channel. Moreover, anomalous Hall effect measurements revealed an enhanced ferromagnetic state as the gate voltage switched from -2V to 2V, thereby indicating the controllable electron carrier density also altered the ferromagnetism in the material.



Scholarly activities

Journal publications

1. 'Nanopatterned L₁₀-FePt nanoparticles from single-source metallopolymer precursors for potential application in ferromagnetic bit-patterned media magnetic recording', Z.G. Meng, G.J. Li, S.M. Ng, **H.F. Wong**, S.C. Yiu, C.L. Ho, C.W. Leung and W.Y. Wong, *Polymer Chem.* 7, 4467 (2016).
2. 'WS₂ nanotube formation by sulphurization: Effect of precursor tungsten film thickness and stress', S.M. Ng, **H.F. Wong**, W.C. Wong, C.K. Tan, S.Y. Choi, C.L. Mak, G.J. Li, Q.C. Dong and C.W. Leung, *Mater. Chem. Phys.*, 181, 352 (2016).
3. 'Patterning of L₁₀ FePt nanoparticles with ultra-high coercivity for bit-patterned media', Z.G. Meng, G.J. Li, **H.F. Wong**, S.M. Ng, S.C. Yiu, C.K. Lam, C.W. Leung, I. Manners and W.Y. Wong, *Nanoscale*, 9, 731 (2017).
4. 'Structural, magnetic and transport properties of fully epitaxial LaMnO₃/LaAlO₃ multilayers', Y.K. Liu, **H.F. Wong**, S.Z. Huang, S.X. Hu, S.M. Ng, K.K. Lam, C.L. Mak and C.W. Leung, *Mater. Lett.*, 205, 230 (2017).
5. 'Effect of Post-Annealing on Sputtered MoS₂ films', W.C. Wong, S.M. Ng, **H.F. Wong**, W.F. Cheng, C.L. Mak and C.W. Leung, *Solid St. Electron.* 138, 62 (2017).
6. 'Enhanced Tunability of Electrical and Magnetic Properties in (La,Sr)MnO₃ Thin Films via Field-assisted Oxygen Vacancy Modulation', **H.F. Wong**, S.M. Ng, W.F. Cheng, Y.K. Liu, X.X. Chen, D. von Nordheim, C.L. Mak, J.Y. Dai, B. Ploss and C.W. Leung, *Solid St. Electron.* 138, 56 (2017).
7. 'Spin-Valve Junction with Transfer-Free MoS₂ Spacer Prepared by Sputtering', W.C. Wong, S.M. Ng, **H.F. Wong**, C.L. Mak and C.W. Leung, *IEEE Trans. Magn.* 53, 1600205 (2017).
8. 'Magnetotransport properties of Ca_{0.8}La_{0.2}IrO₃ epitaxial films', Y.K. Liu, **H.F. Wong**, S.M. Ng, K.K. Lam, C.L. Mak and C.W. Leung, *Mater. Lett.* 213, 135 (2018).
9. 'A ferroelectric relaxor polymer-enhanced p-type WSe₂ transistor', C. Yin, X.D. Wang, Y. Chen, D. Li, T. Lin, S. Sun, H. Shen, P.Y. Du, J.L. Sun, X.J. Meng, J.H. Chu, **H.F. Wong**, C.W. Leung, Z.R. Wang and J.L. Wang, *Nanoscale*, 10, 1727 (2018).
10. 'Percolative multi-susceptible PVDF/NZFO composite films with triply controlled high dielectric and magnetic properties', W. J. Zhao, J.Q. Gong, **H.F. Wong**, Z.R. Wang, C.W. Leung, N. Ma, and P.Y. Du, *J. Appl. Phys.*, 123, 104104 (2018).
11. 'Effect of post-annealing on laser-ablation deposited WS₂ thin films', H. Wang, S.M. Ng, **H.F. Wong**, W.C. Wong, K.K. Lam, Y.K. Liu, L.F. Fei, Y.B. Zhou, C.L. Mak, Y. Wang, C.W. Leung, *Vacuum*, 152, 239 (2018).



12. 'Raman studies of MoS₂ under strain at different uniaxial directions', C.K. Tan, W.C. Wong, S.M. Ng, **H.F. Wong**, C.W. Leung and C.L. Mak, *Vacuum*, 153, 274 (2018).
13. Gate-controlled Transport Properties in Dilute Magnetic Semiconductor (Zn, Mn)O Thin Films', **H.F. Wong**, S.M. Ng, Y.K. Liu, K.K. Lam, K.H. Chan, W.F. Cheng, D. von Nordheim, C.L. Mak, B. Ploss and C.W. Leung, accepted by *IEEE Trans. Magn.*
14. "Anomalous Hall effect in Pt/Tb₃Fe₅O₁₂ heterostructure: Effect of Compensation Point", Y.K. Liu, **H.F. Wong**, K.K. Lam and C.W. Leung, accepted by *J. Magn. Mater.*
15. "Edge decoration of MoS₂ monolayer with ferromagnetic CoFe nanoparticles", Z.G. Meng, Ho, C.L. Ho, G.J. Li, S.M. Ng, **H.F. Wong**, C.W. Leung, W.Y. Wong, accepted by *Materials Research Express*.
16. "Lithographic patterning of ferromagnetic FePt nanoparticles from a single-source bimetallic precursor containing hemipharmidic structure for magnetic data recording media", Z.G. Meng, Ho, C.L. Ho, **H.F. Wong**, Z.Q. Yu, N.Y. Zhu, G.J. Li, C.W. Leung, W.Y. Wong, accepted by *Science China Materials*.
17. 'Electric field-induced oxygen vacancy modulation in perovskite manganite films gated with ferroelectric polymer' **H.F. Wong**, S.M. Ng, Y.K. Liu, Z.G. Meng, L.F. Fei, K.K. Lam, K.H. Chan, W.F. Cheng, D. von Nordheim, C.L. Mak, B. Ploss, C.L. Ho, W.Y. Wong and C.W. Leung, in preparation.
18. 'Electrical control of transport and magnetic properties in dilute magnetic semiconductor Mn:ZnO thin films' **H.F. Wong**, S.M. Ng, Y.K. Liu, Z.G. Meng, L.F. Fei, K.K. Lam, K.H. Chan, W.F. Cheng, C.L. Mak, C.L. Ho, W.Y. Wong, A. Ruotolo and C.W. Leung, in preparation.

**Conference presentations or posters**

1. S.M. Ng, **H.F. Wong**, W.C. Wong, C.K. Tan, G.J. Li, S.Y. Choi, Q.C. Dong, C.L. Mak and C.W. Leung, 'Controlled Growth of Tungsten Disulphide Nanostructures', *2nd International Conference on Two-dimensional Layered Materials (2DLM) 2016, Hong Kong, 2016*
2. W.C. Wong, S.M. Ng, **H.F. Wong**, W.F. Cheng, C.L. Mak and C.W. Leung, 'Spin-Valve Junction with Transfer-Free MoS₂ Spacer Prepared by Sputtering' *IEEE International Magnetic conference Intermag 2017, Dublin, Ireland, 2016*
3. C.K. Tan, W.C. Wong, S.M. Ng, **H.F. Wong**, C.W. Leung and C.L. Mak, 'Raman Response of MoS₂ in different strained direction', *2017 IEEE Electron Devices and solid-state Circuits, Hsinchu, Taiwan, 2017*
4. H. Wang, S.M. Ng, **H.F. Wong**, W. C. Wong, K.K. Lam, Y.K. Liu, L.F. Fei, C.L. Mak, Y. Wang and C.W. Leung, 'Effect of post-annealing on laser-ablation deposited WS₂ thin films', *2017 IEEE Electron Devices and solid-state Circuits, Hsinchu, Taiwan, 2017*
5. **H.F. Wong**, S.M. Ng, Y.K. Liu, K.K. Lam, K.H. Chan, W.F. Cheng, D. von Nordheim, C.L. Mak, B. Ploss and C.W. Leung, 'Gate-controlled Transport Properties in Dilute Magnetic Semiconductor (Zn, Mn)O Thin Films', *IEEE International Magnetic conference Intermag 2018, Singapore, 2018*



Acknowledgements

This work cannot be possible without the help and supports of many people during my three years of Ph.D. studies. I would like to express my sincere gratitude, Dr. C.W. Leung, for his guidance and supervision throughout my studies. His insight and attitudes towards difficulties provides many possible directions in my research and even life. I would like to thank, Dr. C.L. Mak, for fruitful discussion on my research.

I would like to thank Mr. W.F. Cheung for his help to write several LabVIEW programs to perform the magneto-transport measurements in the magnetoelectricity laboratory. Dr. S. M. Ng has inspired and helped me on the fabrication and characterization of magnetic heterostructure and the research work. Dr. N.Y. Chan helped and assisted in equipment operation in the Department of Applied Physics. I would like to express my appreciations towards colleagues in PLD group, Dr Y.K. Liu, Dr. L.F. Fei., Mr. K.K. Lam, Mr. K.H. Chan, Mr. W.H. Fung and Ms. H. Wang.

I wish to thank Prof. Raymond W.Y. Wong, Dr C.L. Ho, and Dr. Z.G. Meng, of Department of Chemistry in Hong Kong Baptist University for the help in XPS measurement. And I would like to thank my friends and colleagues in AP for their help and assistances: Dr. K. Wang, Dr Y.Y. Hui, Mr. M.H. Wong, Mr. K.H. Chou, Ms. S.K. Lai and Mr. F. Zhang.

Last but not least, I would like to thank my parents, for their love and endless support throughout my life.



List of acronyms

Acronyms	Description
PLD	Pulsed laser deposition
XRD	X-ray diffraction
XRR	X-ray reflectivity
FET	Field-effect transistor
PMN-PT	$\text{Pb}(\text{Mg}_{1/3}\text{Nb}_{2/3})\text{O}_3\text{-PbTiO}_3$
FWHM	Full-width-half maximum
AFM	Atomic force microscopy
PFM	Piezoelectric force microscopy
RIE	Reactive ion etching
VSM	Vibration sample magnetometer
AHE	Anomalous hall effect
2D	Two-dimensional
STO	Strontium titanate, SrTiO_3
LAO	Lanthanum aluminate, LaAlO_3
LSMO	Lanthanum strontium manganite, $\text{La}_{0.66}\text{Sr}_{0.33}\text{MnO}_3$
$\text{Zn}_{0.92}\text{Mn}_{0.08}\text{O}$	Manganese doped zinc oxide
PZT	Lead zirconate titanate, $\text{Pb}(\text{Zr,Ti})\text{O}_3$
BTO	Barium titanate, BaTiO_3
HfO ₂	Hafnium oxide
Al ₂ O ₃	Aluminum oxide
SiO ₂	Silicon oxide
MgO	Magnesium oxide
ZrO ₂	Zirconium oxide
P(VDF-TrFE)	copolymer of poly[(vinylidene fluoride-co-trifluoroethylene)]
IL	Ionic liquid
BHF	Buffered hydrofluoric acid



DI	Deionized water
EDL	Electric-double layer
EDLT	Electric-double-layer transistor
T_C	Metal-to-insulator transition
R_{xx}	Longitudinal resistance
ρ_{xx}	Longitudinal resistivity
η	Carrier concentration
μ_e	Electron mobility
ρ_{xy}	Transverse resistivity
ρ_{AHE}	Anomalous resistivity
ρ_{OHE}	Ordinary hall resistivity
σ_{AHE}	Anomalous hall conductivity
MR	Magnetoresistance
AMR	Anisotropic magnetoresistance
AHE	Anomalous hall effect
V_g	Gate voltage
H_c	Coercivity
B	applied magnetic field with in-plane direction
B_z	applied magnetic field with out-of-plane direction
T	Temperature



Table of contents

Certificate of originality	2
Abstract.....	3
Scholarly activities	5
Journal publications.....	5
Conference presentations or posters.....	7
Acknowledgements	8
List of acronyms	9
Table of contents	11
List of figures.....	14
List of tables.....	18
Chapter 1 Introduction.....	19
1.1 Background and objectives	19
1.2 Signification of this work.....	21
1.3 Outline of thesis	21
References for Chapter 1.....	23
Chapter 2 Literature review	26
2.1 Manganites.....	26
2.1.1 Crystallographic structure of manganites.....	26
2.1.2 Electronic structure and Jahn-Teller distortion.....	27
2.1.3 Double-exchange coupling	28
2.1.4 Super-exchange coupling	29
2.1.5 $\text{La}_{1-x}\text{Sr}_x\text{MnO}_3$ phase diagram	30
2.2 Zinc oxide	31
2.2.1 Crystal structure.....	31
2.2.2 Diluted magnetic semiconductor	32
2.2.3 Donor impurity-band exchange model	33
2.3 Electric-field manipulation of magnetism.....	33
2.3.1 Electrostatics doping	35
2.3.2 Electrochemical reaction.....	39
2.3.3 Exchange coupling.....	43
2.3.4 Strain coupling.....	44
2.3.5 Orbital reconstruction.....	46



2.1 Conclusion.....	48
References for Chapter 2.....	49
Chapter 3 Experimental techniques.....	52
3.1 Substrate surface treatment	52
3.1.1 Strontium titanate substrates	52
3.2 Pulsed laser deposition.....	53
3.2.1 Unique characteristics of pulsed laser deposition.....	54
3.2.2 Thin film growth modes	55
3.2.3 Thin film growth conditions in this project.....	56
3.2.4 Target fabrication.....	57
3.3 Device fabrication.....	58
3.3.1 Fabrication of LSMO field-effect devices.....	58
3.3.2 Fabrication of $Zn_{0.92}Mn_{0.08}O$ devices	59
3.4 Thin film characterization techniques.....	61
3.4.1 X-ray diffraction	61
3.4.2 Atomic force microscopy.....	63
3.4.3 X-ray photoelectron spectroscopy.....	63
3.4.4 Transmission electron microscopy	64
3.4.5 Vibrating sample magnetometer	66
3.4.6 Hall effect measurements	66
3.4.7 Anomalous hall effect	68
3.4.8 Physical property measurement system	69
3.4.9 Magnetoresistance	69
3.5 Conclusion.....	69
References for Chapter 3.....	70
Chapter 4 Electric-field manipulation of magnetism in the multiferroic heterostructure of $La_{0.66}Sr_{0.33}MnO_3/P(VDF-TrFE)$.....	71
4.1 Introduction	71
3.2 Experimental details	72
4.1 Results and discussions	74
4.1.1 Structural characterization	74
4.1.2 Transport and magnetic characterization.....	76
4.1.3 Conclusion	79
References for Chapter 4.....	80



Chapter 5 Electric field-induced oxygen vacancy modulation in perovskite manganite Films gated with ferroelectric polymer	82
5.1 Introduction	82
5.2 Experimental details	84
5.2.1 Thin film growth and device fabrication	84
5.2.2 Structural characterization	84
5.2.3 Electrical and magnetic measurements	84
5.3 Results and discussions	85
5.3.1 Structural and ferroelectric characterization	85
5.3.2 Transport characterization.....	87
5.4 Conclusion.....	97
References for Chapter 5.....	98
Chapter 6 Electrical control of the transport and magnetic properties in diluted magnetic oxide of $Zn_{0.92}Mn_{0.08}O$	101
6.1 Introduction	101
6.2 Experimental details	102
6.2.1 Thin film growth and device fabrication.....	102
6.2.2 Structural characterization	103
6.2.3 Transport characterization.....	103
6.3 Results and discussions	104
6.3.1 Structural characterization	104
6.3.2 Transport characterization.....	107
6.3.2 Magnetic characterization	113
6.4 Conclusion.....	117
References for Chapter 6.....	118
Chapter 7 Conclusions and future work.....	120
7.1 Summary of results	120
7.2 Future directions	121
References for Chapter 7.....	122



List of figures

- Figure 2. 1 Left: crystallographic structure of LaMnO_3 perovskite. Right: schematics illustration of cubic perovskite structure [1]. 27
- Figure 2. 2 Schematics illustration of energy levels of Mn^{3+} free ions and Mn^{3+} in oxygen octahedron. Taking manganite as a case, the Hund's rule is stronger than crystal field splitting. The Jahn-Teller effect lifts the degeneracy of e_g level and results in elongation of MnO_6 axial direction. The right side shows the five 3d orbitals (three t_{2g} orbitals and two e_g orbitals) [2]. 28
- Figure 2. 3 Schematic illustration of double exchange mechanism in $\text{Mn}^{3+}\text{-O-Mn}^{4+}$ and $\text{Mn}^{4+}\text{-O-Mn}^{3+}$ [4]. 29
- Figure 2. 4 (a) Phase diagram of $\text{La}_{1-x}\text{Sr}_x\text{MnO}_3$ bulk crystals with different Sr doping concentration x [8]. (b) Temperature dependence of resistivity for different Sr doping concentration (x) of $\text{La}_{1-x}\text{Sr}_x\text{MnO}_3$ bulk crystals. Arrows and open triangles indicated the T_C and structural changes from rhombohedral to orthorhombic [7]. 31
- Figure 2. 5 Crystal structures of common ZnO allotropes: (a) rocksalt, (b) zincblende and (c) hexagonal wurtzite. Large and small circles indicate oxygen and zinc atoms, respectively [9]. 32
- Figure 2. 6 Computed Curie temperatures for different p-type semiconductors [12]. 32
- Figure 2. 7 Schematics illustration of bound magnetic polarons. In the presence of magnetic field, O_v form the polarons. The overlap of polarons results in long-range ferromagnetic ordering. The squares represent O_v of ZnO lattice and black circles represented the magnetic ions [13]. 33
- Figure 2. 8 (a) Electric-field manipulation of hole-induced ferromagnetism in DMS $(\text{In,Mn})\text{As}$ FET. (b) AHE measurements ($R_{\text{AHE}}\text{-H}$ curve) under different V_g of 125, 0 and -125 V. (c) Temperature dependence of R_{AHE} under different V_g , R_{AHE}^2 is proportional to the magnetization of $(\text{In,Mn})\text{As}$ [25]. 35
- Figure 2. 9 The left hand side is the schematics illustration of energy band diagram for ZnO under different bias electric fields. Positive gate electric field results in the enhancement of ferromagnetic interaction between Co ions (increase electron carrier concentration), whereas negative gate electric field results in the suppression of ferromagnetic interaction (decrease electron carrier concentration). The right side is the field dependence of anomalous Hall resistance (R_{AHE}) for various electric fields (5, 0 and -5 MV/cm), measured at 4 K. Clear hysteresis loop appeared as the positive gate electric field was applied [15]. 36
- Figure 2. 10 (a) Schematics illustration of the electric-field manipulation in perpendicularly magnetized Co/Pt devices. (b) The field dependence of R_{AHE} measured at 290 K. (d)-(k) Movement of domain-wall as observed by MOKE microscope after a single domain was produced by the application of large negative H. A magnetic field of 170 Oe was applied at $t = 0$ s, for the nucleation of a domain wall. After that, the magnetic field was reduced to 120 Oe. The image shows the domain-wall creep motion as it prorogates from left to right [30]. 37
- Figure 2. 11 Temperature dependence of LBMO channel resistivity with different ferroelectric polarization reversal in PZT for (a) $x=0.10$ and (b) $x=0.15$. (c) Plot of T_C modulation against the value of ferroelectric remnant polarization with $x=0.1$ (white circle) and $x=0.15$ (black circle). The inset shows the plot of change in channel resistance against the value of ferroelectric remnant polarization, and the linear fit indicates the trend line [33]. 38
- Figure 2. 12 Schematics illustration of LCMO field-effect devices gated with EDL, (a) for the application of position gate voltage. (b) the top view of devices. (c) temperature dependence of 5 nm-thick LCMO sheet resistance gated with ionic liquid with different V_g (3 V: blue line, 0 V: black line and -3 V: red line) [35]. 39
- Figure 2. 13 (a) Phase diagram of $\text{La}_{1-x}\text{Sr}_x\text{MnO}_3$ with different Sr doping concentration (x), where the abbreviations are spin-canted insulating (CI), ferromagnetic insulating (FI), ferromagnetic metal (FM), antiferromagnetic metal (AFM), antiferromagnetic insulating (AFI), paramagnetic insulating (PI), and paramagnetic metal (PM) phases. (b) Temperature dependence of LSMO channel resistance as a function of V_g (c) Fourier-filtered images of LSMO sample with the application of $V_g=3\text{V}$. \perp and dashed ovals highlights the dislocations sites and regions with high dislocation densities, respectively. (d) to (f): MR (left axis) and normalized magnetization (right



- axis) recorded with sweeping magnetic fields along the LSMO channel direction under different V_g : (d) 2.5 V, (e) 3 V and (f) 3.2V [37]. 41
- Figure 2. 14 (a) Temperature dependence of 4 nm-thick SRO thin with different V_g of -2.5, 0, 2.5 and 3 V, (b) Temperature dependence of MR ($\Delta\rho$), which is obtained in 0.5 T with different V_g . The inset is the semi-log plot of data, where TFM is defined as the metal-to-insulator temperature of SRO [38]. 42
- Figure 2. 15 (a) Schematic illustration of Co/GdO_x field-effect devices. (b) AHE measurements (R_{AHE} -H curve) of the Co devices in the as-deposited state and after holding at 200 °C for 10 mins, which are indicated as black and red lines, respectively. (c) AHE measurements (R_{AHE} - B) of the Co devices after the application of electric field of -625 kV/cm for 6 mins (blue line) and +625kV/cm (purple line) for 13 mins at 200 °C. The red line is the same as in (b). Planar Hall effect (R_{AHE} - B) measurement with the magnetic field parallel to the applied current direction [39]. 42
- Figure 2. 16 (a) Normalized hysteresis loop of Cr₂O₃ (111)/Pt (0.5 nm)/[Co (0.3 nm)/Pt (1.5 nm)]₃ Pt (1.5 nm) recorded after field-cooling process (0.6 T, E=0), which is measured from 350 to 298 K (labelled as (1)), and after field-cooling process to 250 K (0.6 T, E= -500 kV/m) and (0.6 T, E=500 kV/m) (labelled as (2) and (3), respectively). (b) and (c) Schematics illustrations of Cr₂O₃ (111)/(Co/Pt)₃ with field cooling (Hfr), showing different polarities of electric field on Cr₂O₃ ($\pm Efr$), order parameter (M, I \pm) and magnetic moment in FM and AFM (SFM, SAF) where AF is single domains after magnetoelectric switching and field cooling process [41]. 43
- Figure 2. 17 (a) Schematics diagram of BFO/La_{0.7}Sr_{0.3}MnO₃ field-effect devices. (b) Temperature dependence of sheet resistance with different ferroelectric directions of BFO. (c). Changes in sheet resistance as a function of V_g measured at 180 K. (d) Magnetoresistance measurement after field-cooling process with 1 T, and measured at 180 K. Two distinct exchange-bias states were observed after switching the ferroelectric direction of BFO [42]. 44
- Figure 2. 18 (a) Relationship between in-plane strain of (001) oriented PMN-PT with x=0.28 and applied electric field along [001] direction. (b) Magnetization of LSMO at T = 330 K against electric field along [001] direction. (c) Magnetization of LSMO against in-plane strain. (d) TC of LSMO as a function of applied electric field. (e) TC of LSMO as a function of in-plane strain [46]. 45
- Figure 2. 19 (a) Change of Zn_{0.96}Mn_{0.04}O resistance with bipolar electric field applied across Zn_{0.96}Mn_{0.04}O/PMN-PT heterostructure. (b) Non-volatile behavior in resistance-switching effect of Zn_{0.96}Mn_{0.04}O/PMN-PT heterostructure by the application of pulse voltages. (c) Magnetic hysteresis loops of the Zn_{0.96}Mn_{0.04}O films after subtracting the background from the substrate; the red and blue lines are loops switched with positive and negative polarization direction respectively. The upper inset is M-H loop without subtracting contribution from the substrate. The lower inset is M-H loop after removal Zn_{0.96}Mn_{0.04}O from PMN-PT substrate [47]. 46
- Figure 2. 20 (a) Magneto-optical Kerr ellipticity (η_K) with applied voltages of 200 and -200V, as a function of magnetic field. The upper inset is the schematic diagram of magnetization direction of point A and B. The lower inset is the voltage manipulation of Kerr ellipticity, $d\eta_K dV$. (b) Schematics illustration of electric-field effect on electron filling of the 3d orbitals in ultrathin Fe layer [48]. 47
- Figure 2. 21 TEM images of Au (4 nm)/Fe (1 nm)/BTO (150nm)/LSMO (50 nm) on STO (001). (a) Elemental mapping analysis. (b) Elemental profiles acquired from electron energy loss spectroscopy (ELLS) line scans, showing a significant amount of O outside the BTO layer. X-ray absorption spectroscopy (XAS) Fe-L_{2,3} spectra obtained from Au/Co/Fe(2 monolayers)/BTO/LSMO on (001) STO at 300 K, after polarization of BTO with (c) $V^+ = 5V$ (P_{up}) and (d) $V^- = -5V$ (P_{down}). (e) XMCD signal from Fe-L₃ energy region for different polarization directions; the yellow region indicates the oxidized Fe layer adjacent with BTO layer [49]. 48
- Figure 3. 1 Surface morphology of STO (001) substrate in different states: (a) as-received, and (b) after a series of substrate treatment processes. (c) shows the line profile along the line in Figure 3. 1 (b) 53
- Figure 3. 2 Schematics diagram of PLD system used in this project. 55
- Figure 3. 3 Three different thin film growth mode: (a) island growth mode, (b) layer-by-layer growth mode, and (c) Stranski-Krastinov growth mode. 56



- Figure 3. 4 Schematic illustration (left) and cross-sectional view (right) of the device geometry for magnetism modulation in LSMO induced by charge accumulation. 59
- Figure 3. 5 The schematic diagram and side view of electric-field manipulation in magnetism of $Zn_{1-x}Mn_xO$ ($x = 0.08$). 61
- Figure 3. 6 (a) XRD θ -2 θ scan of 24 nm-thick LSMO film on (001) STO substrate. * represents the satellite peaks., (b) XRD ω -scan of (002) LSMO film, showing a FWHM around 0.1° 62
- Figure 3. 7 XRR measurement of a 15-nm $La_{0.8}Sr_{0.2}MnO_3$ film deposited on (001) STO substrate by PLD. 63
- Figure 3. 8 Schematics diagram of atomic force microscopy. Adapted from [8] 63
- Figure 3. 9 Schematic diagram of X-ray photoelectron effect. 64
- Figure 3. 10 Schematic illustration of transmission electron microscopy. Adapted from [9]. 65
- Figure 3. 11 Schematic diagram of VSM system. Adapted from [7]. 66
- Figure 3. 12 Schematic diagram of a 6-contact Hall-bar pattern. 67
- Figure 3. 13 AHE of as-deposited Co-doped ZnO (red circles), overlapped with the corresponding M-H loop (dashed line). The inset shows the same measurements for a vacuum-annealed sample. [10]. 68
- Figure 4. 1 Left: Schematic diagram of device structure used for electric-field manipulation of magnetism in the $P(VDF-TrFE)/LSMO$ with accumulated hole carriers in the LSMO channel due to ferroelectric polarization. Right: Planar view of Hall-bar pattern used in this study. 73
- Figure 4. 2 AFM image of 7.5 nm-thick LSMO film grown on STO (001) substrate. 74
- Figure 4. 3 XRD patterns. (a) θ -2 θ scans of bare STO substrate (black color), 24 nm-thick LSMO film (blue color) and $P(VDF-TrFE)/LSMO$ heterostructure (red color). (b) rocking curve acquired from LSMO (002) diffraction peak. (c) θ -2 θ scan of $P(VDF-TrFE)/LSMO$ heterostructure between 2θ values of 16° to 22° , indicating the β phase $P(VDF-TrFE)$ (200)/(110) peak 75
- Figure 4. 4 (a) Hysteresis loop of the OP PFM phase and magnitude signals obtained from $P(VDF-TrFE)/LSMO$ heterostructure, (b) PFM phase images of inner and intermediate square domains, pre-polarized with -10 V and +10 V respectively. (d) AFM image of $P(VDF-TrFE)$ acquiring during the poling process. 77
- Figure 4. 5 R-T measurement for 7.5 nm-thick LSMO film upon upward and downward polarization from $P(VDF-TrFE)$, where P_+ and P_- in the legend represent upward and downward polarization direction in $P(VDF-TrFE)$. The inset shows the magnified view of the measurement around the peak of the curves. 78
- Figure 5. 1 (a) XRR measurement of LSMO film grown on TiO_2 -terminated STO (001) substrate. Inset shows AFM scan of the LSMO film (scan area = $1 \mu m^2$). (b) Polarization hysteresis loop of $P(VDF-TrFE)$ prepared on glass substrate, with the inset showing the XRD θ -2 θ scan profile of $P(VDF-TrFE)$ on LSMO film surface. 86
- Figure 5. 2 (a) Schematics diagram of the FET device with LSMO channel and $P(VDF-TrFE)$ gate. The plots in (b) and (c) show the resistance change $\Delta R_{xx}/R_0$ (left axis) and ΔR_{xx} (right axis) of LSMO channel as functions of different pulse parameters: (b) number of pulse cycles (for constant pulse amplitude of 10 V and width of 300 ms); (c) pulse width (for constant pulse amplitude of 10 V and pulse cycles of 60). 87
- Figure 5. 3 $\Delta R_{xx}/R_0$ (left axis) and R_{xx} (right axis) in response to successive +10 V (first 30k) and -10 V (up to 10^6) pulses with constant pulse width (300 ms). Inset of figure highlights the switching-up process in LSMO $\Delta R_{xx}/R_0$ (left axis) and R_{xx} during the +10 V pulse cycles at the beginning of the measurement in the main figure. 88
- Figure 5. 4 Evolution of V_o in LSMO channel with successive positive and negative V_g pulses, according to the proposed electrochemical switching mechanism. 90
- Figure 5. 5 Variation of ΔR_{xx} of LSMO channel as a function of V_g pulse number in different environment. (a) $+V_g$ cycles in vacuum (squares) and oxygen (triangles) environment. (b) $-V_g$ cycles in vacuum (squares) and oxygen (triangles) environment. 90



- Figure 5. 6 (a) Mn 2p XPS spectra of LSMO film at pristine state and after + V_g pulsing for 36,000 cycles. (b) and (c) shows the multiple peak fitting of the XPS spectra for pristine (b) and gated (c) samples. 91
- Figure 5. 7 (a) Time profile of LSMO channel resistance as a function of + V_g from 0 to 36k cycles. (b) R-T measurement for sample undergone various positive V_g cycles. (c) Change in T_c as a function of positive V_g cycles (main figure) and R_{xx} at 300 K (inset). 93
- Figure 5. 8 Variation of LSMO channel magnetotransport properties at 20 K with applied + V_g , (a) MR behavior for LSMO channel undergone + V_g pulse cycles; the inset indicates the magnified view of MR loop, after the application of 36k + V_g pulses. (b) MR ratio (20 K) and R_{xx} (300 K) as a function of + V_g pulse cycle at 300K. 95
- Figure 5. 9 Reversibility of LSMO channel resistance at 300 K (a), T_c of LSMO (b), and MR of LSMO channel at 20 K (c), through the application of positive and negative V_g pulses. Note that the number of pulses in each 'cycle' (x-axis of the graphs) are different (c.f. Fig. 5. 2). 96
- Figure 6. 1 XRD θ - 2θ scan for the $Zn_{0.92}Mn_{0.08}O/Al_2O_3$. Inset: rocking curve of (0002) $Zn_{0.92}Mn_{0.08}O$ diffraction peak. 104
- Figure 6. 2 (a) High-resolution cross-sectional TEM image of the $Zn_{0.92}Mn_{0.08}O/Al_2O_3$, the d-spacing of $Zn_{0.92}Mn_{0.08}O$ and Al_2O_3 are 0.26 and 0.21 nm respectively. (b) The elemental distribution Zn, Mn and O for the $Zn_{0.92}Mn_{0.08}O$ as examined by elemental mapping in TEM. (c) SAED pattern on the interfaces of ZnO/Al_2O_3 , which is taken at (0001) Al_2O_3 105
- Figure 6. 3 Schematics diagram of $Zn_{0.92}Mn_{0.08}O$ device with Hall-bar pattern and IL as electrolyte. 106
- Figure 6. 4 (a) XPS core-level spectra of $Zn_{0.92}Mn_{0.08}O$, showing binding energies of (a) Mn 2p and (b) Zn 2p. Legends indicate the application of different V_g of -2, 0 and 2 V in 230 K for 1 hour before measurements. 107
- Figure 6. 5 Upper panel: $I_{DS}(V_g)$ measurement of $Zn_{0.92}Mn_{0.08}O$ using a scan rate of 100 mV/s, the curve corresponds to 50 consecutive I(V) measurement. Lower panel is the corresponding leakage current across the $Zn_{0.92}Mn_{0.08}O$ EDLT. 108
- Figure 6. 6 AFM surface topography of $Zn_{0.92}Mn_{0.08}O$ EDLT with different V_g . The root mean square roughness for the samples are: (a) 0.64 nm, (b) 0.65 nm and (c) 0.66 nm. 109
- Figure 6. 7 R_{xx} -time curve with different V_g (2, 0, -2V). 110
- Figure 6. 8 R_{xx} -T of R_{xx} in $Zn_{0.92}Mn_{0.08}O$ EDLT for $V_g = -2$ (blue triangles), 0 (black squares) and 2 V (red circles). 111
- Figure 6. 9 Temperature dependences of various Hall measurement parameters in $Zn_{0.92}Mn_{0.08}O$ EDLT for $V_g = -2$ and 2 V: ρ (a), n (b) and μ_e (c). 112
- Figure 6. 10 MR of $Zn_{0.92}Mn_{0.08}O$ EDLT for different V_g at 10 K (a), 20 K (b), 40 K (c) and 100 K (d). 113
- Figure 6. 11 (a) Hall resistivity of 10-nm thick $Zn_{0.92}Mn_{0.08}O$ EDLTs measured at 50 K as a function of magnetic field. (b) AHE after subtracting the linear contribution from ordinary Hall resistivity. Dashed lines are guides to the eye. (c) Hysteresis loop of a 250 nm-thick $Zn_{0.92}Mn_{0.08}O$ film at 50 K. 115



List of tables

Table 3.1 Experimental conditions for PLD of LSMO and $Zn_{0.92}Mn_{0.08}O$ thin films. 57



Chapter 1 Introduction

1.1 Background and objectives

The strong correlations between spin, charge, orbital and lattice degrees of freedom in transition metal oxides (TMO) provide a variety of interesting features including superconductivity, magnetism, spin-and charge ordering [1-3], among many others. Such correlations in TMO provide fundamental prerequisites to develop novel and tunable functionalities including magnetism, superconductivity and metal-to-insulator transition in the electronic devices through the application of electric-field, which cannot be achieved in conventional semiconductors [4-7]. Take $Zn_{1-x}Mn_xO$ as an example, isovalent ions are introduced into $Zn_{1-x}Mn_xO$ by substitution of divalent ion (Zn^{2+}) into divalent ion (Mn^{2+}) [8]. These chemical substitutions are not applicable for tuning the ferromagnetic properties in the electronic devices, while such tuning in the electronic devices through the application of electric field is highly desired [1, 8-10].

Manipulation of electronic and magnetic properties in TMO has attracted lots of attention [2, 3], such as colossal magnetoresistance (CMR) [11-14], magnetocaloric effects[15] and metal-to-insulator transition [14]. The electrostatic doping through field-effect transistor geometry is conventionally used to achieve the modulation of carriers in the TMO [5, 7, 9, 16-19]. As the electric field is applied through the dielectric layer, the charge carriers in the TMO channel are accumulated or repelled to form the conducting layer [5, 10]. Besides gating with dielectric materials, artificial multiferroic heterostructures provide an alternative solution for modulating the carrier density in TMO, by inducing changes in the ferromagnet layer through polarization in the ferroelectric components [18, 20-22]. This magneto-electric effect has been observed in previous work of $La_{0.85}Ba_{0.15}MnO_3/Pb(Zr_{0.2}Ti_{0.8})O_3$ heterostructures [21, 23], which demonstrated that the magnetic and electric-transport properties in $La_{0.85}Ba_{0.15}MnO_3$ can be simultaneously changed by switching the ferroelectric layer. Lu *et al.* further suggested that the modulation of metal-to-insulator transition in $La_{0.67}Sr_{0.33}MnO_3$ (LSMO) can arise from the electrostatic doping due to ferroelectric reversal in $BaTiO_3$ (BTO) [22]. These reports also concluded that the screening depth provided from the ferroelectric layer can be extended up to 3 nm, which is far beyond the expected values in metallic LSMO. Besides TMO, the interfacial magnetoelectric coupling in Fe/BTO heterostructures have been studied by Radaelli *et al.* [24]. Their results indicated that the magnetization can be



reversibly switched between on and off states by electric field. The manipulation of magnetism in these heterostructure is mainly due to the ionic displacement in BTO, leading to the reversible oxidation of the Fe layer.

In order to achieve a high tunability in the carrier density of the channel layer, dielectric selection and the thickness of the channel layer should be considered. First, a large change of carrier density in the channel layer requires a high capacitance of the dielectric, implying that the dielectric should possess high breakdown voltage and of minimal thickness. Secondly, the thickness of the ferromagnet should be comparable with the screening depth (typically around 1 nm) to achieve a high tunability of carrier concentration in TMO or ferromagnet. Typically, the change in carrier density can be up to 10^{14} cm^{-2} .

Beside using dielectric and ferroelectric as gate materials [25], many reports attempted to enhance the tunability in magnetism by using the electric-double layer (EDL) in ionic liquid (IL) [26-29], since the change in carrier densities can reach up to 10^{15} cm^{-2} [29, 30]. This electrostatic doping effect through IL was observed by Dhoot *et al.* in 5 nm-thick $\text{La}_{0.8}\text{Ca}_{0.2}\text{MnO}_3$ (LCMO) transistor devices [30]. With the application of a positive gate voltage through the IL, the LCMO film could be changed from a ferromagnetic metal to an insulating ground state. Their results also indicated that the electrostatic doping can extend up to 5 nm in LCMO, achieving a doping concentration of $2 \times 10^{15} \text{ cm}^{-2}$.

Beyond electrostatic doping, many studies also attempted to operate the IL through electrochemical reaction in the channel layer [25, 31, 32]. This electrochemical reaction can offer an exceptional tunability of carrier concentration. Cui *et al.* demonstrated electrochemically-induced LSMO layer modulation through the gating process in IL [25]. Their results indicated that the metal-to-insulator transition temperature of LSMO could be changed by up to 60 K. The formation and annihilation of hard magnetic insulating phase were observed in transmission electron microscopy (TEM) measurements upon the application of the gate voltage, accompanied by the changes in Mn valence and magnetotransport behaviour in the LSMO devices.

For achieving a large tunability of carrier density in the ferromagnet [33], several attempts were made to manipulate the transport and magnetic properties of ferromagnets through a redox reaction between the ferromagnetic channel and the gating material [9, 34, 35]. For example, Gilbert *et al.* studied the $\text{AlO}_x/\text{GdO}_x/\text{Co}$ heterostructures [35], and their



results demonstrated that the reversible control of magnetization in the heterostructure is mainly due to the change in the Co valence states, originating from the oxygen transferring from GdO_x at the operating temperature of 230°C .

1.2 Signification of this work

Much efforts have been made to improve the performance of memory devices, such as ones based on the current-induced magnetization reversal in spin-transfer torque (STT) [5, 7, 10, 36]. Rather than using the electric current to manipulate the magnetism, electric field-based control of magnetism is now drawing lots of attentions, since the energy dissipation of electric field based devices is much smaller when compared with current-based ones. Moreover, the electric-field devices are compared to the existing field-effect devices, and with further advantages of non-volatile behavior [5].

Due to the technology importance of such electric field-based devices [5, 7, 9, 10, 18, 19, 37, 38], I investigated the electric-field manipulation of transport and magnetic properties of oxide-based devices. Electric-field-induced manipulation of magnetism through different methods, such as ferroelectric control by poly[(vinylidene fluoride-co-trifluoroethylene) [P(VDF-TrFE)], oxygen vacancy modulation through low-voltage-pulse cycles and electrostatic control through IL, were investigated in this thesis.

1.3 Outline of thesis

This thesis attempts to investigate the electric-field manipulation of transport and magnetic properties in ultrathin LSMO and $\text{Zn}_{0.92}\text{Mn}_{0.08}\text{O}$ films with the field-effect transistor (FET) device geometry. Different gating approaches are studied.

The thesis is arranged in the following way:

- The fundamental concepts of TMO such as LSMO and $\text{Zn}_{0.92}\text{Mn}_{0.08}\text{O}$ are provided in Chapter 2. Different methods for achieving the electric-field manipulation of magnetism in ferromagnets are described.
- Chapter 3 describes an overview of experimental methods, including the substrate treatment processes, thin film fabrication techniques used for the preparation of oxide films, and the structural, electrical and magnetic characterization methods used in this project.



- Chapter 4 details the study of electric-field-effect manipulation of transport and magnetic properties in 7.5 nm-thick LSMO thin film through ferroelectric copolymer of P(VDF-TrFE). Experimental details of these LSMO FET are discussed. Ferroelectric-induced changes in transport and magnetism in LSMO devices are studied.
- In Chapter 5, a different LSMO modulation approach using the same device structure in Chapter 4 is explained. Upon the application of low-voltage pulses through the P(VDF-TrFE) gate, resistance-temperature (R - T) measurements of the LSMO channel reveal a change of the Curie temperature (T_C) by more than 14 K. Through the measurement results of X-ray photoelectron spectroscopy (XPS) and LSMO resistance switching behavior in different gas environment, I will demonstrate that the enhanced tunability of transport and magnetic properties in LSMO channel were mainly due to oxygen vacancy (O_v) modulation with the assistance of P(VDF-TrFE) as a dielectric.
- Chapter 6 focuses on the electric-field induced changes in the transport and magnetic properties of DMS, $Zn_{0.92}Mn_{0.08}O$, using an electric double-layer gating through an IL. The results indicate that magnetoresistance at low temperature, and the perpendicular component of magnetization as measured through anomalous Hall effect (AHE), are varied by the application of external electric field.
- The important findings of this thesis are summarized in Chapter 7, in which potential future work on magnetism modulation in oxide films are also presented.



References for Chapter 1

- [1] J.H. Ngai, F.J. Walker, C.H. Ahn, Correlated Oxide Physics and Electronics, Annual Review of Materials Research, 44 (2014) 1-17.
- [2] M. Lorenz, M.S.R. Rao, T. Venkatesan, E. Fortunato, P. Barquinha, R. Branquinho, D. Salgueiro, R. Martins, E. Carlos, A. Liu, F.K. Shan, M. Grundmann, H. Boschker, J. Mukherjee, M. Priyadarshini, N. DasGupta, D.J. Rogers, F.H. Teherani, E.V. Sandana, P. Bove, K. Rietwyk, A. Zaban, A. Veziridis, A. Weidenkaff, M. Muralidhar, M. Murakami, S. Abel, J. Fompeyrine, J. Zuniga-Perez, R. Ramesh, N.A. Spaldin, S. Ostanin, V. Borisov, I. Mertig, V. Lazenka, G. Srinivasan, W. Prellier, M. Uchida, M. Kawasaki, R. Pentcheva, P. Gegenwart, F.M. Granozio, J. Fontcuberta, N. Pryds, The 2016 oxide electronic materials and oxide interfaces roadmap, Journal of Physics D: Applied Physics, 49 (2016) 433001.
- [3] E. Dagotto, Complexity in Strongly Correlated Electronic Systems, Science, 309 (2005) 257-262.
- [4] D.M. Newns, J.A. Misewich, C.C. Tsuei, A. Gupta, B.A. Scott, A. Schrott, Mott transition field effect transistor, Applied Physics Letters, 73 (1998) 780-782.
- [5] F. Matsukura, Y. Tokura, H. Ohno, Control of magnetism by electric fields, Nat. Nanotech, 10 (2015) 209-220.
- [6] F. Hellman, A. Hoffmann, Y. Tserkovnyak, G.S.D. Beach, E.E. Fullerton, C. Leighton, A.H. MacDonald, D.C. Ralph, D.A. Arena, H.A. Dürr, P. Fischer, J. Grollier, J.P. Heremans, T. Jungwirth, A.V. Kimel, B. Koopmans, I.N. Krivorotov, S.J. May, A.K. Petford-Long, J.M. Rondinelli, N. Samarth, I.K. Schuller, A.N. Slavin, M.D. Stiles, O. Tchernyshyov, A. Thiaville, B.L. Zink, Interface-induced phenomena in magnetism, Reviews of Modern Physics, 89 (2017) 025006.
- [7] C. Song, B. Cui, F. Li, X. Zhou, F. Pan, Recent progress in voltage control of magnetism: Materials, mechanisms, and performance, Progress in Materials Science, 87 (2017) 33-82.
- [8] X.L. Wang, K.H. Lai, A. Ruotolo, A comparative study on the ferromagnetic properties of undoped and Mn-doped ZnO, Journal of Alloys and Compounds, 542 (2012) 147-150.
- [9] D. Chiba, T. Ono, Control of magnetism in Co by an electric field, Journal of Physics D: Applied Physics, 46 (2013) 213001.
- [10] S. Cheng, C. Bin, P. Jingjing, M. Haijun, P. Feng, Electrical control of magnetism in oxides, Chinese Physics B, 25 (2016) 067502.
- [11] A. Urushibara, Y. Moritomo, T. Arima, A. Asamitsu, G. Kido, Y. Tokura, Insulator-metal transition and giant magnetoresistance in $\text{La}_{1-x}\text{Sr}_x\text{MnO}_3$, Physical Review B, 51 (1995) 14103-14109.
- [12] C. Zener, Interaction between the d -Shells in the Transition Metals. II. Ferromagnetic Compounds of Manganese with Perovskite Structure, Physical Review, 82 (1951) 403-405.
- [13] J. Hemberger, A. Krimmel, T. Kurz, H.A. Krug von Nidda, V.Y. Ivanov, A.A. Mukhin, A.M. Balbashov, A. Loidl, Structural, magnetic, and electrical properties of single-crystalline $\text{La}_{1-x}\text{Sr}_x\text{MnO}_3$ ($0.4 < x < 0.85$), Physical Review B, 66 (2002) 094410.
- [14] A.M. Haghiri-Gosnet, J.P. Renard, CMR manganites: physics, thin films and devices, Journal of Physics D: Applied Physics, 36 (2003) R127.
- [15] M.-H. Phan, S.-C. Yu, Review of the magnetocaloric effect in manganite materials, Journal of Magnetism and Magnetic Materials, 308 (2007) 325-340.
- [16] C.H. Ahn, J.M. Triscone, J. Mannhart, Electric field effect in correlated oxide systems, Nature, 424 (2003) 1015-1018.



- [17] C.H. Ahn, A. Bhattacharya, M. Di Ventra, J.N. Eckstein, C.D. Frisbie, M.E. Gershenson, A.M. Goldman, I.H. Inoue, J. Mannhart, A.J. Millis, A.F. Morpurgo, D. Natelson, J.-M. Triscone, Electrostatic modification of novel materials, *Reviews of Modern Physics*, 78 (2006) 1185-1212.
- [18] Q. Yang, Z. Zhou, N.X. Sun, M. Liu, Perspectives of voltage control for magnetic exchange bias in multiferroic heterostructures, *Physics Letters A*, 381 (2017) 1213-1222.
- [19] M. Liu, N.X. Sun, Voltage control of magnetism in multiferroic heterostructures, *Philos. Trans. Royal Soc. A*, 372 (2014).
- [20] X. Hong, A. Posadas, A. Lin, C.H. Ahn, Ferroelectric-field-induced tuning of magnetism in the colossal magnetoresistive oxide $\text{La}_{1-x}\text{Sr}_x\text{MnO}_3$, *Physical Review B*, 68 (2003) 134415.
- [21] T. Kanki, H. Tanaka, T. Kawai, Electric control of room temperature ferromagnetism in a $\text{Pb}(\text{Zr}_{0.2}\text{Ti}_{0.8})\text{O}_3/\text{La}_{0.85}\text{Ba}_{0.15}\text{MnO}_3$ field-effect transistor, *Applied Physics Letters*, 89 (2006) 242506.
- [22] H. Lu, T.A. George, Y. Wang, I. Ketsman, J.D. Burton, C.-W. Bark, S. Ryu, D.J. Kim, J. Wang, C. Binek, P.A. Dowben, A. Sokolov, C.-B. Eom, E.Y. Tsymbal, A. Gruverman, Electric modulation of magnetization at the $\text{BaTiO}_3/\text{La}_{0.67}\text{Sr}_{0.33}\text{MnO}_3$ interfaces, *Applied Physics Letters*, 100 (2012) 232904.
- [23] T. Kanki, Y.-G. Park, H. Tanaka, T. Kawai, Electrical-field control of metal-insulator transition at room temperature in $\text{Pb}(\text{Zr}_{0.2}\text{Ti}_{0.8})\text{O}_3/\text{La}_{1-x}\text{Ba}_x\text{MnO}_3$ field-effect transistor, *Applied Physics Letters*, 83 (2003) 4860-4862.
- [24] G. Radaelli, D. Petti, E. Plekhanov, I. Fina, P. Torelli, B.R. Salles, M. Cantoni, C. Rinaldi, D. Gutiérrez, G. Panaccione, M. Varela, S. Picozzi, J. Fontcuberta, R. Bertacco, Electric control of magnetism at the Fe/BaTiO_3 interface, *Nature communications*, 5 (2014) 3404-3404.
- [25] B. Cui, C. Song, G. Wang, Y. Yan, J. Peng, J. Miao, H. Mao, F. Li, C. Chen, F. Zeng, F. Pan, Reversible Ferromagnetic Phase Transition in Electrode-Gated Manganites, *Advanced Functional Materials*, 24 (2014) 7233-7240.
- [26] T. Fujimoto, K. Awaga, Electric-double-layer field-effect transistors with ionic liquids, *Physical Chemistry Chemical Physics*, 15 (2013) 8983-9006.
- [27] M. Galiński, A. Lewandowski, I. Stępnik, Ionic liquids as electrolytes, *Electrochimica Acta*, 51 (2006) 5567-5580.
- [28] H. Yuan, H. Shimotani, A. Tsukazaki, A. Ohtomo, M. Kawasaki, Y. Iwasa, High-Density Carrier Accumulation in ZnO Field-Effect Transistors Gated by Electric Double Layers of Ionic Liquids, *Advanced Functional Materials*, 19 (2009) 1046-1053.
- [29] S.Z. Bisri, S. Shimizu, M. Nakano, Y. Iwasa, Endeavor of Iontronics: From Fundamentals to Applications of Ion-Controlled Electronics, *Advanced Materials*, 29 (2017) n/a-n/a.
- [30] A.S. Dhoot, C. Israel, X. Moya, N.D. Mathur, R.H. Friend, Large Electric Field Effect in Electrolyte-Gated Manganites, *Physical Review Letters*, 102 (2009) 136402.
- [31] H.T. Yi, B. Gao, W. Xie, S.-W. Cheong, V. Podzorov, Tuning the metal-insulator crossover and magnetism in SrRuO_3 by ionic gating, *Scientific Reports*, 4 (2014) 6604.
- [32] J. Walter, H. Wang, B. Luo, C.D. Frisbie, C. Leighton, Electrostatic versus Electrochemical Doping and Control of Ferromagnetism in Ion-Gel-Gated Ultrathin $\text{La}_{0.5}\text{Sr}_{0.5}\text{CoO}_{3-\delta}$, *ACS Nano*, 10 (2016) 7799-7810.
- [33] C. Ge, K.-J. Jin, L. Gu, L.-C. Peng, Y.-S. Hu, H.-Z. Guo, H.-F. Shi, J.-K. Li, J.-O. Wang, X.-X. Guo, C. Wang, M. He, H.-B. Lu, G.-Z. Yang, Metal-Insulator Transition Induced by Oxygen Vacancies from Electrochemical Reaction in Ionic Liquid-Gated Manganite Films, *Advanced Materials Interfaces*, 2 (2015) 1500407.



- [34] M. Huang, A.J. Tan, M. Mann, U. Bauer, R. Ouedraogo, G.S.D. Beach, Three-terminal resistive switch based on metal/metal oxide redox reactions, *Scientific Reports*, 7 (2017) 7452.
- [35] D.A. Gilbert, A.J. Grutter, E. Arenholz, K. Liu, B.J. Kirby, J.A. Borchers, B.B. Maranville, Structural and magnetic depth profiles of magneto-ionic heterostructures beyond the interface limit, 7 (2016) 12264.
- [36] S. Ikeda, K. Miura, H. Yamamoto, K. Mizunuma, H.D. Gan, M. Endo, S. Kanai, J. Hayakawa, F. Matsukura, H. Ohno, A perpendicular-anisotropy CoFeB–MgO magnetic tunnel junction, *Nature Materials*, 9 (2010) 721.
- [37] D. Chiba, Electric field effect on magnetism in metallic ultra-thin films, *Front. Phys.*, 3 (2015).
- [38] S. Fusil, V. Garcia, A. Barthélémy, M. Bibes, Magnetoelectric Devices for Spintronics, *Annual Review of Materials Research*, 44 (2014) 91-116.



Chapter 2 Literature review

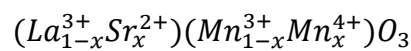
This Chapter gives a brief introduction on the fundamental concepts of magnetic oxides such as $\text{La}_x\text{Sr}_{1-x}\text{MnO}_3$ and ZnO . This is followed by a literature review about different methods for controlling magnetism in ferromagnets, such as electrostatic doping, electrochemical reactions, exchange coupling, strain effect and orbital reconstructions.

2.1 Manganites

Doped perovskite manganites such as the $\text{La}_x\text{Sr}_{1-x}\text{MnO}_3$ system attract lots of attention for the development of future spintronic applications [1], owing to their distinctive properties of nearly 100% spin polarization, high T_C , metallic conductivity and colossal magnetoresistance. These unique properties are mainly due to the strong coupling effect between spin, charge, lattice and orbital degrees of freedom [1]. In this section, the crystal structure, electronic and magnetic properties of manganites are presented.

2.1.1 Crystallographic structure of manganites

Mixed-valence manganites have the general chemical composition of $\text{A}_x\text{B}_{1-x}\text{MnO}_3$, where A is a trivalent rare-earth cation (La, Pr, Nd, Sm, Bi, Y, Ho, Er, Tb and Gd) and B is divalent alkali-earth cation (such as Sr, Ca, Pb and Ba). As divalent alkali-earth cations (Sr^{2+} in case of LSMO) substitute the trivalent rare-earth cations (La^{3+}) in the mixed valence manganite, the Mn ions can take two possible valence states of Mn^{3+} and Mn^{4+} for maintaining the charge stoichiometry, and can be expressed as below:



The crystal structure of $\text{La}_x\text{Sr}_{1-x}\text{MnO}_3$ belongs to perovskites with the formula ABO_3 , which is close to the ideal cubic structure (Figure 2. 1). The A site is occupied by the trivalent rare-earth cation (La^{3+}) or divalent alkali-earth cation (Sr^{2+}), and B site is occupied by the mixed valence manganese (Mn^{3+} and Mn^{4+}), which is located at the center and surrounded by the oxygen octahedron.

The crystal structure of the mixed-valence manganites is governed by the tolerance factor (t_f),

$$t_f = \frac{r_{A,B} + r_O}{\sqrt{2}(r_{Mn} + r_O)}$$



where $r_{A,B}$, r_{Mn} and r_O are the ionic radii of A, B, Mn and O ions respectively. The perovskite structure is stable with t_f between 0.89 and 1.02. For $t_f = 1$, the perfect cubic structure is preferred. The crystal structure of manganites generally belongs to orthorhombic perovskites with t_f appreciably differs from 1.

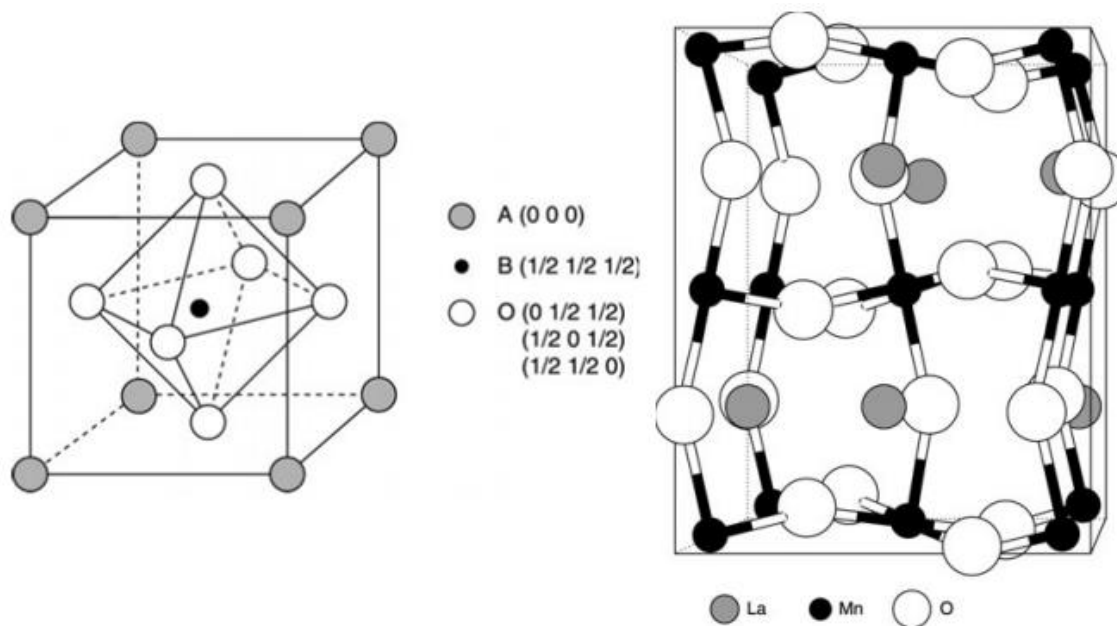


Figure 2. 1 Left: crystallographic structure of LaMnO_3 perovskite. Right: schematics illustration of cubic perovskite structure [1].

2.1.2 Electronic structure and Jahn-Teller distortion

The $3d$ electrons in Mn^{3+} ions experience an electric field from the surrounding oxygen octahedron, leading to the splitting of five degenerate orbital states for the $3d$ electrons into three t_{2g} orbitals (with lower energy) and two e_g orbitals (with higher energy). This effect is the so-called “crystal-field splitting”. This crystal-field splitting is typically ~ 2 eV for manganites. According to the Hund’s rule, the electron spins should be occupied and aligned into a half-filled parallel status in order to maximize the total spin, which is the result of the Coulomb interaction within a single atom. This so-called Hund’s rule energy is typically ~ 4 eV in manganites and is much larger than the crystal field splitting [2]. Figure 2. 2 shows the case for manganites that Hund’s rule coupling is larger than the crystal-field splitting. Under this case, four electrons with parallel spins are distributed such that one occupies the e_g level and the remaining three take the t_{2g} level. Such a single electron in the e_g level results in the case that Mn^{3+} ion is active in Jahn-Teller



effect. Based on Jahn-Teller theory, Mn^{3+}O_6 octahedra in the manganites would elongate along z-direction, and causes the energies of d_{z^2} , d_{xz} and d_{yz} orbitals to decrease. In the perovskite manganites, the splitting energy due to the Jahn-Teller distortion is typically 0.6 eV [2]. Owing to absence of an unpaired electron in the e_g orbitals, Mn^{4+} ion is inactive in Jahn-Teller effect.

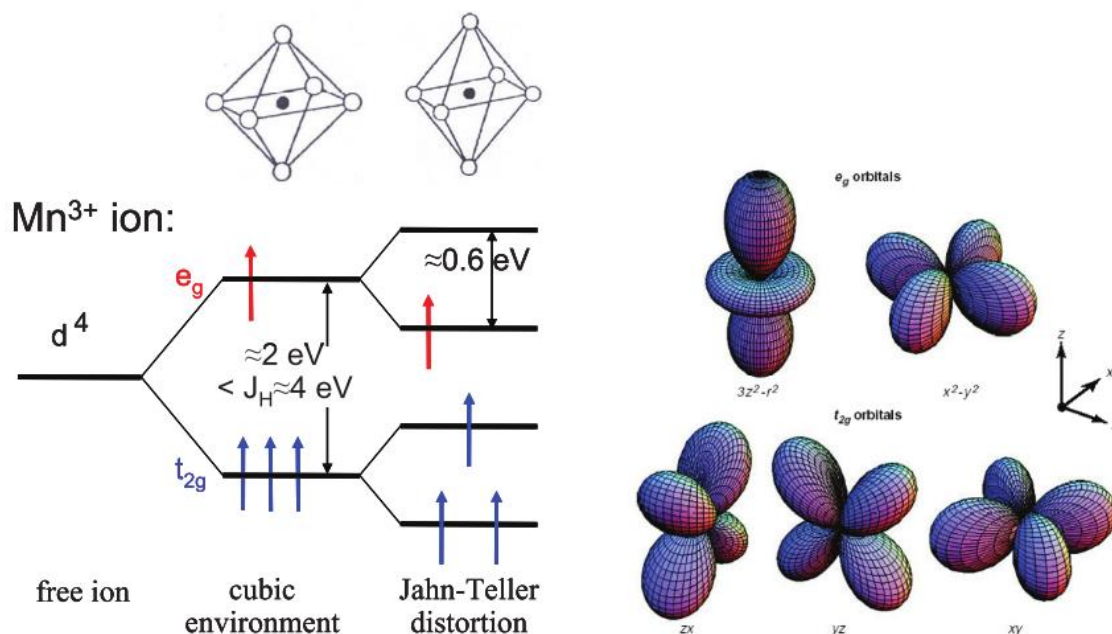


Figure 2. 2 Schematics illustration of energy levels of Mn^{3+} free ions and Mn^{3+} in oxygen octahedron. Taking manganite as a case, the Hund's rule is stronger than crystal field splitting. The Jahn-Teller effect lifts the degeneracy of e_g level and results in elongation of MnO_6 axial direction. The right side shows the five 3d orbitals three t_{2g} orbitals and two e_g orbitals [2].

2.1.3 Double-exchange coupling

LaMnO_3 (LMO) is the parent compound of $\text{La}_x\text{Sr}_{1-x}\text{MnO}_3$, with only Mn^{3+} ion being present. The 3d electrons (triple t_{2g} and one e_g) hybridize with O 2p states and results an insulating and antiferromagnetic states ($\text{Mn}^{3+}\text{-O-Mn}^{3+}$). When part of the La^{3+} ions are replaced by Sr^{2+} ions in the LMO lattice, a corresponding number of Mn ions have to be changed from 3+ to 4+ in order to maintain the charge stoichiometry. As suggested by Zener [3], the direct coupling between Mn^{3+} and Mn^{4+} is not possible, since the distance between Mn^{3+} and Mn^{4+} orbitals is too far and without any appreciable overlapping. Zener *et al.* further proposed the double-exchange coupling between Mn^{4+} and Mn^{3+} mediating through the oxygen p-orbital, that could induce ferromagnetic signal and electronic conduction in the mixed-valence manganites [3], as shown in Figure 2. 3. Based on the



theory of double-exchange (DE), the magnetic properties of manganites are determined by a transfer of e_g electrons in Mn^{3+} ions to the oxygen $2p$ orbital, and the simultaneous transfer of another electron from O $2p$ orbital to the empty e_g state in the Mn^{4+} site. Upon the completion of the transfer processes, Mn^{3+} changes to Mn^{4+} and vice-versa. Due to Hund's rule, the electron hopping mechanism between Mn^{3+} to Mn^{4+} can happen when the spin alignment of t_{2g} electrons are in parallel states. As a result, double-exchange mechanism between Mn^{3+} and Mn^{4+} leads ferromagnetic alignment of spins and is associated with electron conductivity. The hopping probability between Mn^{3+} and Mn^{4+} ions depend on the relative orientation of neighboring spins, which is proportional to $\cos(\theta/2)$, where θ is the bond angle of Mn-O-Mn. In the case of $\text{La}_{0.66}\text{Sr}_{0.33}\text{MnO}_3$, it is ferromagnetic at low temperatures and possesses high conductivity due to the active hopping channel ($\theta = 0$). As the temperature goes up, manganites transits from the ferromagnetic state to a disordered state (with reduced conductivity) as the hopping channel becomes forbidden. Therefore, the transition temperature from metallic to insulator states matches with the T_C , and one can infer the magnetism of manganites through R-T measurements.

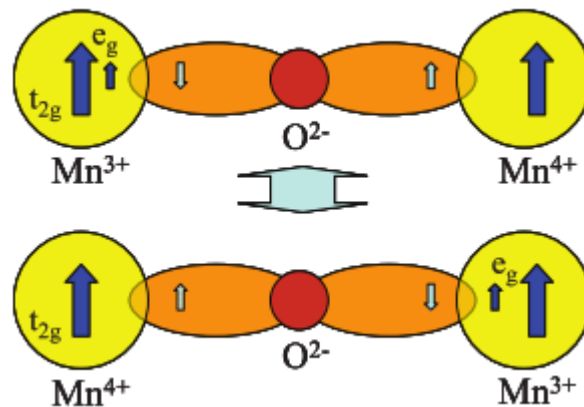


Figure 2.3 Schematic illustration of double exchange mechanism in Mn^{3+} -O- Mn^{4+} and Mn^{4+} -O- Mn^{3+} [4].

2.1.4 Super-exchange coupling

Super-exchange (SE) coupling is the electron interaction between the Mn ions and O $2p$ orbitals. Owing to weak overlapping between t_{2g} in Mn ions and $2p$ orbitals in O ions, the t_{2g} electrons are confined. t_{2g} electrons virtually hop between two Mn ions through O- $2p$ orbitals. For Mn^{3+} and Mn^{4+} , t_{2g} electrons are half-filled due to Hund's rules. According to Pauli exclusion principle, the transferred electrons between Mn^{4+} and Mn^{3+}



through O-2p orbitals should be in opposite spin directions. Therefore, the relative spins of Mn^{3+} and Mn^{4+} possess antiparallel state, leading to an antiferromagnetic coupling. However, SE coupling does not necessarily lead to antiferromagnetic behaviour but can lead to weak ferromagnetic. Based on the Goodenough-Kanamori rules [3, 5, 6], a certain dependence on the e_g orbital occupancy and bond angle in the Mn-O-Mn can predict whether ferromagnetic or antiferromagnetic interaction inside the manganite is dominant, as listed below:

1. The exchange between empty or filled e_g states is strong in antiferromagnetic interaction when the bond angle is 180° in the Mn-O-Mn.
2. The exchange between one empty and one filled orbital is weak in ferromagnetic interaction when the bond angle is 180° in the Mn-O-Mn.
3. The exchange coupling between both filled orbitals are weak in ferromagnetic interaction when the bond angle is 180° in the Mn-O-Mn.

2.1.5 $\text{La}_{1-x}\text{Sr}_x\text{MnO}_3$ phase diagram

Bulk $\text{La}_{1-x}\text{Sr}_x\text{MnO}_3$ exhibits different magnetic interactions such as SE and DE with varying Sr doping concentrations as shown in Figure 2. 4. For $0 < x < 0.1$, an A-type antiferromagnetic interaction due to SE interaction is dominant with $T_N \sim 130$ K. In this doping concentration, the manganite is highly insulating, since the major valence of Mn ions is $3+$. As x increases to 0.17, ferromagnetic interaction due to DE interaction gradually dominates and T_C can be observed, but the material is still insulating. With further increases in x to 0.5, ferromagnetic state with metallic behavior at low temperature dominates due to DE interaction. The peak of T_C is 360 K at $x \approx 0.33$ [7]. Above $x = 0.5$, the antiferromagnetic interaction starts to dominate due to SE interaction. Up to $x < 0.7$, the transport properties still belong to metallic. As $0.7 < x < 1$, magnetic interaction of manganites becomes C-type antiferromagnetic and the system is insulating [7].

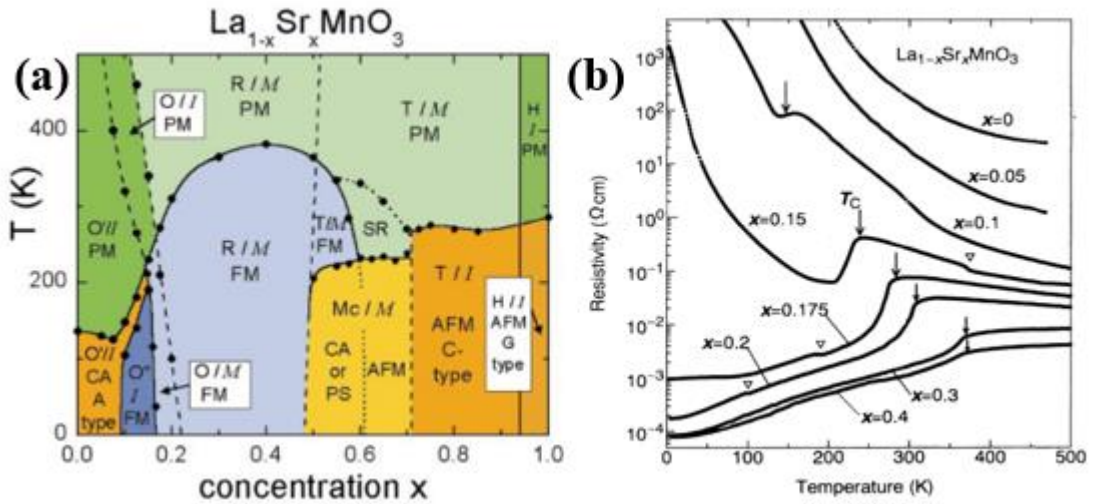


Figure 2. 4 (a) Phase diagram of $La_{1-x}Sr_xMnO_3$ bulk crystals with different Sr doping concentration x [8]. (b) Temperature dependence of resistivity for different Sr doping concentration (x) of $La_{1-x}Sr_xMnO_3$ bulk crystals. Arrows and open triangles indicated the T_C and structural changes from rhombohedral to orthorhombic [7].

2.2 Zinc oxide

Owing to the large direct bandgap (3.4 eV) and high exciton energy (60 meV), ZnO-based materials have attracted lots of attention due to the promising applications in spintronics and optoelectronic devices such as light-emitting diodes and transparent conducting electrodes for liquid crystal display [9]. The native doping of ZnO materials are O_V , while making p -type doping in ZnO is quite challenging [10].

2.2.1 Crystal structure

Figure 2. 5 shows that ZnO has three common allotropes, namely rocksalt, cubic zincblende and hexagonal wurtzite. ZnO with rocksalt structure is only stable at extremely high pressures (10 GPa) and cannot be epitaxially grown on lattice-matching substrates, unless a large proportion of MgO is doped into the ZnO lattice (40%). Zincblende ZnO is rare and can only be grown on cubic substrates such as cubic-phase ZnS. Under ambient pressure and temperature, ZnO crystalizes into the hexagonal wurtzite structure with a and c lattice constants of 0.33 and 0.52 nm, respectively. The Zn ions are bonded with the oxygen ion tetrahedron. This ZnO lattice exhibits a lack of inversion symmetry, which induces piezoelectric and pyroelectric properties [9].

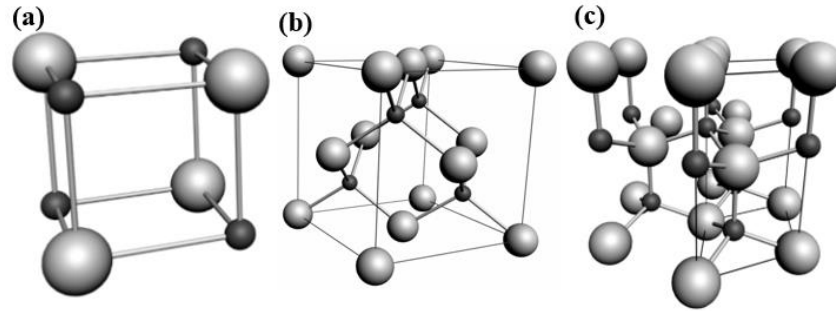


Figure 2. 5 Crystal structures of common ZnO allotropes: (a) rocksalt, (b) zincblende and (c) hexagonal wurtzite. Large and small circles indicate oxygen and zinc atoms, respectively [9].

2.2.2 Diluted magnetic semiconductor

In 1961, Matthias *et al.* first demonstrated simultaneous ferromagnetism and semiconducting behavior in europium oxide (EuO) [11]. This type of material is termed magnetic semiconductor, as all magnetic atoms are periodically distributed inside the semiconductor lattice. However, its low T_C (<80 K) means it is not suitable for integration into current semiconductor industries.

More efforts were made on the discovery of DMS, in which a small portion of cations are replaced by the transition metal ions [12-14], while the magnetic moment of these DMS are mainly due to the partially occupied $3d$ and $4f$ electrons of magnetic ions [15-18]. Dietl *et al.* predicted theoretically that p -type semiconductors such as Mn-doped GaN or ZnO exhibit T_C higher than room temperature and with bandgap larger than 3 eV [12], as shown in Figure 2. 6. Such DMS materials have great potential to fabricate practical spintronic devices such as spin-light emitting diode and spin-field effect transistor working at room temperature.

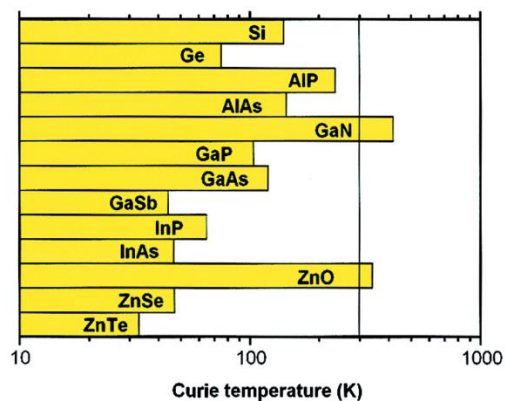


Figure 2. 6 Computed Curie temperatures for different p -type semiconductors [12].

2.2.3 Donor impurity-band exchange model

Coey *et al.* adapted the donor impurity-band model to explain the variation of magnetic moments across $3d$ -transition metal-doped ZnO films, and how structural defects such as O_v and zinc interstitial (Zn_i) induce ferromagnetism in n -type materials [13]. Considering Mn-doped ZnO as an example (Figure 2. 7), O_v in the ZnO lattice give rise to impurity states in the band diagram, resulting in spin-polarized electrons in the ZnO lattice. The interactions of collective spins in DMS are known as bound magnetic polarons. As magnetic polarons interact with $3d$ cation such as Mn^{2+} within their orbitals, these interactions result in ferromagnetism, when the $3d$ shell of Mn^{2+} is less than half full. Therefore, the overlap of neighboring polarons forms a parallel alignment, resulting in a long-range ferromagnetic interaction. For the coupling between electrons and Mn^{2+} ions, it results in antiferromagnetic ordering when the $3d$ shell in cations are half full or more [13].

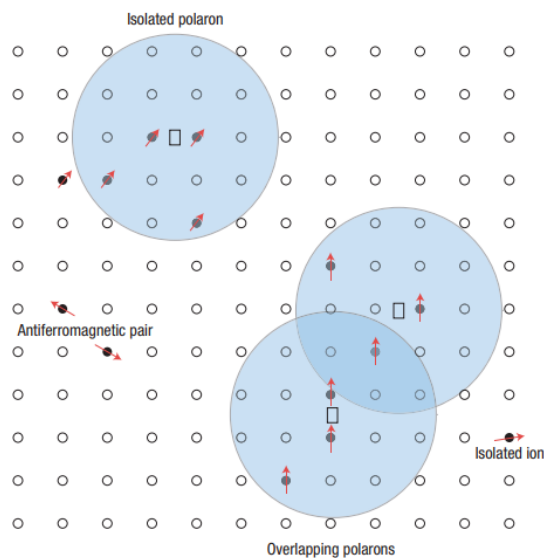


Figure 2. 7 Schematics illustration of bound magnetic polarons. In the presence of magnetic field, O_v form the polarons. The overlap of polarons results in long-range ferromagnetic ordering. The squares represent O_v of ZnO lattice and black circles represented the magnetic ions [13].

2.3 Electric-field manipulation of magnetism

With the strong demand for small, high-density and low-power consumption data storage devices, joule-heating issue become an enormous obstacle for developing magnetic random access memories (MRAM) with increased densities, which is based on spin-transfer torque (STT) to alter the magnetization direction of the spin valve structure [19].



Rather than using electric current for controlling the magnetization in the memory devices, electric-field manipulation of magnetization and tunnel magnetoresistance can be achieved with a current density of 10^4 A/cm², which is 100 times smaller than the current required in STT-MRAM technology, and further incorporates non-volatile functionality [20-23]. Electric-field manipulation of magnetism in memory devices are considered as promising candidates for the next-generation memory technologies with ultralow power consumption, high density and compatible with standard CMOS technologies [24].

In 2000, Ohno. *et al.* first realized electric-field manipulation of ferromagnetism in DMS (In,Mn)As films in the FET geometries (Figure 2. 8 (a)), using thick polyimide as the top gate [25]. The AHE curve in Figure 2. 8 (b) indicates that the ferromagnetic response is switched to a paramagnetic response upon the application of gate voltage (V_g) from -125 to 125 V respectively. This voltage-controlled ferromagnetism is mainly due to the manipulation of hole carriers in (In,Mn)As: a negative V_g increases hole carrier concentration, leading to an increase in the ferromagnetic interaction inside (In,Mn)As, whereas a positive V_g has an opposite effect. Their work (Figure 2. 8 (c)) also demonstrated that T_C of DMS can be manipulated through the hole concentration density.

Inspired by these works, many efforts have been made to replace normal dielectric materials with either ferroelectrics or IL to enhance the tunability of magnetism. The mechanism of electric-field manipulation of ferromagnet (FM) can be classified into the following five categories:

- I. Electrostatic doping
- II. Electrochemical reaction
- III. Exchange coupling
- IV. Strain effect
- V. Orbital reconstruction

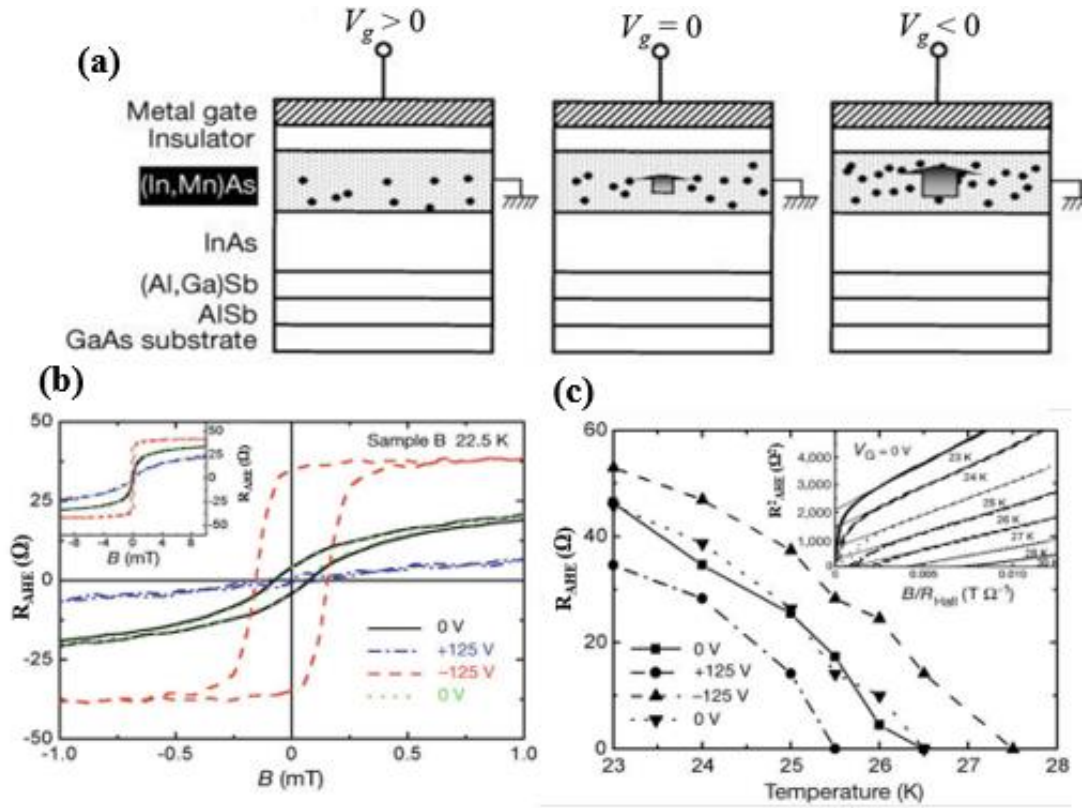


Figure 2. 8 (a) Electric-field manipulation of hole-induced ferromagnetism in DMS (In,Mn)As FET. (b) AHE measurements (R_{AHE} - H curve) under different V_g of 125, 0 and -125 V. (c) Temperature dependence of R_{AHE} under different V_g , R_{AHE}^2 is proportional to the magnetization of (In,Mn)As [25].

2.3.1 Electrostatics doping

Electrostatics effect originates from the electrostatic potential profile induced from dielectrics and liquid electrolytes, or by non-volatile electric polarization of ferroelectric materials. The modulation of magnetism in ferromagnets induced by electric field or polarization is located at the interfacial region between the gate dielectric and the ferromagnet, and the extent of modulation is determined by the screening depth (t_{sd}) within the ferromagnet layer [22, 26]:

$$t_{sd} = (\kappa \hbar^2 / 4me^2)^{\frac{1}{2}} (1/n)^{\frac{1}{6}},$$

where κ is the permittivity of the DMS, n is the carrier density, \hbar is the Planck constant, m and e are the electron mass and charge, respectively. Owing to the low carrier density, electrostatic control of charge carrier density is an effective way to manipulate the magnetism in ferromagnetic semiconductors, since the carrier density in semiconductors is 2-3 orders of magnitude smaller than that in metals. Many reports have demonstrated the modulation of magnetic anisotropy, T_C and coercivity in magnetic semiconductors

[17, 27-29]. In the following sections, the use of normal dielectric, high- k dielectric, ferroelectrics and IL as gating materials are introduced.

1) Dielectric material

Lee. *et. al* first demonstrated the electric-field control of ferromagnetism in (Zn,Co)O system by AHE, using 500 nm-thick SiO_x as the dielectric [15]. AHE revealed that ferromagnetism was induced upon the increase of electron concentration in the depletion layer (Figure 2. 9). This finding showed the ability of manipulating ferromagnetism in ZnO system by electron-mediated exchange interaction through AHE measurement.

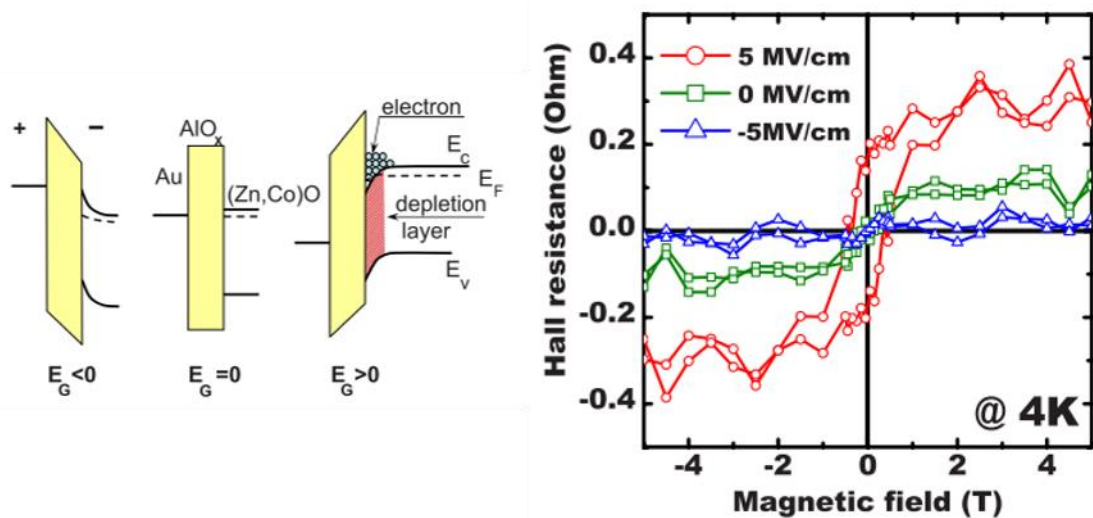


Figure 2. 9 The left hand side is the schematics illustration of energy band diagram for ZnO under different bias electric fields. Positive gate electric field results in the enhancement of ferromagnetic interaction between Co ions (increase electron carrier concentration), whereas negative gate electric field results in the suppression of ferromagnetic interaction (decrease electron carrier concentration). The right side is the field dependence of anomalous Hall resistance (R_{AHE}) for various electric fields (5, 0 and -5 MV/cm), measured at 4 K. Clear hysteresis loop appeared as the positive gate electric field was applied [15].

2) High- k dielectric oxide

To increase the field-induced change in ferromagnetic properties in semiconductors, larger changes in carrier concentration or a larger screening depth upon gating process is needed. Considering the geometry of field-effect transistor, the change in Δn_{2D} can be expressed by the following equations: $\Delta n_{2D} = \frac{CV_g}{e}$, where C is the capacitance per unit area. The capacitance across the gate can be expressed as the following equations; $C = \frac{k\epsilon_0}{d}$, where k is the relative permittivity, ϵ_0 is the permittivity of free space and d is the thickness of the dielectric layer. Therefore, field-effect devices require a high V_g or high

C to obtain a large changes in carrier concentration. A large C value can be achieved by adopting high- k materials such as HfO_2 , MgO , Al_2O_3 and ZrO_2 . Chiba *et. al.* reported the electric-field control of magnetism in perpendicularly magnetized Co/Pt system with 50 nm-thick HfO_2 gate insulator [30] (Figure 2. 10). They not only controlled the coercivity through changing V_g , but also observed a controllable domain-wall velocity from 10^6 to 10^3 ms^{-1} as detected through the magneto-optical Kerr effect (MOKE) microscopy.

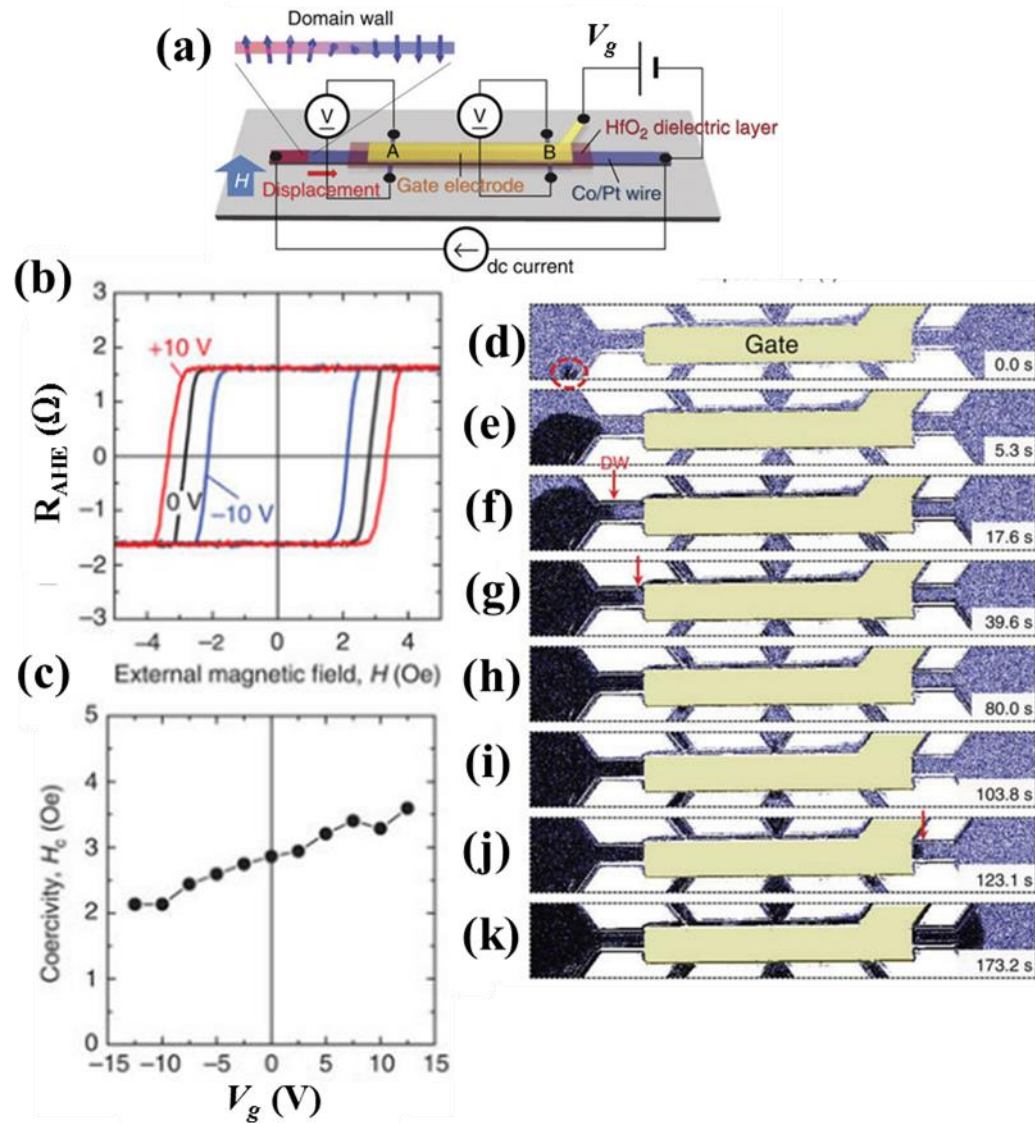


Figure 2. 10 (a) Schematics illustration of the electric-field manipulation in perpendicularly magnetized Co/Pt devices. (b) The field dependence of R_{AHE} measured at 290 K. (d)-(k) Movement of domain-wall as observed by MOKE microscope after a single domain was produced by the application of large negative H . A magnetic field of 170 Oe was applied at $t = 0$ s, for the nucleation of a domain wall. After that, the magnetic field was reduced to 120 Oe. The image shows the domain-wall creep motion as it prorogates from left to right [30].

3) Artificial multiferroic heterostructure

There are limited choices of single-phase materials with a coupling effect between ferroelectricity and ferromagnetism at room temperature [23, 24, 31]. Artificial multiferroic heterostructures are promising alternatives, by depositing a bilayer consisting of FM film coupled with FE film. The non-volatile spontaneous electric polarization at the FE results in carrier accumulation or depletion in FM and hence a change in ferromagnetic properties. Among different FE/FM heterostructures, the coupling between FE and perovskite manganites have attracted lots of attention, since they are potential candidates for spintronic devices with high efficiency [22, 32]. Kanki *et al.* demonstrated electric-field control of T_C in 6 nm-thick $\text{La}_{1-x}\text{Ba}_x\text{MnO}_3$ (LBMO) films through the ferroelectric reversal in $\text{Pb}(\text{Zr}_{0.2}\text{Ti}_{0.8}\text{O}_3)$ (PZT) [33], which is shown in Figure 2. 11. Their results indicated that the shift in T_C was proportional to the magnitude of ferroelectric polarization of PZT, and they attributed the hole accumulation as a main factor for the magnetic change in the LBMO layer.

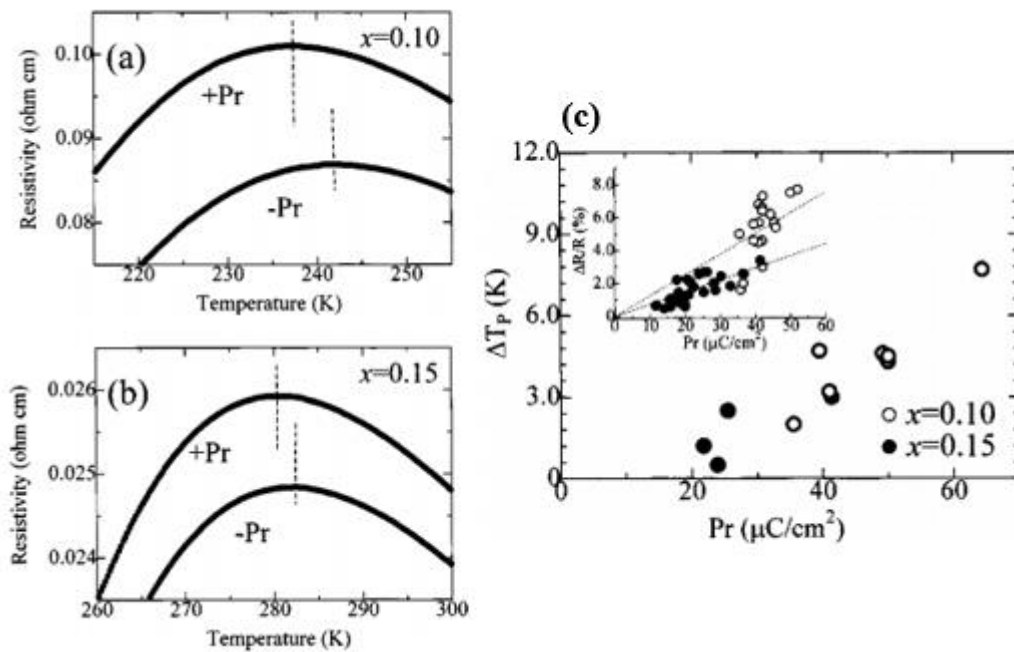


Figure 2. 11 Temperature dependence of LBMO channel resistivity with different ferroelectric polarization reversal in PZT for (a) $x=0.10$ and (b) $x=0.15$. (c) Plot of T_C modulation against the value of ferroelectric remnant polarization with $x=0.1$ (white circle) and $x=0.15$ (black circle). The inset shows the plot of change in channel resistance against the value of ferroelectric remnant polarization, and the linear fit indicates the trend line [33].

4) IL (electrostatic operation)

A large capacitance in the dielectric layer is expected to increase the tunability of the ferromagnetic properties. The non-conventional approach uses IL as electrolytes which contains mobile anion and cations. As V_g is applied, an EDL is formed, then cations and anions are attracted electrostatically between the ferromagnet channel and the gate electrode. Therefore, accumulated or depleted charge carriers are achieved in the ferromagnetic channel upon the polarity change of V_g . A larger C value can be achieved since the gap of two charged sheet in the EDL capacitor is approximately 1 nm [34]. As a result, a larger change in carrier density is expected.

EDL capacitors have been widely used for manipulation of transport and magnetic properties of ferromagnet. Dhoot *et al.* demonstrated the electric-field manipulation of magnetism in $\text{La}_{0.8}\text{Ca}_{0.2}\text{MnO}_3$ (LCMO) [35] (Figure 2. 12). For a positive V_g , electron doping from IL (cation: EMIM⁺; anion: TFSI⁻) drives the manganite layer from a ferromagnetic to an insulating state in LCMO. The electron-doped layer ($V_g = +3\text{V}$) can extend to 5 nm within the LCMO layer, requiring an electric-field doping of 2×10^{15} charges per cm^2 , which is equivalent to 2.5 electrons per unit cell area. For negative V_g , the metallic conductivity can be increased by 30 %.

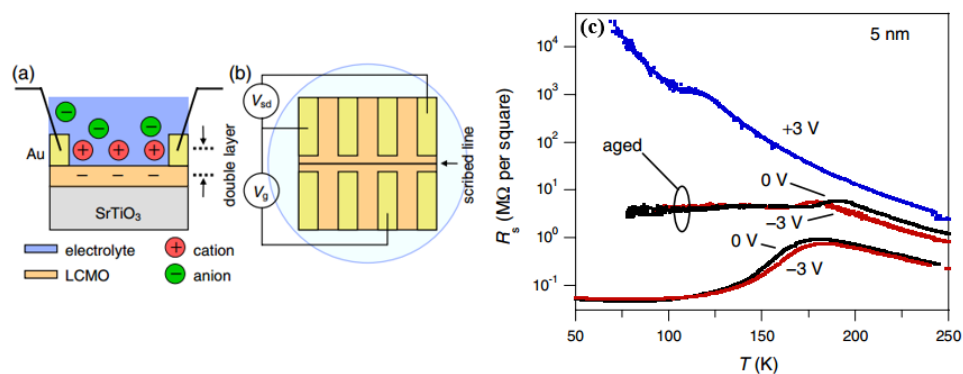


Figure 2. 12 Schematics illustration of LCMO field-effect devices gated with EDL, (a) for the application of position gate voltage. (b) the top view of devices. (c) temperature dependence of 5 nm-thick LCMO sheet resistance gated with ionic liquid with different V_g (3 V: blue line, 0 V: black line and -3 V: red line) [35].

2.3.2 Electrochemical reaction

Charge screening in the ferromagnets tend to confine the electrostatic effect at the gate electrode/ferromagnet interface region, and hence reduce the tunability of ferromagnetism in the channel as the film thickness is increased. Alternatively, the



electric-field-driven redox reaction in the ferromagnet is a promising method for the manipulation of magnetism in thicker films. The redox reaction is based on the changes in the chemical states, which can either be partially reversible or completely irreversible reaction.

1) IL (electrochemical reaction)

It was experimentally proved that the charge accumulation and depletion mechanism between IL and ferromagnet interfaces changes from electrostatic doping ($C \approx 10\mu F cm^{-2}$) to electrochemical reaction ($C \approx 10^3\mu F cm^{-2}$) with the increase of V_g [36]. These electrochemical reactions are useful for robustly manipulating the magnetism in any ferromagnetic system. Cui *et al.* demonstrated that the manipulation of phase separation in LSMO was controlled via the IL gating process [37]. TEM and MR results (Figure 2. 13) indicated the formation of an insulating and magnetic matrix in the ferromagnetic layer. Through the variation in $Mn^{4+}/(Mn^{3+}+Mn^{4+})$, dislocation density and magnetotransport measurement, it is demonstrated that the controllable V_g would cause the formation of insulating and magnetic matrices in the ferromagnetic layer, further leading to a T_C change up to 70 K in literature.

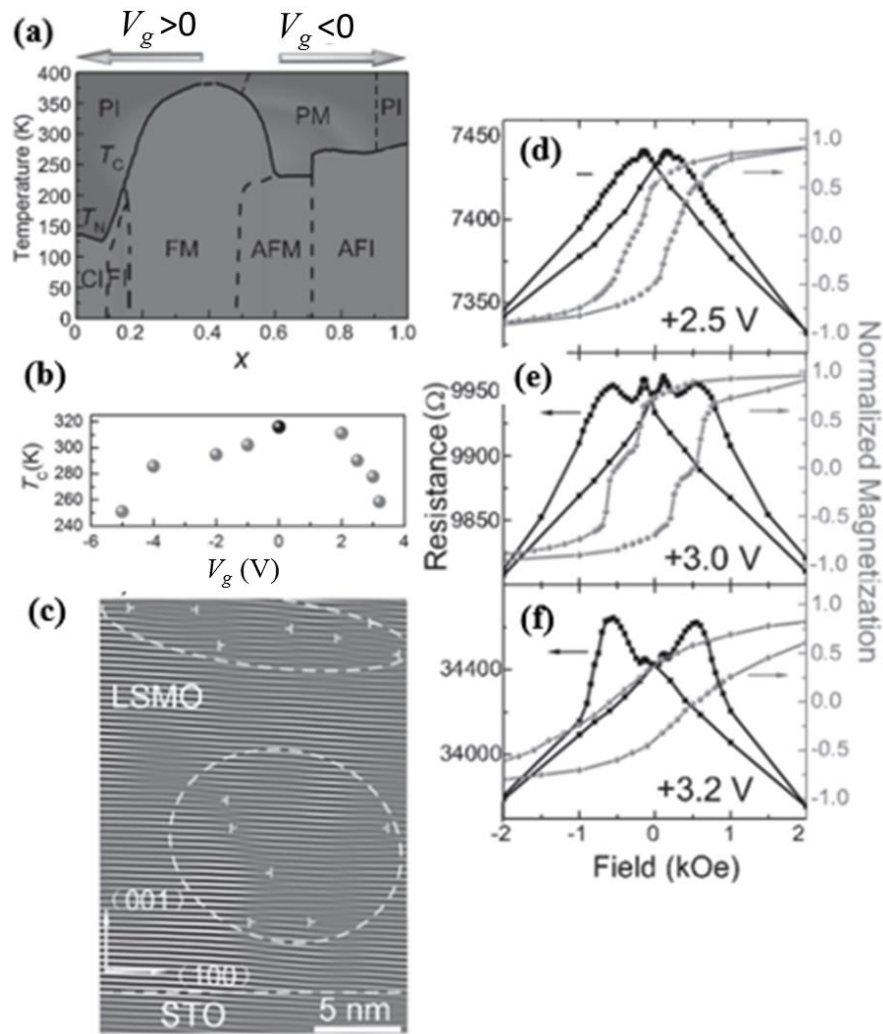


Figure 2. 13 (a) Phase diagram of $La_{1-x}Sr_xMnO_3$ with different Sr doping concentration (x), where the abbreviations are spin-canted insulating (CI), ferromagnetic insulating (FI), ferromagnetic metal (FM), antiferromagnetic metal (AFM), antiferromagnetic insulating (AFI), paramagnetic insulating (PI), and paramagnetic metal (PM) phases. (b) Temperature dependence of LSMO channel resistance as a function of V_g (c) Fourier-filtered images of LSMO sample with the application of $V_g=3$ V. \perp and dashed ovals highlights the dislocations sites and regions with high dislocation densities, respectively. (d) to (f): MR (left axis) and normalized magnetization (right axis) recorded with sweeping magnetic fields along the LSMO channel direction under different V_g : (d) 2.5 V, (e) 3 V and (f) 3.2V [37].

Electric-field-reversible manipulation of T_c and magnetism were demonstrated in 4 nm-thick $SrRuO_3$ (SRO) films with FET geometry [38], as shown in Figure 2. 14. In these SRO FETs, T_c and MR measurements can be reversibly manipulated in range from 90-250 K and 70-100 K by the application of V_g less than 2.2 V. Electric-field manipulation of magnetism in SRO were suggested to originate from the reversible-diffusion process of oxygen ions in SRO lattice.

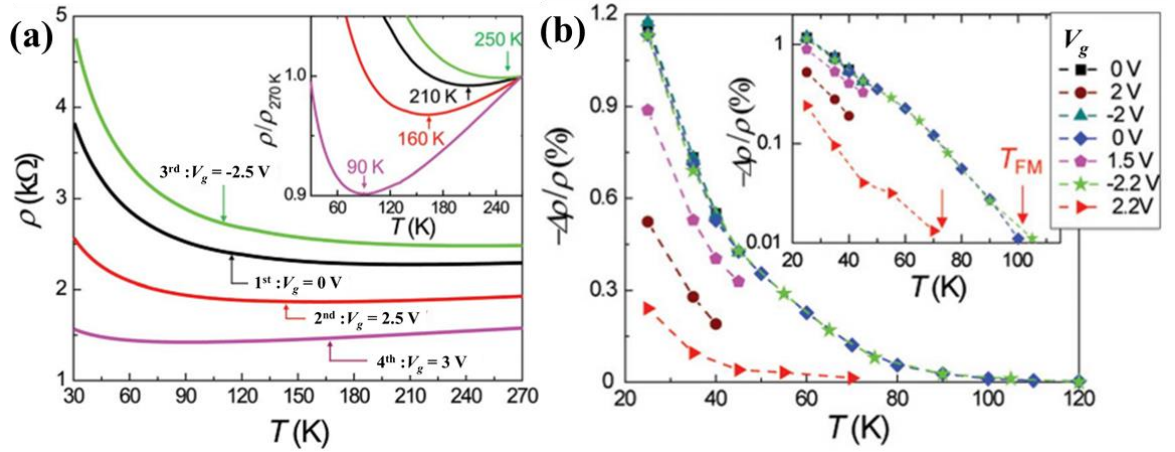


Figure 2. 14 (a) Temperature dependence of 4 nm-thick SRO thin with different V_g of -2.5, 0, 2.5 and 3 V, (b) Temperature dependence of MR ($\frac{\Delta\rho}{\rho}$), which is obtained in 0.5 T with different V_g . The inset is the semi-log plot of data, where T_{FM} is defined as the metal-to-insulator temperature of SRO [38].

2) Voltage-induced oxidation

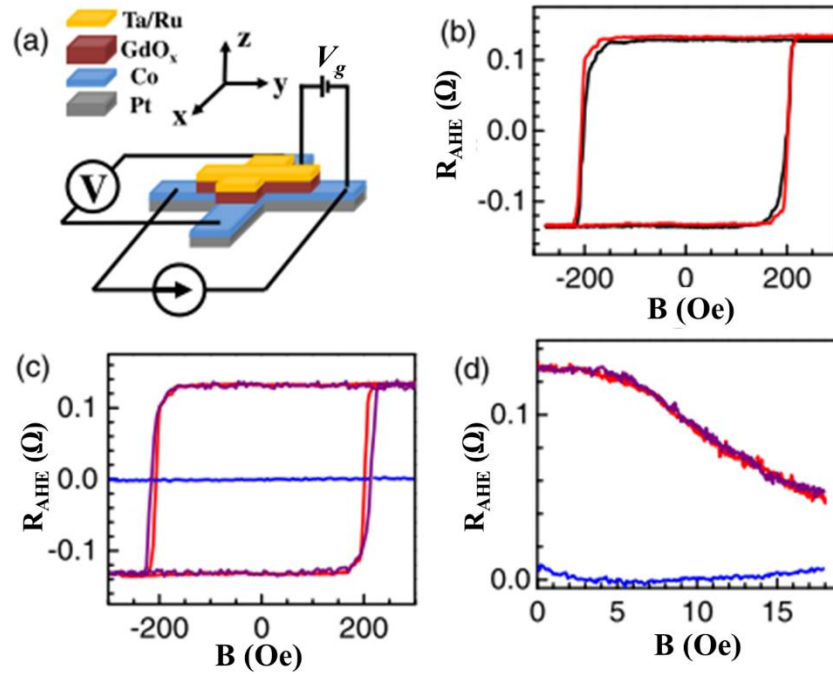


Figure 2. 15 (a) Schematic illustration of Co/GdO_x field-effect devices. (b) AHE measurements (R_{AHE} -H curve) of the Co devices in the as-deposited state and after holding at 200 °C for 10 mins, which are indicated as black and red lines, respectively. (c) AHE measurements (R_{AHE} - B) of the Co devices after the application of electric field of -625 kV/cm for 6 mins (blue line) and +625 kV/cm for 13 mins at 200 °C. The red line is the same as in (b). Planar Hall effect (R_{AHE} - B) measurement with the magnetic field parallel to the applied current direction [39].

Electric-field manipulation of magnetic properties in Co films adjacent to Gd_2O_3 gate oxides were demonstrated by Bi *et al.* [39], as shown in Figure 2. 15. Using the strong oxygen affinity of gadolinium oxide [40], oxygen ions can be reversibly migrated into/out of the Co film. Their results indicate that Co films can be reversibly manipulated from ferromagnets with strong perpendicular magnetic anisotropy (metallic state) to one with zero magnetization, depending on the polarity and duration in which V_g was applied.

2.3.3 Exchange coupling

The observed phenomena of electric-field manipulation of magnetism in antiferromagnet (AF) have been subjected to intensive investigations [31, 41-43]. Experiments have successfully manipulated the AF spins through different mechanisms such as magnetoelectric coupling [41-43] and carrier accumulation from ionic liquid [44].

1) Magnetoelectric coupling

In 2005, magnetoelectric-induced antiferromagnetic changes in Cr_2O_3 were first reported in the heterostructure of Cr_2O_3 (111)/(Co/Pt)₃ [41]. Under the application of magnetic field and electric field (E), the antiferromagnetic domain switched some uncompensated pinned spin at the interfacial region between Cr_2O_3 and (Co/Pt)₃, as shown in Figure 2. 16.

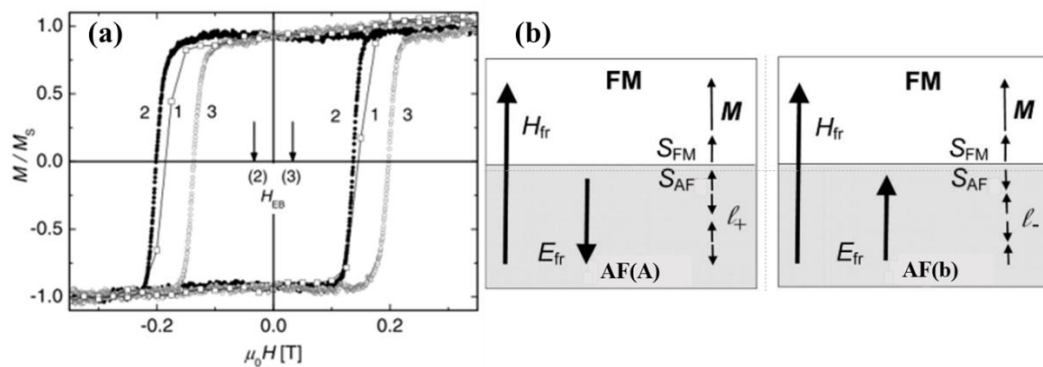


Figure 2. 16 (a) Normalized hysteresis loop of Cr_2O_3 (111)/Pt (0.5 nm)/[Co (0.3 nm)/Pt (1.5 nm)]₃ Pt (1.5 nm) recorded after field-cooling process (0.6 T, $E=0$), which is measured from 350 to 298 K (labelled as (1)), and after field-cooling process to 250 K (0.6 T, $E= -500$ kV/m) and (0.6 T, $E=500$ kV/m) (labelled as (2) and (3), respectively). (b) and (c) Schematics illustrations of Cr_2O_3 (111)/(Co/Pt)₃ with field cooling (H_{fr}), showing different polarities of electric field on Cr_2O_3 ($\pm E_{fr}$), order parameter (M , I_{\pm}) and magnetic moment in FM and AFM (S_{FM} , S_{AF}) where AF is single domains after magnetoelectric switching and field cooling process [41].

Wu *et al.* demonstrated the electric-field control of exchange-bias effect through a field-effect device with 600 nm-thick BiFeO₃ (BFO) and 3 nm-thick La_{0.7}Sr_{0.3}MnO₃ [42], as shown in Figure 2. 17. Upon the application of electric field and switching the polarization direction of BFO, a reversible switching of exchange bias (EB) between two distinct states was observed at 180 K.

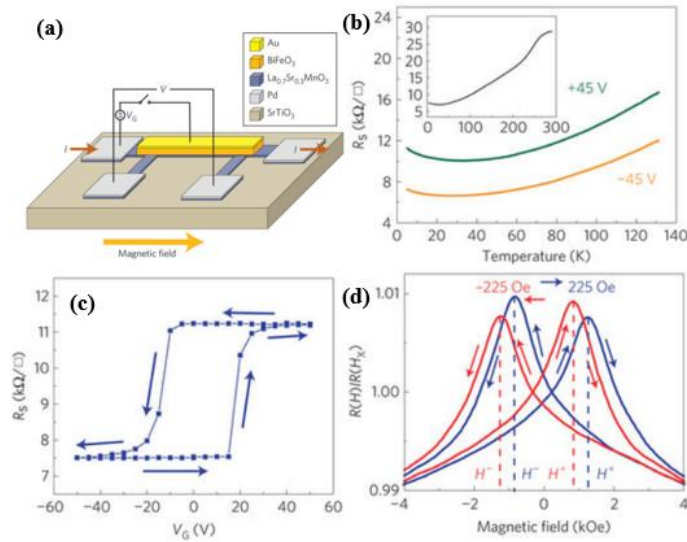


Figure 2. 17 (a) Schematics diagram of BFO/La_{0.7}Sr_{0.3}MnO₃ field-effect devices. (b) Temperature dependence of sheet resistance with different ferroelectric directions of BFO. (c). Changes in sheet resistance as a function of V_g measured at 180 K. (d) Magnetoresistance measurement after field-cooling process with 1 T, and measured at 180 K. Two distinct exchange-bias states were observed after switching the ferroelectric direction of BFO [42].

2.3.4 Strain coupling

Strain coupling is a conventional method to control the magnetism for ferromagnetic materials grown on ferroelectric substrates such as BTO [45] and PMN-PT [46]. The control of FM properties can be classified into two different mechanisms.

1) Converse piezoelectric effect from ferroelectric crystal (piezo-strain): As the external electric field is applied to the ferroelectric crystal or substrate, the lattice dimension of the ferroelectric is altered and transfers the strain to the FM layer, resulting in a change in magnetic anisotropy, coercivity and T_C by magnetostriction. This electric-field induced strain to FM layer (Figure 2. 18) leads to a butterfly-loop shape in magnetization-electric-field measurement, which has similar shape in the relationships between in-plane strain and applied electric field: i.e. the electric-field-induced strain to FM layer is volatile [46].

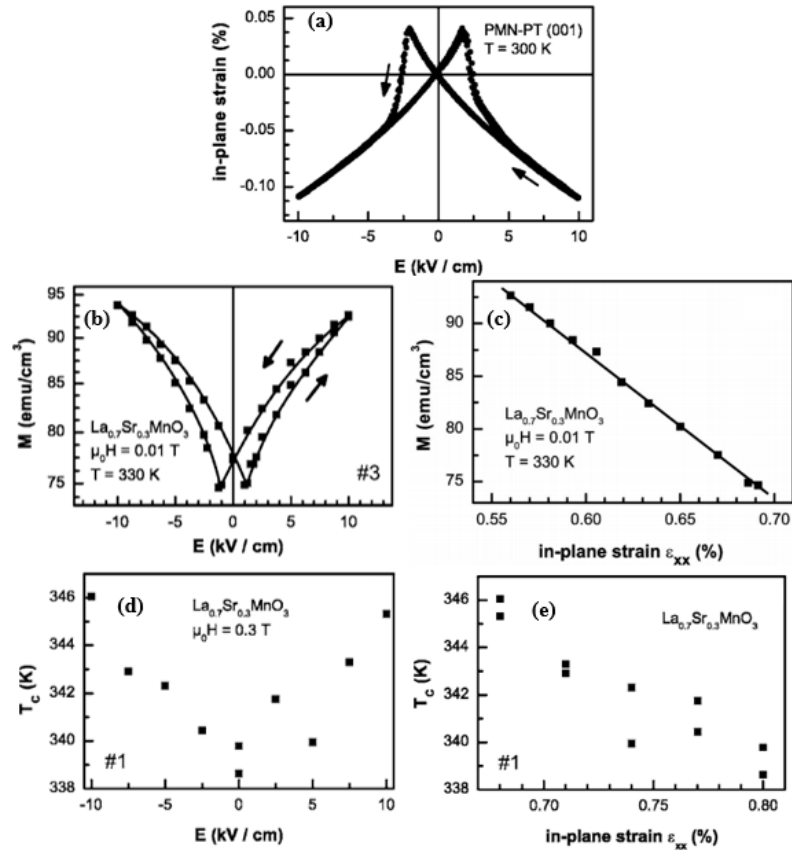


Figure 2. 18 (a) Relationship between in-plane strain of (001) oriented PMN-PT with $x=0.28$ and applied electric field along [001] direction. (b) Magnetization of LSMO at $T = 330$ K against electric field along [001] direction. (c) Magnetization of LSMO against in-plane strain. (d) T_C of LSMO as a function of applied electric field. (e) T_C of LSMO as a function of in-plane strain [46].

2) Charge-mediated mechanism (ferroelectric-strain): If the applied electric field is larger than the coercivity field of the ferroelectric substrate, the manipulation of magnetism by FE is mainly due to the accumulated/depleted charge carriers FM/FE interface. Usually an electric field of a few hundred volts are required to switch the FE polarization. The reversible hysteresis-loops curves such as resistance-electric field (R-E) and magnetization-electric field (M-E) measurements are used to indicate the manipulation of magnetism with non-volatile behavior [47], as shown in Figure 2. 19.

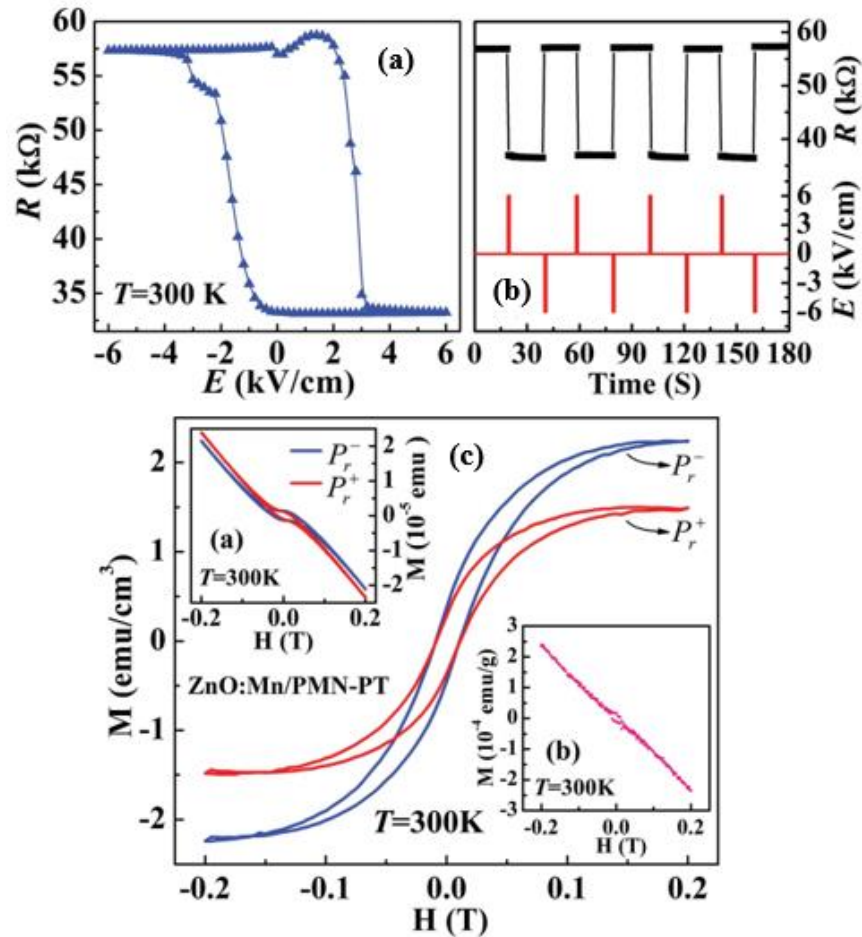


Figure 2. 19 (a) Change of $Zn_{0.96}Mn_{0.04}O$ resistance with bipolar electric field applied across $Zn_{0.96}Mn_{0.04}O/PMN-PT$ heterostructure. (b) Non-volatile behavior in resistance-switching effect of $Zn_{0.96}Mn_{0.04}O/PMN-PT$ heterostructure by the application of pulse voltages. (c) Magnetic hysteresis loops of the $Zn_{0.96}Mn_{0.04}O$ films after subtracting the background from the substrate; the red and blue lines are loops switched with positive and negative polarization direction respectively. The upper inset is $M-H$ loop without subtracting contribution from the substrate. The lower inset is $M-H$ loop after removal $Zn_{0.96}Mn_{0.04}O$ from $PMN-PT$ substrate [47].

2.3.5 Orbital reconstruction

The change in orbital hybridization at the FM interfaces through gating with FE or dielectric has a great impact on the magnetism in FM. Electrical-field manipulation of magnetic anisotropy in MgO (10 nm)/ Fe (0.48 nm) were demonstrated [48], as shown in Figure 2. 20. Based on the measurement of magneto-optical Kerr ellipticity (η_K), the increase in perpendicular anisotropy of Fe layer were observed upon the application of V_g changes from 200 to -200V. Manipulation of magnetism in Fe layer is concluded due to the $3d$ orbital occupation alterations.

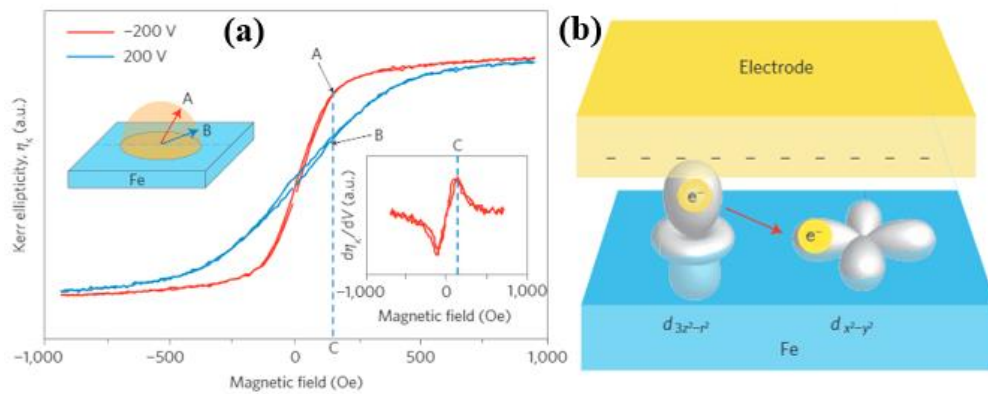


Figure 2. 20 (a) Magneto-optical Kerr ellipticity (η_{κ}) with applied voltages of 200 and -200V, as a function of magnetic field. The upper inset is the schematic diagram of magnetization direction of point A and B. The lower inset is the voltage manipulation of Kerr ellipticity, $\frac{d\eta_{\kappa}}{dV}$. (b) Schematics illustration of electric-field effect on electron filling of the 3d orbitals in ultrathin Fe layer [48].

Subsequently, Radaelli *et al.* demonstrated that electric-field control of interfacial magnetism in the Fe/BTO [49], as shown in Figure 2. 21. X-ray magnetic circular dichroism (XMCD) measurements revealed that oxidized interfacial FeO_x shows an enhanced magnetism as the ferroelectric polarization of BTO was switched to upward directions. These findings provided microscopic information on how the interfacial level of the artificial magnetoelectric system is controlled through the electrical switching of BTO polarization.

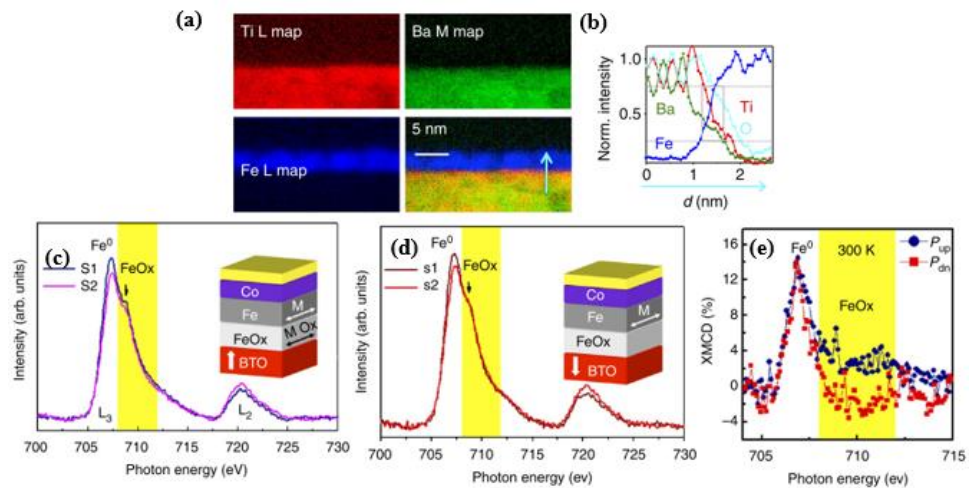


Figure 2. 21 TEM images of Au (4 nm)/Fe (1 nm)/BTO (150nm)/LSMO (50 nm) on STO (001). (a) Elemental mapping analysis. (b) Elemental profiles acquired from electron energy loss spectroscopy (ELLS) line scans, showing a significant amount of O outside the BTO layer. X-ray absorption spectroscopy (XAS) Fe-L_{2,3} spectra obtained from Au/Co/Fe(2 monolayers)/BTO/LSMO on (001) STO at 300 K, after polarization of BTO with (c) $V^+ = 5V$ (P_{up}) and (d) $V^- = -5V$ (P_{down}). (e) XMCD signal from Fe-L₃ energy region for different polarization directions; the yellow region indicates the oxidized Fe layer adjacent with BTO layer [49].

2.1 Conclusion

This Chapter introduced the concepts of LSMO and ZnO. The different methods of electric-field control of magnetism through electrostatic doping, electrochemical reaction, exchange coupling, strain effect and orbital reconstruction was also introduced.



References for Chapter 2

- [1] A.M. Haghiri-Gosnet, J.P. Renard, CMR manganites: physics, thin films and devices, *Journal of Physics D: Applied Physics*, 36 (2003) R127.
- [2] T. Brückel, Neutron Scattering Lectures of the JCNS Laboratory Course held at Forschungszentrum Jülich and at the Heinz Maier-Leibnitz Zentrum Garching In cooperation with RWTH Aachen and University of Münster, Forschungszentrum Jülich, Zentralbibliothek 2013.
- [3] C. Zener, Interaction between the *d*-Shells in the Transition Metals. II. Ferromagnetic Compounds of Manganese with Perovskite Structure, *Physical Review*, 82 (1951) 403-405.
- [4] G.H. Thomas Brückel, Dieter Richter, Georg Roth, Reiner Zorn, Neutron Scattering lectures of the JCNS Laboratory Course held at Forschungszentrum Jülich and at the Heinz Maier-Leibnitz Zentrum Garching. In cooperation with RWTH Aachen and University of Münster, Jülich Forschungszentrum Jülich, Zentralbibliothek 2014/2014.
- [5] J.B. Goodenough, Theory of the Role of Covalence in the Perovskite-Type Manganites (La,M(II))MnO₃, *Physical Review*, 100 (1955) 564-573.
- [6] J. Kanamori, Superexchange interaction and symmetry properties of electron orbitals, *Journal of Physics and Chemistry of Solids*, 10 (1959) 87-98.
- [7] A. Urushibara, Y. Moritomo, T. Arima, A. Asamitsu, G. Kido, Y. Tokura, Insulator-metal transition and giant magnetoresistance in La_{1-x}Sr_xMnO₃, *Physical Review B*, 51 (1995) 14103-14109.
- [8] J. Hemberger, A. Krimmel, T. Kurz, H.A. Krug von Nidda, V.Y. Ivanov, A.A. Mukhin, A.M. Balbashov, A. Loidl, Structural, magnetic, and electrical properties of single-crystalline La_{1-x}Sr_xMnO₃ (0.4 < x < 0.85), *Physical Review B*, 66 (2002) 094410.
- [9] V.A. Coleman, C. Jagadish, Chapter 1 - Basic Properties and Applications of ZnO, *Zinc Oxide Bulk, Thin Films and Nanostructures*, Elsevier Science Ltd, Oxford, 2006, pp. 1-20.
- [10] J.C. Fan, K.M. Sreekanth, Z. Xie, S.L. Chang, K.V. Rao, p-Type ZnO materials: Theory, growth, properties and devices, *Progress in Materials Science*, 58 (2013) 874-985.
- [11] B.T. Matthias, R.M. Bozorth, J.H. Van Vleck, Ferromagnetic Interaction in EuO, *Physical Review Letters*, 7 (1961) 160-161.
- [12] T. Dietl, H. Ohno, F. Matsukura, J. Cibert, D. Ferrand, Zener Model Description of Ferromagnetism in Zinc-Blende Magnetic Semiconductors, *Science*, 287 (2000) 1019-1022.
- [13] J.M.D. Coey, M. Venkatesan, C.B. Fitzgerald, Donor impurity band exchange in dilute ferromagnetic oxides, *Nat Mater*, 4 (2005) 173-179.
- [14] N. Nepal, M.O. Luen, J.M. Zavada, S.M. Bedair, P. Frajtag, N.A. El-Masry, Electric field control of room temperature ferromagnetism in III-N dilute magnetic semiconductor films, *Applied Physics Letters*, 94 (2009) 132505.
- [15] H.-J. Lee, E. Helgren, F. Hellman, Gate-controlled magnetic properties of the magnetic semiconductor (Zn,Co)O, *Applied Physics Letters*, 94 (2009) 212106.
- [16] H.W. Chang, S. Akita, F. Matsukura, H. Ohno, Hole concentration dependence of the Curie temperature of (Ga,Mn)Sb in a field-effect structure, *Applied Physics Letters*, 103 (2013) 142402.
- [17] D. Chiba, F. Matsukura, H. Ohno, Electric-field control of ferromagnetism in (Ga,Mn)As, *Applied Physics Letters*, 89 (2006) 162505.



- [18] Y. Yamada, K. Ueno, T. Fukumura, H.T. Yuan, H. Shimotani, Y. Iwasa, L. Gu, S. Tsukimoto, Y. Ikuhara, M. Kawasaki, Electrically Induced Ferromagnetism at Room Temperature in Cobalt-Doped Titanium Dioxide, *Science*, 332 (2011) 1065-1067.
- [19] D.C. Ralph, M.D. Stiles, Spin transfer torques, *Journal of Magnetism and Magnetic Materials*, 320 (2008) 1190-1216.
- [20] F. Matsukura, Y. Tokura, H. Ohno, Control of magnetism by electric fields, *Nat. Nanotech*, 10 (2015) 209-220.
- [21] D. Chiba, T. Ono, Control of magnetism in Co by an electric field, *Journal of Physics D: Applied Physics*, 46 (2013) 213001.
- [22] S. Cheng, C. Bin, P. Jingjing, M. Haijun, P. Feng, Electrical control of magnetism in oxides, *Chinese Physics B*, 25 (2016) 067502.
- [23] C. Song, B. Cui, F. Li, X. Zhou, F. Pan, Recent progress in voltage control of magnetism: Materials, mechanisms, and performance, *Progress in Materials Science*, 87 (2017) 33-82.
- [24] M. Liu, N.X. Sun, Voltage control of magnetism in multiferroic heterostructures, *Philos. Trans. Royal Soc. A*, 372 (2014).
- [25] H. Ohno, D. Chiba, F. Matsukura, T. Omiya, E. Abe, T. Dietl, Y. Ohno, K. Ohtani, Electric-field control of ferromagnetism, *Nature*, 408 (2000) 944-946.
- [26] A.N.W.a.M.N. D, *Solid State Physics*, Toronto Thomson Learning 1976.
- [27] D. Chiba, Y. Nakatani, F. Matsukura, H. Ohno, Simulation of magnetization switching by electric-field manipulation of magnetic anisotropy, *Applied Physics Letters*, 96 (2010) 192506.
- [28] P. Balestriere, T. Devolder, J. Wunderlich, C. Chappert, Electric field induced anisotropy modification in (Ga,Mn)As: A strategy for the precessional switching of the magnetization, *Applied Physics Letters*, 96 (2010) 142504.
- [29] D. Chiba, A. Werpachowska, M. Endo, Y. Nishitani, F. Matsukura, T. Dietl, H. Ohno, Anomalous Hall Effect in Field-Effect Structures of (Ga,Mn)As, *Physical Review Letters*, 104 (2010) 106601.
- [30] D. Chiba, M. Kawaguchi, S. Fukami, N. Ishiwata, K. Shimamura, K. Kobayashi, T. Ono, Electric-field control of magnetic domain-wall velocity in ultrathin cobalt with perpendicular magnetization, 3 (2012) 888.
- [31] Q. Yang, Z. Zhou, N.X. Sun, M. Liu, Perspectives of voltage control for magnetic exchange bias in multiferroic heterostructures, *Physics Letters A*, 381 (2017) 1213-1222.
- [32] V. Laukhin, V. Skumryev, X. Martí, D. Hrabovsky, F. Sánchez, M.V. García-Cuenca, C. Ferrater, M. Varela, U. Lüders, J.F. Bobo, J. Fontcuberta, Electric-Field Control of Exchange Bias in Multiferroic Epitaxial Heterostructures, *Physical Review Letters*, 97 (2006) 227201.
- [33] T. Kanki, Y.-G. Park, H. Tanaka, T. Kawai, Electrical-field control of metal-insulator transition at room temperature in $\text{Pb}(\text{Zr}_{0.2}\text{Ti}_{0.8})\text{O}_3/\text{La}_{1-x}\text{Ba}_x\text{MnO}_3$ field-effect transistor, *Applied Physics Letters*, 83 (2003) 4860-4862.
- [34] R. Yamamoto, H. Morisaki, O. Sakata, H. Shimotani, H. Yuan, Y. Iwasa, T. Kimura, Y. Wakabayashi, External electric field dependence of the structure of the electric double layer at an ionic liquid/Au interface, *Applied Physics Letters*, 101 (2012) 053122.
- [35] A.S. Dhoot, C. Israel, X. Moya, N.D. Mathur, R.H. Friend, Large Electric Field Effect in Electrolyte-Gated Manganites, *Physical Review Letters*, 102 (2009) 136402.
- [36] A. Molinari, P.M. Leufke, C. Reitz, S. Dasgupta, R. Witte, R. Kruk, H. Hahn, Hybrid supercapacitors for reversible control of magnetism, 8 (2017) 15339.
- [37] B. Cui, C. Song, G. Wang, Y. Yan, J. Peng, J. Miao, H. Mao, F. Li, C. Chen, F. Zeng, F. Pan, Reversible Ferromagnetic Phase Transition in Electrode-Gated Manganites, *Advanced Functional Materials*, 24 (2014) 7233-7240.



- [38] H.T. Yi, B. Gao, W. Xie, S.-W. Cheong, V. Podzorov, Tuning the metal-insulator crossover and magnetism in SrRuO₃ by ionic gating, *Scientific Reports*, 4 (2014) 6604.
- [39] C. Bi, Y. Liu, T. Newhouse-Illige, M. Xu, M. Rosales, J.W. Freeland, O. Mryasov, S. Zhang, S.G.E. te Velthuis, W.G. Wang, Reversible Control of Co Magnetism by Voltage-Induced Oxidation, *Physical Review Letters*, 113 (2014) 267202.
- [40] D.A. Gilbert, J. Olamit, R.K. Dumas, B.J. Kirby, A.J. Grutter, B.B. Maranville, E. Arenholz, J.A. Borchers, K. Liu, Controllable positive exchange bias via redox-driven oxygen migration, 7 (2016) 11050.
- [41] P. Borisov, A. Hochstrat, X. Chen, W. Kleemann, C. Binek, Magnetolectric Switching of Exchange Bias, *Physical Review Letters*, 94 (2005) 117203.
- [42] S.M. Wu, S.A. Cybart, P. Yu, M.D. Rossell, J.X. Zhang, R. Ramesh, R.C. Dynes, Reversible electric control of exchange bias in a multiferroic field-effect device, *Nat. Mater.*, 9 (2010) 756-761.
- [43] S.M. Wu, S.A. Cybart, D. Yi, J.M. Parker, R. Ramesh, R.C. Dynes, Full Electric Control of Exchange Bias, *Physical Review Letters*, 110 (2013) 067202.
- [44] Y. Wang, X. Zhou, C. Song, Y. Yan, S. Zhou, G. Wang, C. Chen, F. Zeng, F. Pan, Electrical Control of the Exchange Spring in Antiferromagnetic Metals, *Advanced Materials*, 27 (2015) 3196-3201.
- [45] S. Sahoo, S. Polisetty, C.-G. Duan, S.S. Jaswal, E.Y. Tsymlal, C. Binek, Ferroelectric control of magnetism in BaTiO₃/Fe heterostructures via interface strain coupling, *Physical Review B*, 76 (2007) 092108.
- [46] C. Thiele, K. Dörr, O. Bilani, J. Rödel, L. Schultz, Influence of strain on the magnetization and magnetoelectric effect in La_{0.7}A_{0.3}MnO₃/PMN-PT(001) (A=Sr,Ca), *Physical Review B*, 75 (2007) 054408.
- [47] Q.-X. Zhu, M.-M. Yang, M. Zheng, R.-K. Zheng, L.-J. Guo, Y. Wang, J.-X. Zhang, X.-M. Li, H.-S. Luo, X.-G. Li, Ultrahigh Tunability of Room Temperature Electronic Transport and Ferromagnetism in Dilute Magnetic Semiconductor and PMN-PT Single-Crystal-Based Field Effect Transistors via Electric Charge Mediation, *Advanced Functional Materials*, 25 (2015) 1111-1119.
- [48] MaruyamaT, ShiotaY, NozakiT, OhtaK, TodaN, MizuguchiM, A.A. Tulapurkar, ShinjoT, ShiraishiM, MizukamiS, AndoY, SuzukiY, Large voltage-induced magnetic anisotropy change in a few atomic layers of iron, *Nat Nano*, 4 (2009) 158-161.
- [49] G. Radaelli, D. Petti, E. Plekhanov, I. Fina, P. Torelli, B.R. Salles, M. Cantoni, C. Rinaldi, D. Gutiérrez, G. Panaccione, M. Varela, S. Picozzi, J. Fontcuberta, R. Bertacco, Electric control of magnetism at the Fe/BaTiO₃ interface, *Nature communications*, 5 (2014) 3404-3404.



Chapter 3 Experimental techniques

This Chapter describes the key techniques used for the fabrication and characterization of epitaxial thin films. Firstly, details of substrate surface treatment before the thin film deposition are explained, followed by an introduction on pulsed laser deposition (PLD). Next, a brief description of the device fabrication with Hall-bar pattern is provided. In the final part, the experimental techniques that are employed to characterize the electrical and magnetic properties of the heterostructures are introduced.

3.1 Substrate surface treatment

3.1.1 Strontium titanate substrates

Strontium titanate (STO) has the perovskite structure of ABO_3 with a pseudo-cubic lattice constant of 3.905 \AA . LSMO films prepared by PLD exhibit a layer-by-layer growth pattern with a step height of 3.9 \AA , which is close to the lattice parameter of STO lattice. The small lattice mismatch between LSMO and STO substrate is suitable for the growth of high-quality LSMO thin films.

Many reports have shown that the device performance of oxide films, such as 2D electron gas at the LAO/STO interface, strongly depends on the film/substrate interface quality [1, 2]. However, surfaces of commercially-purchased STO substrates typically contain both SrO and TiO_2 -terminating planes along the (001) direction. The preparation of STO substrates with single termination is an important step for growing high-quality thin films. For our LSMO films, I used TiO_2 -terminated STO substrates to fabricate the LSMO films for several reasons:

- The interfacial quality between STO substrate and LSMO film can be well-controlled.
- TiO_2 -terminated STO substrates are chemically more stable in various acids and even in water than those with SrO termination [2].

STO (001) substrates with a mixture of SrO and TiO_2 terminations and miscut angle $<0.5^\circ$ were purchased from HeFei-Kejing in China (Figure 3. 1 (a)). Due to the safety issue related to the use of buffered hydrofluoric acid (BHF) [3], deionized (DI) water etching and thermal treatment were employed to achieve the TiO_2 -termination on the STO substrates [4, 5]. Firstly, as-received substrates were ultrasonically cleaned by acetone and ethanol, in order to remove organic impurities on the surface. And then the substrates were annealing at 1000°C in air for 2 hours (1st thermal annealing process). Boiling DI



water was then used for etching, as SrO is readily soluble in water and hence the process can enhance the etching selectivity of SrO layers. As a final cleaning step, the substrates were subjected to annealing at 1000°C in air for another 2 hours (2nd thermal annealing process). Figure 3. 1 (b) show the AFM image after DI water treatment and the thermal annealing processes. As in contrast with as-purchased substrates, atomically-flat substrates with clear step-terraced surfaces were obtained. The step height is equivalent to the height of a single STO cell along the (001) direction (Figure 3. 1 (c)).

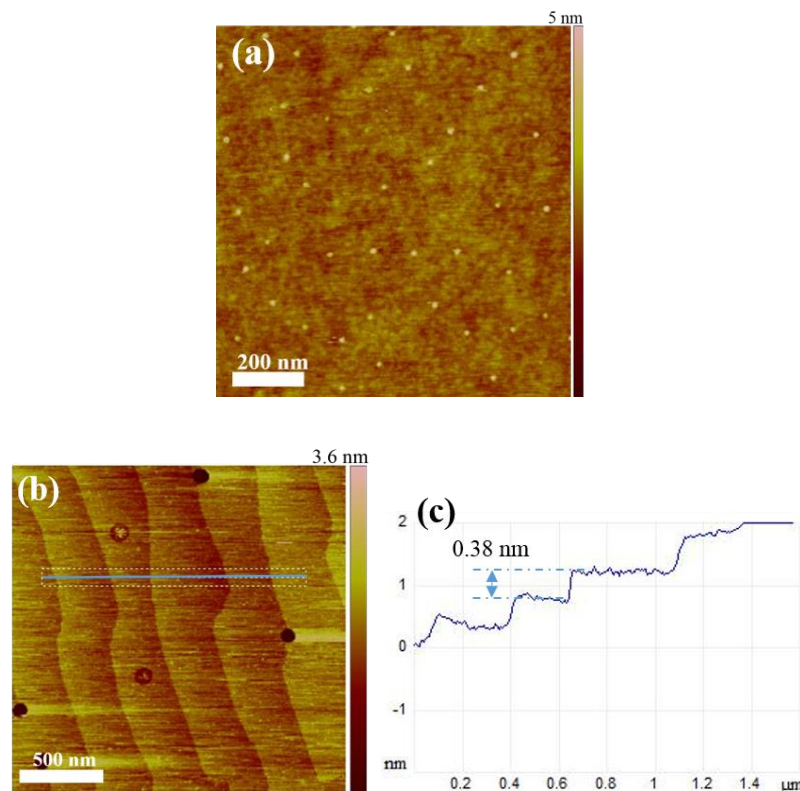


Figure 3. 1 Surface morphology of STO (001) substrate in different states: (a) as-received, and (b) after a series of substrate treatment processes. (c) shows the line profile along the line in Figure 3. 1 (b)

3.2 Pulsed laser deposition

Epitaxial growth of LSMO films and $Zn_{0.92}Mn_{0.08}O$ films were prepared by PLD. Figure 3. 2 shows a schematic diagram of the PLD system, with the main components of UV excimer laser, vacuum system, substrate heater stage and target. The mechanism of PLD involves the use of tightly-focused high-energy laser pulses to hit on the target in vacuum. Due to the high energy of the laser pulses, target materials are vaporized on the surface and a plume containing atoms, molecules, ions, electrons and large particulates are



produced. The plume (and the associated materials) is transported towards the substrate. The quality of deposited films is governed by various deposition parameters, such as substrate temperature, ambient gas pressure, laser power density and repetition rates. These parameters strongly affect the ablation process and the thin film growth mode. Besides, the content of oxygen vacancies in the films can be controlled through the deposition environment or by post-deposition *in situ* annealing process. The condensation and diffusion processes of transported materials are mainly governed by the substrate temperature. With a high substrate temperature ($> 600^{\circ}\text{C}$) and lattice-matching substrates, epitaxial growth of films can be achieved by PLD.

3.2.1 Unique characteristics of pulsed laser deposition

Compared with other deposition techniques, the unique characteristics associated with the PLD technique are listed as follows:

- Good stoichiometric matching between the target material and the as-grown films.
- Epitaxial films can be easily obtained under high substrate temperatures.
- Precise control of film thickness can be achieved.
- Background pressure can be varied from mTorr to 10^{-8} Torr range. Moreover, an oxygen-abundant environment can be introduced to suppress the formation of oxygen vacancies during the deposition of oxide films.
- Under certain deposition conditions, nanoparticles and nanowire can be prepared.
- Deposition rates can be adjusted by controlling the laser pulse frequency.
- Due to the high kinetic energy of the species, re-deposition and defects are often found in the as-grown films.
- Due to the use of high laser energy, micron-sized particulates are often found on the films.

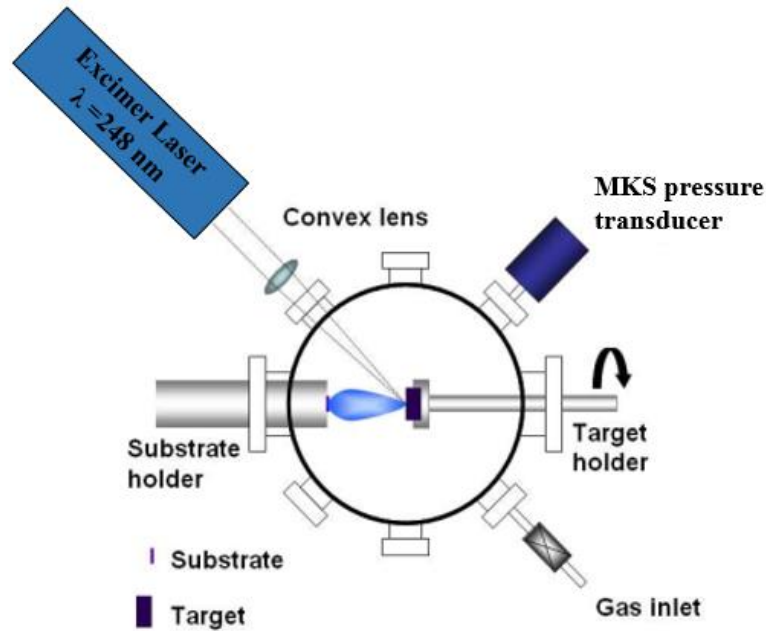


Figure 3. 2 Schematics diagram of PLD system used in this project.

3.2.2 Thin film growth modes

The surface energy between adatoms, and the interaction energy between adatoms and the substrate are the key factors that determine the growth of epitaxial films on lattice-matching substrates. On the sub-monolayer level, adatoms arrive and move to favorite sites on the substrate by surface diffusion. As the deposition goes on, the adatoms prefer to coalesce and form nuclei. The nuclei then tend to form grains and islands, which gradually merge together and form a continuous film.

These nucleation and growth processes can be classified into three modes (Figure 3. 3): Volmer-Weber (island) growth, Frank-van der Merwe (layer-by-layer) growth and Stranski-Krastinov growth. In the Volmer-Weber growth mode, deposited materials tend to form clusters and finally become three-dimensional aggregates on the substrate. The interatomic interactions between adatoms are stronger than that between the substrate and the film material. In the layer-by-layer growth mode, the adatoms tend to spread over on the substrate and form a full coverage of monolayer. The interatomic interactions between adatoms and the substrate are stronger than those among the adatoms. Stranski-Krastinov growth mode involves a layer-by layer growth mode at the early stages, and island growth mode tends to happen as the film thickness increases.

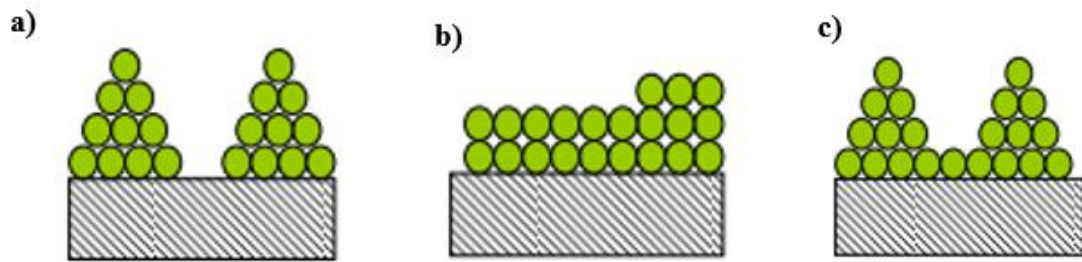


Figure 3.3 Three different thin film growth mode: (a) island growth mode, (b) layer-by-layer growth mode, and (c) Stranski-Krastinov growth mode.

3.2.3 Thin film growth conditions in this project

In this project, a krypton fluoride (KrF) excimer laser (with wavelength 248 nm and pulse duration 25 ns) was used to ablate the desired target materials. The target faced directly towards the substrates, which facilitated the achievement of uniform film thickness. The base pressure of the PLD system can achieve 5×10^{-4} Pa. Up to four PLD targets can be installed and selected during the deposition, and a linear manipulator allowed the change of the target-substrate distance. The substrate temperature was monitored by a K-type thermocouple, which was embedded underneath the substrate holder. The substrate can be heated up to 750°C during the thin film growth. The oxygen pressure of the PLD system was controlled by a MKS mass flow controller and a regulating valve inside the chamber. Prior to deposition, a pre-ablation process was necessary to remove any unwanted materials on the surface of the target. Table 3.1 lists the deposition conditions for PLD of thin films in this project.



Target materials	LSMO	Zn _{0.92} Mn _{0.08} O
Energy	220 mJ	220-300 mJ
Substrate temperature	700 °C	300 °C
Oxygen pressure	150 mTorr	3.8 x10 ⁻⁶ Torr
Repetition rate of excimer laser	1	3
Number of pulses	240	600
In-situ annealing condition	700 °C, 10 Torr (5 minutes)	NA

Table 3. 1 Experimental conditions for PLD of LSMO and Zn_{0.92}Mn_{0.08}O thin films.

3.2.4 Target fabrication

LSMO and Zn_{0.92}Mn_{0.08}O ceramic targets for PLD were prepared by conventional solid-state reactions. The synthesis of ceramic target can be divided into two parts:

- 1) Starting precursors (oxide powders) of correct stoichiometric ratio were mixed in an ethanol medium by a ball-milling process for 10 hours. After that, the mixture was dried in the oven at 120°C and was followed by a calcination process (600°C for Zn_{0.92}Mn_{0.08}O target and 1100°C for LSMO target) for 10 hours. The calcination process allowed the initialization of the chemical reaction in the mixed oxides.
- 2) The calcined powder was grounded and mixed with 5 wt% PVA (polyvinyl alcohol) homogeneously. The PVA solution served as a binder for granulation in the agate mortar. Dense pellets with 25 mm diameters were prepared by an uniaxial pressure of 50 MPa for 30 seconds. Finally, a sintering process (800°C for Zn_{0.92}Mn_{0.08}O target and 1350°C for LSMO target) was employed to increase the density of the ceramic target.



3.3 Device fabrication

This section describes the fabrication process of micron-sized devices, which were used to study the electric-field manipulation of magnetism in $\text{Zn}_{0.92}\text{Mn}_{0.08}\text{O}$ and LSMO. The device fabrication processes, including optical lithography, etching and deposition of contact electrodes, are described as follows.

3.3.1 Fabrication of LSMO field-effect devices

To study the electric-field manipulation of magnetism in LSMO, ferroelectric copolymer of P(VDF-TrFE) was employed as the dielectric to manipulate the change in the carrier concentration in the LSMO channel layer. In this section, the device fabrication process is described.

1. Optical lithography of Hall-bar patterns
 - a. 1.5 μm -thick AZ5214 photoresist was spun on the sample. Desired Hall-bar patterns with channel widths and lengths of 20 and 200 μm were exposed to ultraviolet (UV) radiation with a power density of 24 mW/cm^2 for 15 seconds and developed in AZ300 MIF for 40 seconds.
 - b. Inductively coupled plasma (ICP) etching was employed to provide the physical and chemical etching of the LSMO channel, using a mixture of CH_4 and Ar gases at a ratio of 4:1 for 4 mins. The etching rate was typically 4 nm/min .
 - c. The remaining photoresist was washed away by acetone.
2. Fabrication of contact pads
 - a. 1.5 μm -thick AZ5214 photoresist was spun on the sample. The desired contact pad patterns were exposed to UV radiation with a power density of 24 mW/cm^2 for 15 seconds and developed in AZ300 MIF for 40 seconds.
 - b. Au (50 nm)/Ti (5 nm) contact pads for LSMO channel were deposited by electron-beam (e-beam) evaporation, with a deposition rate of 0.2 $\text{\AA}/\text{s}$.
 - c. A lift-off process was employed to remove any metal films on unwanted locations.
3. P(VDF-TrFE) deposition

- a. P(VDF-TrFE) copolymer (7:3 mole ratio) was dissolved in diethyl carbonate with a mass content of 2.5%, and was spin-coated at 4000 rpm for 30 seconds on the LSMO Hall-bar pattern, resulting in 250 nm of copolymer film.
- b. The as-deposited copolymer films were annealed at 120°C in air for 2 hours, in order to obtain the ferroelectric β phase.
- c. Au (30 nm)/ Al (100 nm) top-contact electrodes ($500 \times 1000 \mu\text{m}$) were deposited by e-beam evaporation with appropriate alignment of shadow masks.

Upon the application of a large voltage that is sufficient to induce the ferroelectric polarization reversal, or through the use of a low-voltage pulsing method, the accumulation and depletion of charge carriers in the LSMO/P(VDF-TrFE) heterostructure were obtained, which is shown in Figure 3. 4.

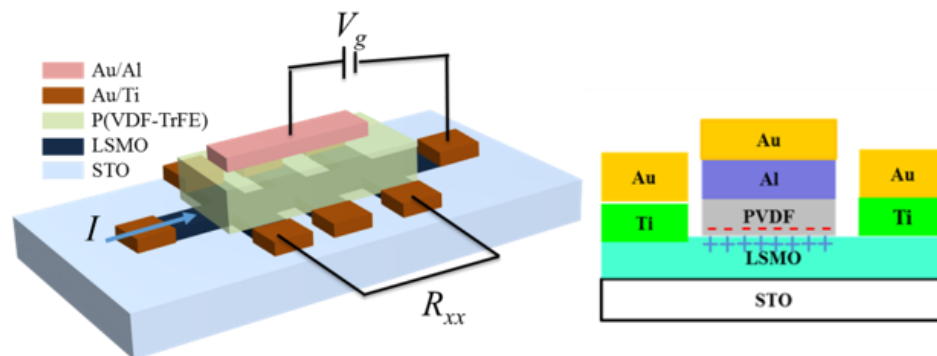


Figure 3. 4 Schematic illustration (left) and cross-sectional view (right) of the device geometry for magnetism modulation in LSMO induced by charge accumulation.

3.3.2 Fabrication of $\text{Zn}_{0.92}\text{Mn}_{0.08}\text{O}$ devices

To reduce the electric-field-induced breakdown of the field-effect devices, low-electric-field manipulation of magnetism in $\text{Zn}_{0.92}\text{Mn}_{0.08}\text{O}$ devices was studied through gating via an IL of [*N,N*-diethyl-*N*-(2-methoxyethyl)-*N*-methylammonium (DEME⁺) and bis(trifluoromethylsulfonyl)-imide (TFSI⁻)]. The device fabrication process is described as follows:

1. Fabrication of Hall-bar patterns

- a. 1.5 μm -thick AZ5214 photoresist was spun on the sample. The desired Hall-bar geometry with channel widths and lengths of 50 and 100 μm were



- exposed to UV radiation with a power density of 24 mW/cm^2 for 15 seconds and developed with AZ300 MIF for 40 seconds.
- b. Wet etching process was employed to remove materials in the area not covered by the photoresist, using diluted HCl as the etchant.
 - c. The remaining photoresist was washed away by acetone.
2. Deposition of metal electrodes and capping layers
- a. $1.5 \text{ }\mu\text{m}$ -thick AZ5214 photoresist was spun on the sample. The desired contact pads were exposed to UV radiation with a power density of 24 mW/cm^2 for 15 seconds and developed with AZ300 MIF for 40 seconds.
 - b. Au (50 nm)/Ti (5 nm) contact electrodes for $\text{Zn}_{0.92}\text{Mn}_{0.08}\text{O}$ and IL were deposited by e-beam evaporation, with a deposition rate of 0.2 \AA/s .
 - c. A lift-off process was employed to remove any metal films at unwanted locations.
3. Preparation of IL
- a. 2 nm-thick SiO_2 was prepared by e-beam evaporation, to prevent any chemical reaction between the IL and $\text{Zn}_{0.92}\text{Mn}_{0.08}\text{O}$ thin film.
 - b. Due to the sensitive chemical nature of IL, it was kept at 80°C to prevent any water contamination.
 - c. The devices were immediately put into the measurement chamber within 2 minutes after the addition of IL on the channel.

With the application of a gate voltage, electric-field manipulation of charge carriers occurred on the surface of $\text{Zn}_{0.92}\text{Mn}_{0.08}\text{O}$ layer, as illustrated in Figure 3. 5.

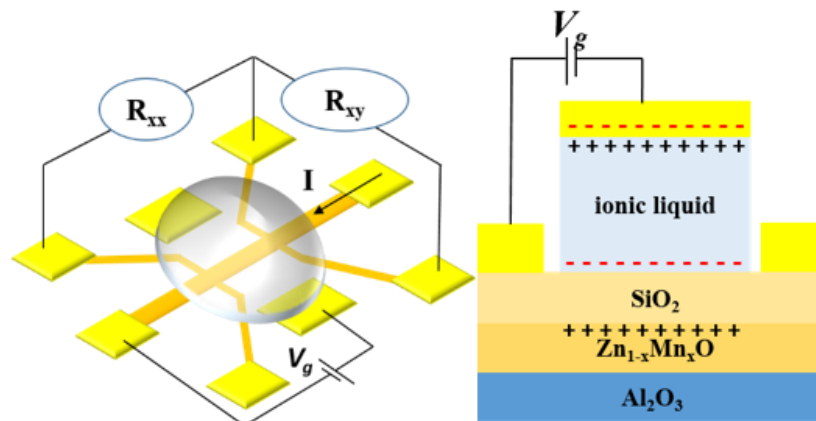




Figure 3. 5 The schematic diagram and side view of electric-field manipulation in magnetism of $Zn_{1-x}Mn_xO$ ($x = 0.08$).

3.4 Thin film characterization techniques

This section presents the experimental techniques used to characterize the oxide thin films and the Hall-bar devices. Structural characterization methods such as AFM, TEM, XPS and XRD are discussed. The magnetic behavior of the oxide thin films were examined by VSM. Finally, Hall-effect measurements and magnetic field-dependent resistance measurements are also mentioned.

3.4.1 X-ray diffraction

X-ray diffraction (XRD) is widely used to reveal the microstructural information of materials such as crystal structure, crystal orientation and phases present in materials. In this project, XRD was performed using a Rigkua Smartlab XRD with Cu K_α radiation with a 2-bounce monochromator.

The working principle of XRD involves an X-ray beam incident on the sample surface. The X-ray beam scattered by crystal planes interfere with each other, and constructive interference occur according to Bragg's law:

$$2d_{hkl} \sin \theta = n\lambda$$

where d_{hkl} is the d -spacing between successive planes and n is an integer.

In the high-angle regime ($2\theta > 10^\circ$), several scan modes were performed to understand the crystal information of films. θ - 2θ scans were used to identify the crystalline phase and crystal orientation of the films. ω -scans (rocking curves) were used to determine the mosaicity of the films, which can be revealed by the full-width at half-maximum (FWHM) of selected diffraction peaks. ϕ -scans were employed to understand in-plane crystallographic relationship between the film and the substrate.

Figure 3. 6 (a) shows the θ - 2θ scan of a 24 nm-thick LSMO film grown on TiO₂-terminated STO (001) substrate. Only (002) peaks of the LSMO film and the STO substrate are obtained. Moreover, Laue oscillations are observed around the LSMO film peak, indicating highly-ordered crystalline film was prepared in the PLD system used in this work. In Figure 3. 6 (b), the FWHM of LSMO (002) and STO (002) diffraction peak are 0.1° and 0.06° respectively, further proving that the LSMO films are of good quality.

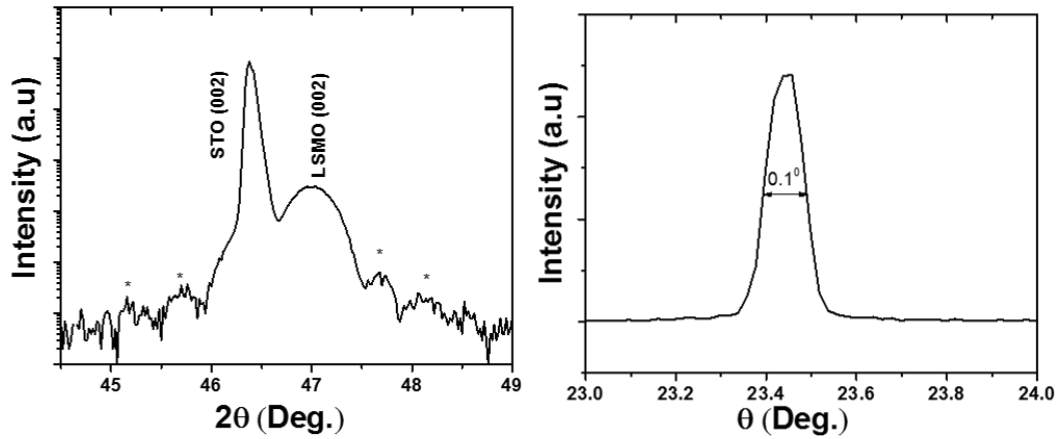


Figure 3. 6 (a) XRD θ - 2θ scan of 24 nm-thick LSMO film on (001) STO substrate. * represents the satellite peaks., (b) XRD ω -scan of (002) LSMO film, showing a FWHM around 0.1° .

In the low-angle regime ($2\theta < 10^\circ$), physical properties of the films such as film thickness, surface roughness and density of films can be explored by X-ray reflectivity (XRR). Figure 3. 7 shows the characteristic features of a typical XRR scan. The initial drop of the intensity at very low 2θ values ($< 1^\circ$) originates from the critical angle, which results from the total external reflectivity of X-ray from the surface of the film. The regularly-spaced oscillations in the reflectivity scan are known as the Kiessig fringes, which are consequences of the interference of X-rays between heterogeneous interfaces formed by different materials (hence different refractive indices). The thickness of films (down to angstrom-level resolution) can be obtained from the 2θ values of successive Kiessig fringes [6, 7]:

$$\sin^2 \theta_{n+1} - \sin^2 \theta_n = \left(\frac{\lambda}{2t_{film}}\right)^2$$

where $(\sin^2 \theta_{n+1} - \sin^2 \theta_n)$ is the measured value from successive peaks in XRR measurement, λ is the wavelength of x-ray and t_{film} is the thickness of films.

The general effect of film roughness is to affect the decay rate of the reflectivity in the XRR measurement. The higher the film roughness, the stronger is the attenuation of the reflectivity with increasing 2θ values.

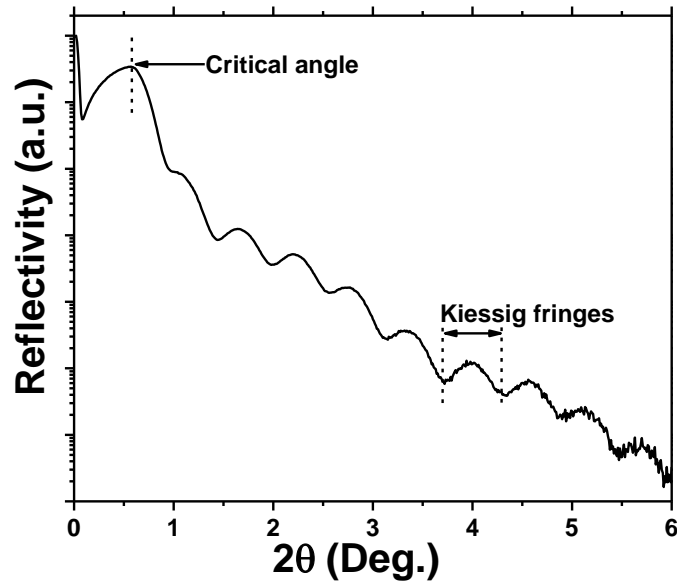


Figure 3. 7 XRR measurement of a 15-nm $\text{La}_{0.8}\text{Sr}_{0.2}\text{MnO}_3$ film deposited on (001) STO substrate by PLD.

3.4.2 Atomic force microscopy

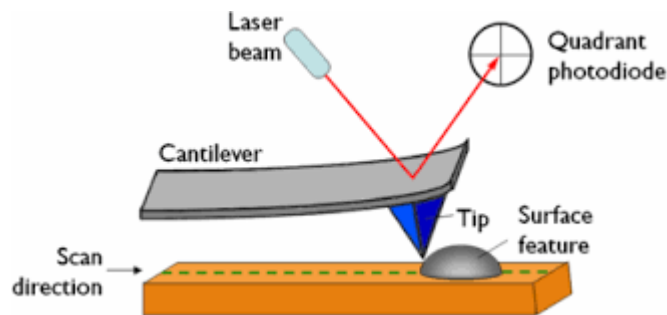


Figure 3. 8 Schematics diagram of atomic force microscopy. Adapted from [8].

Atomic force microscopy (AFM) (Digital Instrument Nanoscope IV) was used to investigate the surface morphology of films with height variations ranging from angstroms to sub-micrometer levels (Figure 3. 8). For the working principle, as the tip approaches to sample's surface, either attractive or repulsive force between sample surfaces and tip would cause the cantilever to deflect towards or away the sample surfaces. The change in oscillation amplitude of the tip can be reflected from the back of the tip to photodiodes. By tracking the movement of the tip, the surface features can be obtained.

3.4.3 X-ray photoelectron spectroscopy

X-ray photoelectron spectroscopy (XPS) is a surface-sensitive spectroscopic technique that is widely employed to investigate the chemical information of samples, such as



elemental composition, empirical formulae, chemical and electronic states of the elements inside the samples. The working principle of XPS (Figure 3. 9) involves the sample being irradiated with a beam of monochromatic X-ray, and the kinetic energy and the number of the ejected electrons are quantitatively measured.

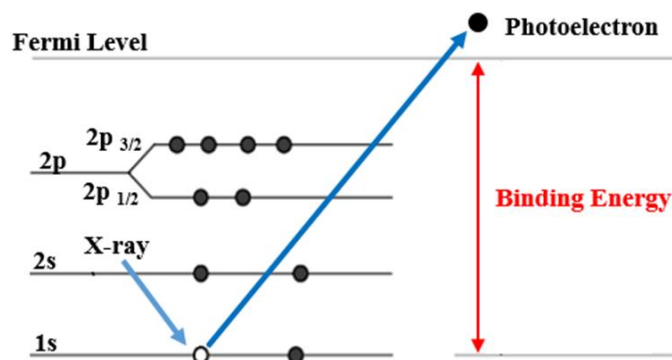


Figure 3. 9 Schematic diagram of X-ray photoelectron effect.

The binding energy of the emitted electrons can be determined by the following equation:

$$E_{binding} = E_{photon} - E_{kinetic}$$

where $E_{binding}$ is the binding energy of electron, E_{photon} is the energy of the X-ray photon and $E_{kinetic}$ is the kinetic energy of electrons measured from the sample.

In this project, the chemical states of the samples were characterized by XPS with a Sengyang SKL-12 electron spectrometer equipped with a VG CLAM 4 MCD electron energy analyzer and twin-anode Mg K_{α} radiation (1253.6 eV) or Al K_{α} radiation (1496.3 eV) X-ray sources. The base pressure of the XPS measurement was about 2×10^{-9} Torr. All binding energies in this work were calibrated with the C 1s peak (284.6 eV).

3.4.4 Transmission electron microscopy

Transmission electron microscopy (TEM) is a high-resolution microscopic technique, as illustrated in Figure 3. 10. It is useful to study the crystal quality in microscopic scales, as well as the epitaxial relationship between the film and the substrate.

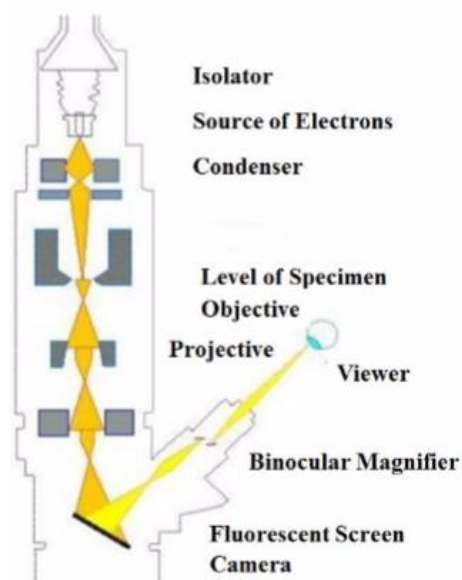


Figure 3. 10 Schematic illustration of transmission electron microscopy. Adapted from[9].

The crystal structure of epitaxial films was examined by cross-sectional high-resolution transmission electron microscopy (HRTEM) with a JEOL 2100F electron microscope. The preparation of cross-sectional specimen involves the mechanical polishing of the sample down to 10 μm or below, followed by an ion milling process which further reduces the specimen thickness to 100 nm or below. In this study, TEM was generally operated at the bright field mode for capturing large-area images, and the HRTEM mode for detailed studies such as defects, interfacial investigations and thickness measurements.

3.4.5 Vibrating sample magnetometer

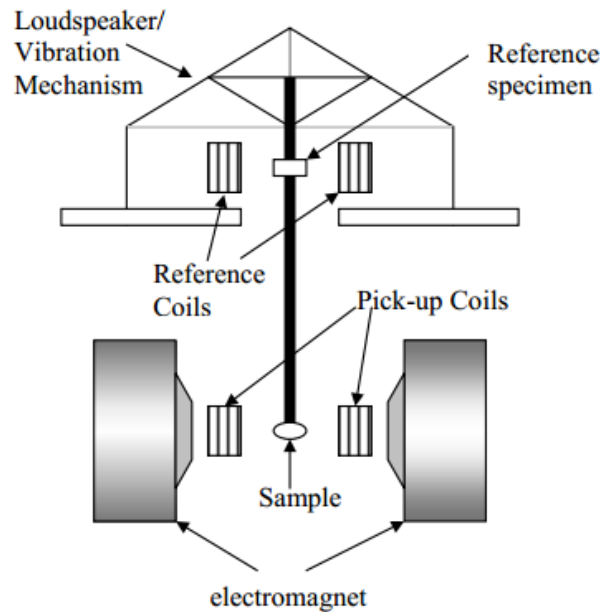


Figure 3. 11 Schematic diagram of VSM system. Adapted from [7].

Vibrating sample magnetometer (VSM) was employed to study the magnetic properties of LSMO and $\text{Zn}_{0.92}\text{Mn}_{0.08}\text{O}$ thin films. This non-destructive technique is a common method to characterize the magnetization signals ranging from 10 emu to 1 μemu . The working principle of VSM (Figure 3. 11) involves the sample being vibrated in an applied static magnetic field. The induced voltage in the pick-up coil is proportional to the magnetic moment of the sample. In this project, the magnetic hysteresis curves (M-H curves) were examined by a Quantum Design physics property measurement system (PPMS) and a Lakeshore 7400 magnetometer. Moreover, diamagnetic contributions from the substrates and sample rods were subtracted, in order to measure the accurate magnetic moments of the samples.

3.4.6 Hall effect measurements

Hall effect is a phenomenon that a transverse force is exerted on the charge carriers if an electric current flows through a conductor, when an applied magnetic field is imposed perpendicularly to the current flow direction.

The film resistivity, sheet carrier density and mobility of thin films were measured in this project by preparing the films into Hall bar geometries. The measurements were carried



out in a closed-loop cryogenic chamber at temperatures between 10 and 300 K and variable magnetic field between $\pm 0.6\text{T}$.

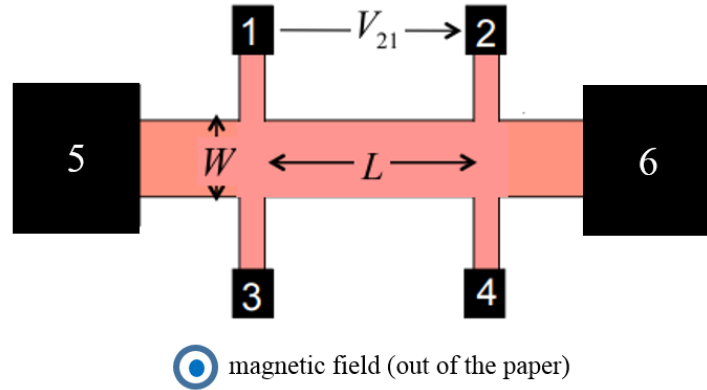


Figure 3. 12 Schematic diagram of a 6-contact Hall-bar pattern.

The resistivity of thin films can be deduced from the longitudinal resistance using the 6-point Hall bar pattern (Figure 3. 12) in the absence of external magnetic field, according to the following relation: $\rho_{xx} = \frac{V_{21}Wt}{I_{56}L}$, where W and t are the width and thickness of the Hall bar, L is the distance between point 2 and 1, I_{56} is the applied current. The carrier concentration (n) of the samples can be deduced from these following equation: $n = \frac{V_{24}t}{B I_{56}}$, where B is the applied (out-of-plane) magnetic field and V_{24} is the potential difference between points 2 and 4. Sheet carrier densities of samples can be deduced from the Hall voltage measured between points 2 and 4 by: $n_s = \frac{IB}{qV_{24}}$. The negative and positive signs of carrier concentration refer to the electron and hole conduction, respectively. Finally, the mobility of samples can be calculated from $\mu = \frac{R_H}{\rho_{xx}}$.

The use of Hall-bar patterns with micrometer sizes suppresses the possibility of short-circuits between top gate and sample channel, as well as restrict the current direction under Hall-bar geometries.

3.4.7 Anomalous hall effect

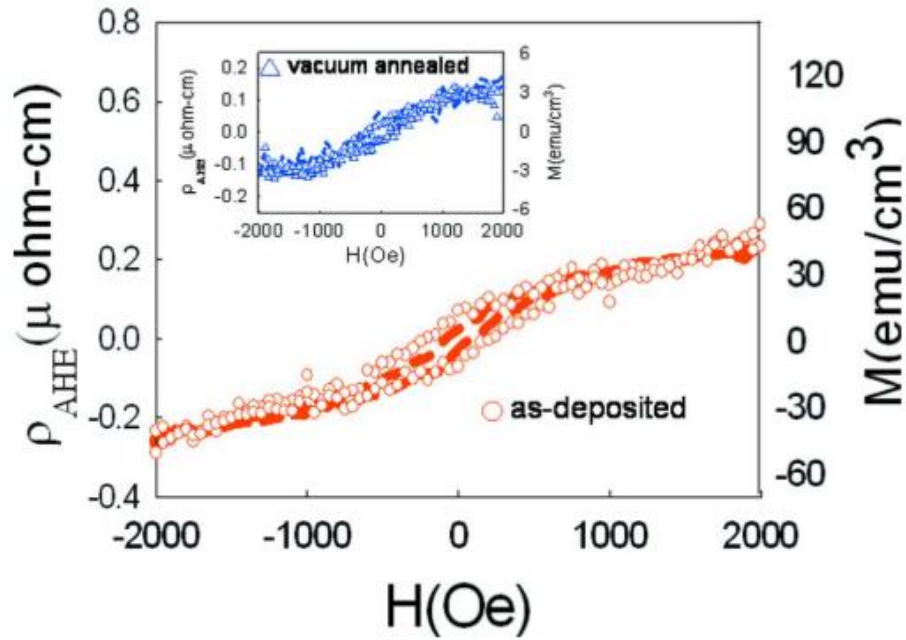


Figure 3. 13 AHE of as-deposited Co-doped ZnO (red circles), overlapped with the corresponding $M-H$ loop (dashed line). The inset shows the same measurements for a vacuum-annealed sample. [10].

The Hall effect in ferromagnetic materials (under an out-of-plane applied field H_z) have contributions from two different sources; the ordinary hall effect (OHE) increases with H_z due to the Lorentz force acting on the charge carriers, while the contribution from anomalous hall effect (AHE) is due to the magnetization of the sample. The AHE increases steeply in weak H_z , and becomes saturated as H_z further increases. Study from Pugh *et al.* established the equation which is described as [11],

$$\rho_{xy} = R_0 H_z + R_S M_z$$

where R_0 is a constant which may be nearly independent of material and R_S is a constant which can be positive and negative depending on the material [11]. The first and second terms are the OHE and AHE, the latter being the consequence of the spontaneous magnetization in the ferromagnet. As shown in Figure 3. 13, the coercivity value of $\rho_{AHE} - H$ curves in Co-doped ZnO is comparable with those in $M - H$ curves, indicating that AHE is an alternative method to characterize the weak ferromagnetic signals that cannot be easily measured by the conventional magnetometers. In this work, the AHE was employed to characterize the strength of ferromagnetism in $Zn_{0.92}Mn_{0.08}O$, as the charge carrier of $Zn_{0.92}Mn_{0.08}O$ is accumulated or depleted through an IL gating process.



3.4.8 Physical property measurement system

Physical property measurement system (PPMS) was employed to measure the electrical and magnetic properties of $\text{Zn}_{0.92}\text{Mn}_{0.08}\text{O}$ thin films. The PPMS provides an environment for variable temperature (2 to 400 K) and variable magnetic field (± 9 T) measurements. Magneto-transport properties of $\text{Zn}_{0.92}\text{Mn}_{0.08}\text{O}$ devices were measured by four-point electrical measurements, in order to eliminate the contribution from contact resistances. Au (50 nm)/ Ti (5 nm) electrodes were used to form ohmic contacts on the $\text{Zn}_{0.92}\text{Mn}_{0.08}\text{O}$ and LSMO films. Electrical contacts between thin films and measurement holder were connected with Al bonding wire.

3.4.9 Magnetoresistance

Magnetoresistance (MR) measurements were performed in a closed-cycle cryogenic chamber with temperature ranging from 20 to 400 K in the vicinity of a magnetic field (± 0.6 T). Keithley 6221 was employed as an AC current source ranging from 100 to 1 μA into sample and the voltage was measured by a Keithley 2182A nanovoltmeter. The MR ratio is defined by the following equation:

$$\frac{R(H_{\text{Field}}) - R(H_0)}{R(H_{\text{Field}})} \times 100\%$$

As the applied magnetic field is parallel with the current direction of samples, anisotropic magnetoresistance (AMR) of the samples can be measured. AMR can be useful in probing the magnetic signals which are low and difficult to be measured by conventional magnetometers [12-14].

3.5 Conclusion

The experimental details for the deposition of high-quality LSMO and $\text{Zn}_{0.92}\text{Mn}_{0.08}\text{O}$ films are presented. Detailed fabrication steps of Hall bars, field-effect devices are introduced. Finally, different characterization methods were employed to study structural, electronic and magnetic properties of these electric-field manipulation of magnetism in the LSMO and $\text{Zn}_{0.92}\text{Mn}_{0.08}\text{O}$ devices are introduced.



References for Chapter 3

- [1] M. Salluzzo, S. Gariglio, D. Stornaiuolo, V. Sessi, S. Rusponi, C. Piamonteze, G.M. De Luca, M. Minola, D. Marré, A. Gadaleta, H. Brune, F. Nolting, N.B. Brookes, G. Ghiringhelli, Origin of Interface Magnetism in $\text{BiMnO}_3/\text{SrTiO}_3$ and $\text{LaAlO}_3/\text{SrTiO}_3$ Heterostructures, *Physical Review Letters*, 111 (2013) 087204.
- [2] T. Ohnishi, K. Shibuya, M. Lippmaa, D. Kobayashi, H. Kumigashira, M. Oshima, H. Koinuma, Preparation of thermally stable TiO_2 -terminated $\text{SrTiO}_3(100)$ substrate surfaces, *Applied Physics Letters*, 85 (2004) 272-274.
- [3] M. Kawasaki, K. Takahashi, T. Maeda, R. Tsuchiya, M. Shinohara, O. Ishiyama, T. Yonezawa, M. Yoshimoto, H. Koinuma, Atomic Control of the SrTiO_3 Crystal Surface, *Science*, 266 (1994) 1540-1542.
- [4] J.G. Connell, B.J. Isaac, G.B. Ekanayake, D.R. Strachan, S.S.A. Seo, Preparation of atomically flat SrTiO_3 surfaces using a deionized-water leaching and thermal annealing procedure, *Applied Physics Letters*, 101 (2012) 251607.
- [5] M. Kareev, S. Prosandeev, J. Liu, C. Gan, A. Kareev, J.W. Freeland, M. Xiao, J. Chakhalian, Atomic control and characterization of surface defect states of TiO_2 terminated SrTiO_3 single crystals, *Applied Physics Letters*, 93 (2008) 061909.
- [6] B. Cull, Y. Shi, S. Kumar, R. Shih, J. Mann, X-ray reflectivity study of interface roughness, structure, and morphology of alignment layers and thin liquid crystal films, *Physical Review E*, 51 (1995) 526-535.
- [7] C.W. Leung, *Metallic Magnetic Heterostructures*, Department of Materials Science, University of Cambridge, United Kingdom, 2002.
- [8] J.B. Daniel, A.B. William, C. Neal, K. Jennifer, H.T. Neil, Single-molecule studies of DNA transcription using atomic force microscopy, *Physical Biology*, 9 (2012) 021001.
- [9] H.M. A., *Principles and Techniques of Scanning Electron Microscopy*, Van Nostrand Reinhold Co. 1974.
- [10] H.S. Hsu, C.P. Lin, H. Chou, J.C.A. Huang, Room temperature anomalous Hall effect in Co doped ZnO thin films in the semiconductor regime, *Applied Physics Letters*, 93 (2008) 142507.
- [11] E.M. Pugh, Hall Effect and the Magnetic Properties of Some Ferromagnetic Materials, *Physical Review*, 36 (1930) 1503-1511.
- [12] N. García, M. Muñoz, Y.W. Zhao, Magnetoresistance in excess of 200% in Ballistic Ni Nanocontacts at Room Temperature and 100 Oe, *Physical Review Letters*, 82 (1999) 2923-2926.
- [13] J.A. Katine, A. Palanisami, R.A. Buhrman, Width dependence of giant magnetoresistance in Cu/Co multilayer nanowires, *Applied Physics Letters*, 74 (1999) 1883-1885.
- [14] R.D. Slater, J.A. Caballero, R. Loloee, W.P.P. Jr., Perpendicular-current exchange-biased spin valve structures with micron-size superconducting top contacts, *Journal of Applied Physics*, 90 (2001) 5242-5246.



Chapter 4 Electric-field manipulation of magnetism in the multiferroic heterostructure of $\text{La}_{0.66}\text{Sr}_{0.33}\text{MnO}_3/\text{P}(\text{VDF-TrFE})$

4.1 Introduction

Recent progress in electric-field control of magnetism has already demonstrated the capability of tuning magnetic moments [1-3], metal-to-insulator transition temperatures [1, 3-6], magnetic anisotropy [1, 3, 7] and exchange-bias effect in magnetic heterostructures [1, 8-10]. Among different methods, electric-field control of magnetoelectric multiferroics has attracted much attention, due to the potential application for next-generation memories devices by controlling the magnetic states through electric field [11].

Intensive studies have been conducted on the strain-mediated magnetoelectric multiferroics [2, 12]. External electric field causes a change of ferroelectric lattice parameter, and the strain effect is transferred to the ferromagnet layer through the converse piezoelectric effect. The strain induces changes in the magnetic properties such as magnetization and T_c of $(\text{La}_{1-x}\text{Sr}_x)\text{MnO}_3$ grown on the PMN-PT substrates [12]. Very often, a few hundred volts is required for achieving such changes, which is too large for integration into the existing semiconductor devices [2, 12, 13].

The second method of electric-field manipulation of magnetism in ferroelectric/ferromagnetic bilayers relies on the interfacial charge-mediated magnetoelectric coupling [14-17]. The change of transport and magnetic properties in ferromagnet is mainly governed by the ferroelectric polarization. For LSMO, the field-effect geometry is expected to modulate the magnetism mainly due to charge-mediated ME coupling, which occurs within a few nm of the LSMO at the ferroelectric/ferromagnetic interface [13]. To achieve low-switching voltage in electric-field-induced magnetic devices, a thin ferroelectric layer with epitaxial relationship between the ferroelectric and the ferromagnet is required, and high deposition temperature is necessary to obtain highly-crystalline ferroelectrics such as BaTiO_3 and $(\text{Pb,Zr})\text{TiO}_3$ [16, 18, 19].



Apart from ferroelectric oxides, ferroelectric polymers such as crystalline copolymer of P(VDF-TrFE) have been used as the ferroelectric layer in electric-field-controlled magnetic devices. For P(VDF-TrFE), an annealing temperature of 120-140°C is required for crystallization into the ferroelectric β phase [20]. In particular, such a ferroelectric control of magnetism has been widely investigated in manganite systems such as LSMO, due to the 100 %-spin polarization and T_c around 350 K that are promising for future spintronics devices [15, 21-26]. In these system, tunable ferromagnetism using ferroelectric gate mainly relies on the manipulation of the double-exchange coupling between Mn^{3+} and Mn^{4+} through the O $2p$ orbital [27, 28]. Upon the depletion and accumulation of charge carrier in the ferromagnet, a control in the strength of magnetism was achieved.

Up to now, most of works concerning the field-effect control of magnetism are based on polarization reversal of FE oxides [9, 19], and there was little work on modulating manganite channels use FE copolymer as the gate dielectric. In this Chapter, the electric-field manipulation of transport and magnetic properties in the multiferroic bilayer heterostructure, with P(VDF-TrFE) as ferroelectric layer and LSMO as ferromagnetic layer, is reported. A 15% change in LSMO channel resistance at 300 K was observed upon the ferroelectric reversal of P(VDF-TrFE), with insignificant T_c change in LSMO channel. The experimental results indicated that electric-field effect provided from the ferroelectric reversal of P(VDF-TrFE) failed to penetrate into the LSMO channel, leading to an insignificant change of the magnetic properties in the LSMO devices.

3.2 Experimental details

Epitaxial LSMO films with a thickness of 7.5 nm were prepared on single-crystal STO (001) substrates by PLD. Before the deposition, the substrates were treated with buffered hydrofluoric acid (HF) or deionized (DI) water, followed by a thermal annealing process at 1100°C for 2 hours; as mentioned in Chapter 2, such steps would lead to the formation of TiO_2 -terminated STO surfaces with atomic steps of height 0.39 nm. The LSMO films were then deposited at 700°C with an oxygen pressure of 150 mTorr. After deposition, the films were annealed *in-situ* at an oxygen pressure of 10 Torr for 5 minutes, in order to minimize the oxygen vacancies. The LSMO films were then cooled down to 300 K with a ramp rate of 10 K/min. Film thickness was controlled by the number of laser pulses



used during the deposition (based on a calibrated rate obtained from a thick LSMO sample) and was further evaluated by XRR measurements.

$\text{P}(\text{VDF-TrFE})/\text{LSMO}$ heterostructures were prepared as follows. The LSMO films were patterned into Hall bars with 200 μm channel length and 20 μm channel width by standard photolithography and reactive ion etching processes. Electron beam evaporation was employed to deposit Au (80 nm)/Ti (15 nm) as contact electrodes, with a base pressure of 2.2×10^{-6} Torr and no substrate heating. After that, $\text{P}(\text{VDF-TrFE})$ with 7:3 mole ratio of VDF/TrFE copolymers were dissolved in diethyl carbonate ($\text{C}_5\text{H}_{10}\text{O}_3$, DEC) at a concentration of 2.5% weight content. 250 nm-thick $\text{P}(\text{VDF-TrFE})$ films were prepared on the patterned LSMO by spin-coating techniques at 4000 rpm for 30 seconds and subsequently annealed at 120°C for 2 hours, allowing them to crystallize into the ferroelectric β phase. Finally, top gate electrodes of Au (15 nm)/Al (100 nm) were deposited by electron beam evaporation via appropriate shadow mask alignment with the bottom LSMO Hall-bar pattern.

Figure 4. 1 shows the schematic diagram of the device structure used in this study. To probe the magnetic properties of the LSMO channel, a Keithley 2400 sourcemeter was employed to provide the V_g for switching the polarization direction of $\text{P}(\text{VDF-TrFE})$. The LSMO R_{xx} was measured along the longitudinal direction of the Hall-bar pattern via four-point measurements, in order to eliminate the contributions from contact resistances.

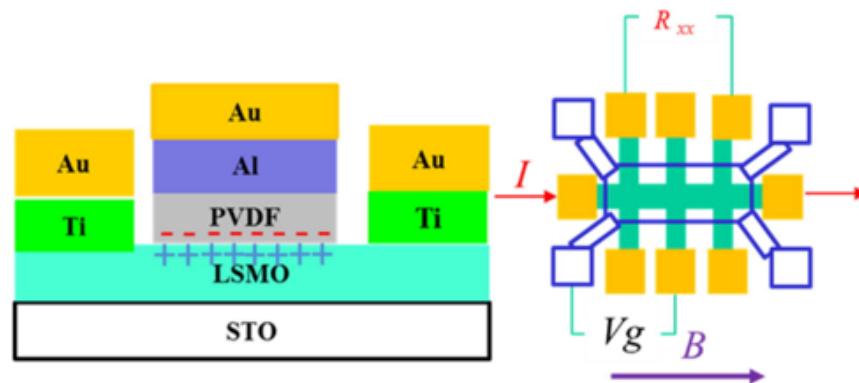


Figure 4. 1 Left: Schematic diagram of device structure used for electric-field manipulation of magnetism in the $\text{P}(\text{VDF-TrFE})/\text{LSMO}$ with accumulated hole carriers in the LSMO channel due to ferroelectric polarization. Right: Planar view of Hall-bar pattern used in this study.



4.1 Results and discussions

4.1.1 Structural characterization

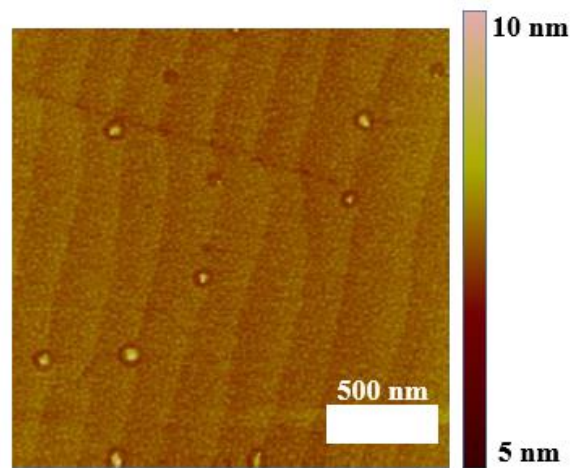


Figure 4. 2 AFM image of 7.5 nm-thick LSMO film grown on STO (001) substrate.

Prior to characterizing the heterostructure, AFM measurement was employed to study the surface morphology of LSMO films grown on STO (001) substrates. As shown in Figure 4. 2, the LSMO film exhibits flat terraces and steps with a height of 0.4 nm, corresponding to one unit-cell of LSMO lattice along the (001) direction [29].

Figure 4. 3 (a) shows the XRD pattern of a 24 nm-thick LSMO films. Apart from the diffraction peaks of LSMO (002) and STO (002) as observed in the $\theta - 2\theta$ scan, the Laue fringes alongside the LSMO (002) diffraction peaks indicate the high crystallinity and atomic flatness of the LSMO films. Moreover, rocking curve (Figure 4. 3(b)) acquired on LSMO (002) diffraction peak have a FWHM about 0.1° , further implying the well-ordering of the LSMO lattice. However, the LSMO (002) diffraction peak in the P(VDF-TrFE)/LSMO heterostructure becomes insignificant due to the reduced film thickness, and is shadowed by (002) STO substrate peak [29, 30]. At the lower-angle regime (Figure 4. 3(c)), a diffraction peak is observed at 19.7° , corresponding to the P(VDF-TrFE) β phase (110) and (200) diffraction peak [30].

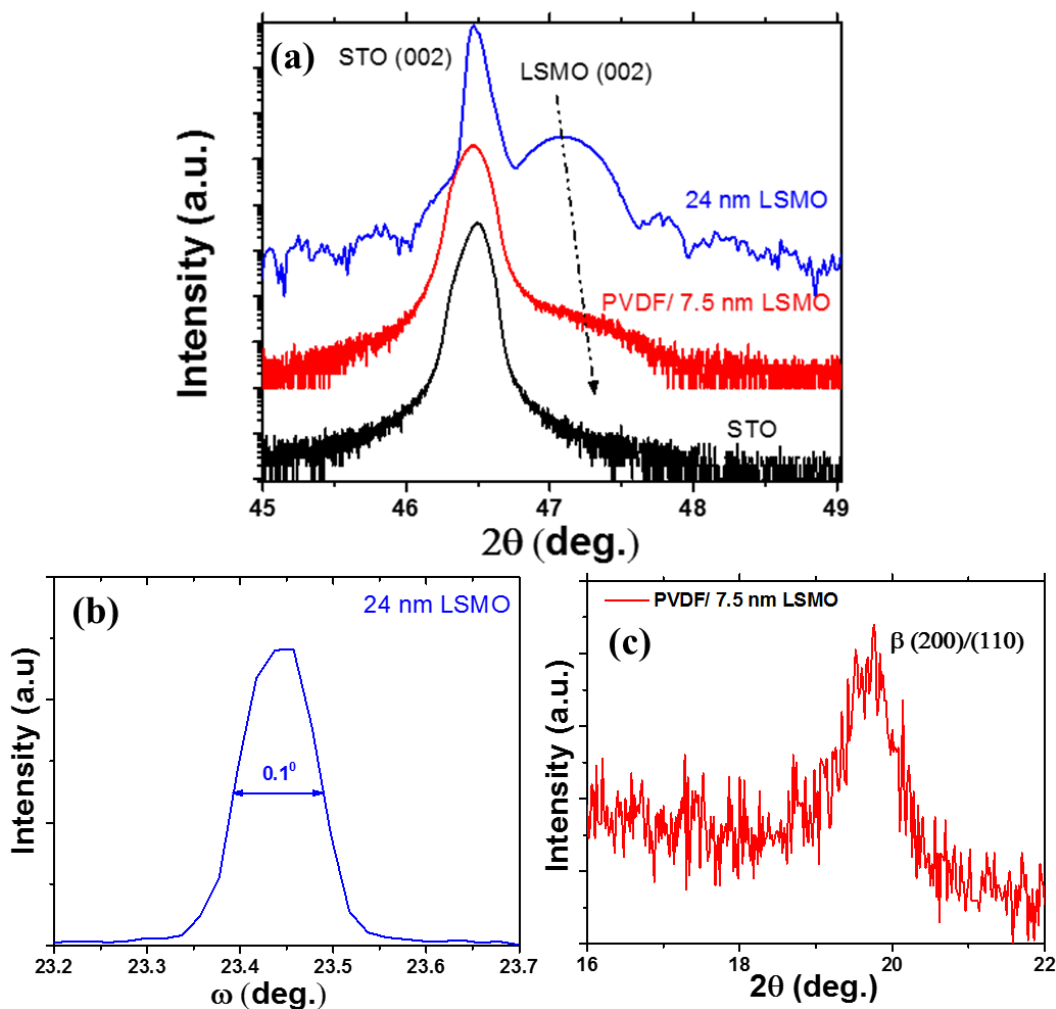


Figure 4. 3 XRD patterns. (a) θ - 2θ scans of bare STO substrate (black color), 24 nm-thick LSMO film (blue color) and P(VDF-TrFE)/LSMO heterostructure (red color). (b) rocking curve acquired from LSMO (002) diffraction peak. (c) θ - 2θ scan of P(VDF-TrFE)/LSMO heterostructure between 2θ values of 16° to 22° , indicating the β phase P(VDF-TrFE) (200)/(110) peak.

PFM was performed to examine the ferroelectric properties of P(VDF-TrFE)/LSMO heterostructures. A Pt-coated AFM tip and the LSMO bottom electrode were set as the positive and negative terminals respectively. Figure 4. 4 (a) show the out-of-plane (OP) piezoelectric response of a 250 nm-thick P(VDF-TrFE) film grown on LSMO sample. The OP PFM phase angle shows a typical ferroelectric hysteresis loop, which corresponds to the domain switching-induced upward and downward polarizations. Based on the hysteresis loop, it was concluded that voltages above 35 V was sufficient to fully switch the polarization directions of the ferroelectric copolymer.



Low-voltage ferroelectric switching process was also examined in the work. Figure 4. 4 (b) shows the topography of the heterostructure undergoing different poling conditions respectively. Without a poling process (outer region), the scan exhibits noisy PFM signals, implying an arbitrary dipole arrangement. After poling with -10 V (downward polarization) and +10 V (upward polarization) tip voltage in the intermediate and inner square region (Figure 4. 4 (b)), sharp piezoelectric contrasts can be observed, implying a voltage of 10 V is enough to partially switch the ferroelectric domain in the P(VDF-TrFE). Figure 4. 4 (c) shows the AFM topography of the P(VDF-TrFE) surface, which shows no surface deformation during the film poling process, and the film surfaces exhibited no atomic terraces of the LSMO after the deposition of P(VDF-TrFE).

4.1.2 Transport and magnetic characterization

The temperature dependence of LSMO channel resistance (R-T) was employed to study its magnetic changes upon the electric-field induced polarization reversal in P(VDF-TrFE), and the results are shown in Figure 4. 5. Voltage pulses of ± 35 V were applied to the top gate electrode, resulting in a 15 % resistance change in R_{xx} at 300 K and less than 1% at 20 K. As the temperature was ramped down from 290 K, a larger screening depth is expected in the LSMO interfaces since the LSMO became more insulating. However, once the temperature is ramped down across the metal-to-insulator transition temperature of the LSMO, it starts to be like a metallic material (with hole carrier concentration $\sim 10^{21} \text{ cm}^{-3}$), resulting in a decrease in the screening depth and leading to a decrease in R_{xx} in the low temperature regime [16].

Insignificant peak value (which essentially correspond to its T_C) shift in the R-T measurements is observed upon the change of polarization direction (Figure. 4. 5), implying that the change of carrier concentration within the LSMO channel is not significant. Upon the application of a +35 V (-35 V) through the top gate electrode, an upward (downward) polarization is induced in the copolymer ferroelectric layer. Hole-doped LSMO carriers are depleted from (accumulated towards) the P(VDF-TrFE)/LSMO interface. On the other hand, this switching process will be irreversible if electric field applied is above the dielectric breakdown strength (400 MV/m) of P(VDF-TrFE) [31]. Several reports suggest that the electric field provided from ferroelectric oxide of BTO only pass through two to three u.c. of LSMO lattice [16]. In the present study, the

spontaneous polarization coefficient of $\text{P}(\text{VDF}-\text{TrFE})$ ($10 \mu\text{C}/\text{cm}^2$) is four times less than BTO ($48 \mu\text{C}/\text{cm}^2$). Low tunability in magnetism is therefore expected.

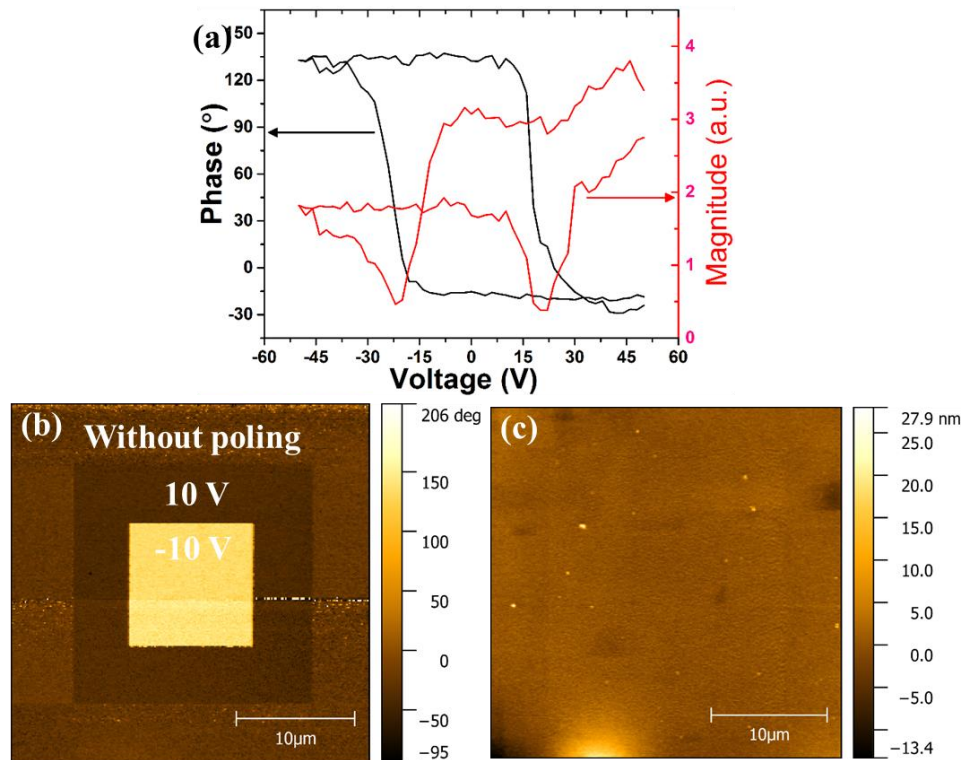


Figure 4.4 (a) Hysteresis loop of the OP PFM phase and magnitude signals obtained from $\text{P}(\text{VDF}-\text{TrFE})/\text{LSMO}$ heterostructure, (b) PFM phase images of inner and intermediate square domains, pre-polarized with -10 V and $+10 \text{ V}$ respectively. (d) AFM image of $\text{P}(\text{VDF}-\text{TrFE})$ acquiring during the poling process.

Considering the homogenous channel in the current case, the carrier concentration in the LSMO channel is uniformly equivalent to 10^{21} cm^{-3} . Electric-field effect from ferroelectric reversal of $\text{P}(\text{VDF}-\text{TrFE})$ is confined to 1 nm at the LSMO/ $\text{P}(\text{VDF}-\text{TrFE})$ interface in LSMO channel, and does not extend into the whole layer. Since the thickness of whole LSMO is 7.5 nm , this implies that the bulk of the film is unaffected and hence the change in T_C is not obvious. At the same time, the overall R_{xx} depends on the proportion of LSMO in the channel layer that is affected by the gating. At high temperatures ($T > T_C$), electric-field effect due to ferroelectric reversal has a strong impact on paramagnetic (insulating) LSMO compared with LSMO in the ferromagnetic metallic state. The change in R_{xx} is expected to be stronger than at low temperatures. At low temperatures ($T < T_C$), the positive V_g transforms the gated LSMO into the insulating state and further suppresses the ferromagnetic metallic state, and results in the increase in the



overall R_{xx} at low temperature. Therefore, large change in R_{xx} and insignificant changes in T_C happens in our system.

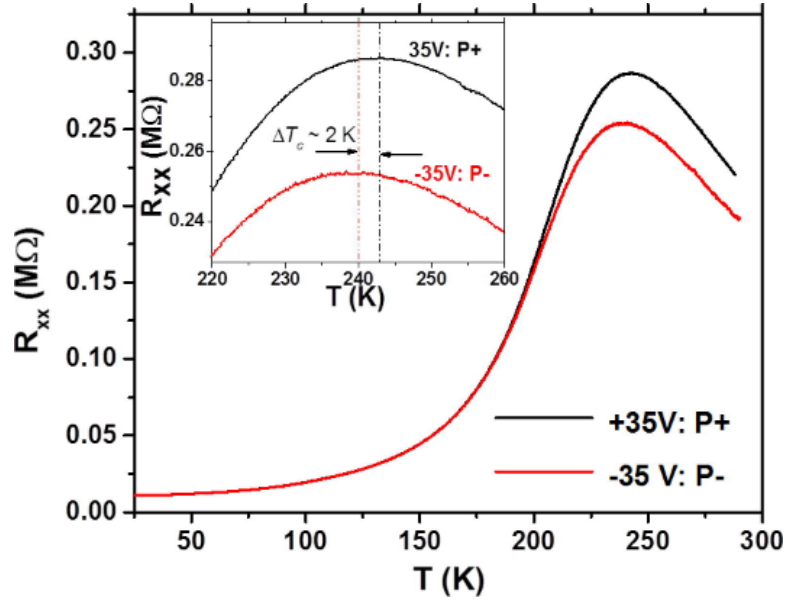


Figure 4. 5 R - T measurement for 7.5 nm-thick LSMO film upon upward and downward polarization from P(VDF-TrFE), where P+ and P- in the legend represent upward and downward polarization direction in P(VDF-TrFE). The inset shows the magnified view of the measurement around the peak of the curves.

To prove that short screening depth of ferroelectric polarization is the main reason of insignificant T_C in the LSMO channel, one should understand the relationship between T_C and hole carrier concentration of LSMO can be approximated as [15],

$$\Delta T_c \propto \frac{\Delta n}{n} \quad (4.1)$$

where Δn can be expressed in the following relationship,

$$\Delta n \propto \frac{P_r}{d_{LSMO}} \quad (4.2)$$

In (4.2), P_r is the remanent polarization of the ferroelectrics and d_{LSMO} is the thickness of LSMO. Based the experimental results by Cui *et al.*, the T_C shift in BTO/LSMO heterostructure is only 5 K upon the ferroelectric reversal in BTO [32], when the thickness of LSMO layer is 20 u.c. (~7.8 nm). Combining equation (4.2) and the experimental results by Cui *et al.*, the expected T_C change due to ferroelectric reversal of P(VDF-TrFE)



should be around 1 K, which can hardly be observed given the broad R-T peak in Fig. 4.5.

4.1.3 Conclusion

In this Chapter, I reported electric-field manipulation of transport and magnetic properties of P(VDF-TrFE) as ferroelectric layer, and LSMO as ferromagnetic layer. Upon the switching polarization direction of P(VDF-TrFE), the screening effect providing from ferroelectrics exhibited 15% change in LSMO resistance at 300K, but less than 1% at 20 K. Moreover, insignificant change of T_C was observed in the R - T measurement.



References for Chapter 4

- [1] S. Fusil, V. Garcia, A. Barthélémy, M. Bibes, *Magnetoelectric Devices for Spintronics*, *Annual Review of Materials Research*, 44 (2014) 91-116.
- [2] W.P. Zhou, Q. Li, Y.Q. Xiong, Q.M. Zhang, D.H. Wang, Q.Q. Cao, L.Y. Lv, Y.W. Du, Electric field manipulation of magnetic and transport properties in $\text{SrRuO}_3/\text{Pb}(\text{Mg}_{1/3}\text{Nb}_{2/3})\text{O}_3\text{-PbTiO}_3$ heterostructure, *Scientific Reports*, 4 (2014) 6991.
- [3] H. Ohno, D. Chiba, F. Matsukura, T. Omiya, E. Abe, T. Dietl, Y. Ohno, K. Ohtani, Electric-field control of ferromagnetism, *Nature*, 408 (2000) 944-946.
- [4] B. Cui, C. Song, G. Wang, Y. Yan, J. Peng, J. Miao, H. Mao, F. Li, C. Chen, F. Zeng, F. Pan, Reversible Ferromagnetic Phase Transition in Electrode-Gated Manganites, *Advanced Functional Materials*, 24 (2014) 7233-7240.
- [5] T. Wu, S.B. Ogale, J.E. Garrison, B. Nagaraj, A. Biswas, Z. Chen, R.L. Greene, R. Ramesh, T. Venkatesan, A.J. Millis, Electroresistance and Electronic Phase Separation in Mixed-Valent Manganites, *Physical Review Letters*, 86 (2001) 5998-6001.
- [6] A.S. Dhoot, C. Israel, X. Moya, N.D. Mathur, R.H. Friend, Large Electric Field Effect in Electrolyte-Gated Manganites, *Physical Review Letters*, 102 (2009) 136402.
- [7] Maruyama T, Shiota Y, Nozaki T, Ohta K, Toda N, Mizuguchi M, A.A. Tulapurkar, Shinjo T, Shiraishi M, Mizukami S, Ando Y, Suzuki Y, Large voltage-induced magnetic anisotropy change in a few atomic layers of iron, *Nat Nano*, 4 (2009) 158-161.
- [8] V. Laukhin, V. Skumryev, X. Martí, D. Hrabovsky, F. Sánchez, M.V. García-Cuenca, C. Ferrater, M. Varela, U. Lüders, J.F. Bobo, J. Fontcuberta, Electric-Field Control of Exchange Bias in Multiferroic Epitaxial Heterostructures, *Physical Review Letters*, 97 (2006) 227201.
- [9] S.M. Wu, S.A. Cybart, D. Yi, J.M. Parker, R. Ramesh, R.C. Dynes, Full Electric Control of Exchange Bias, *Physical Review Letters*, 110 (2013) 067202.
- [10] S.M. Wu, S.A. Cybart, P. Yu, M.D. Rossell, J.X. Zhang, R. Ramesh, R.C. Dynes, Reversible electric control of exchange bias in a multiferroic field-effect device, *Nat. Mater.*, 9 (2010) 756-761.
- [11] V. Garcia, M. Bibes, A. Barthélémy, Artificial multiferroic heterostructures for an electric control of magnetic properties, *Comptes Rendus Physique*, 16 (2015) 168-181.
- [12] C. Thiele, K. Dörr, O. Bilani, J. Rödel, L. Schultz, Influence of strain on the magnetization and magnetoelectric effect in $\text{La}_{0.7}\text{A}_{0.3}\text{MnO}_3/\text{PMN-PT}(001)$ (A=Sr,Ca), *Physical Review B*, 75 (2007) 054408.
- [13] S. Zhang, Q. Chen, Y. Liu, A. Chen, L. Yang, P. Li, Z.S. Ming, Y. Yu, W. Sun, X. Zhang, Y. Zhao, Y. Sun, Y. Zhao, Strain-Mediated Coexistence of Volatile and Nonvolatile Converse Magnetoelectric Effects in $\text{Fe}/\text{Pb}(\text{Mg}_{1/3}\text{Nb}_{2/3})_{0.7}\text{Ti}_{0.3}\text{O}_3$ Heterostructure, *ACS Applied Materials & Interfaces*, 9 (2017) 20637-20647.
- [14] M. Liu, N.X. Sun, Voltage control of magnetism in multiferroic heterostructures, *Philos. Trans. Royal Soc. A*, 372 (2014).
- [15] T. Kanki, Y.-G. Park, H. Tanaka, T. Kawai, Electrical-field control of metal-insulator transition at room temperature in $\text{Pb}(\text{Zr}_{0.2}\text{Ti}_{0.8})\text{O}_3/\text{La}_{1-x}\text{Ba}_x\text{MnO}_3$ field-effect transistor, *Applied Physics Letters*, 83 (2003) 4860-4862.
- [16] H. Lu, T.A. George, Y. Wang, I. Ketsman, J.D. Burton, C.-W. Bark, S. Ryu, D.J. Kim, J. Wang, C. Binek, P.A. Dowben, A. Sokolov, C.-B. Eom, E.Y. Tsymbal, A. Gruverman, Electric modulation of magnetization at the $\text{BaTiO}_3/\text{La}_{0.67}\text{Sr}_{0.33}\text{MnO}_3$ interfaces, *Applied Physics Letters*, 100 (2012) 232904.
- [17] D. Chiba, F. Matsukura, H. Ohno, Electric-field control of ferromagnetism in (Ga,Mn)As, *Applied Physics Letters*, 89 (2006) 162505.



- [18] F. Matsukura, Y. Tokura, H. Ohno, Control of magnetism by electric fields, *Nat. Nanotech*, 10 (2015) 209-220.
- [19] T. Zhao, S.B. Ogale, S.R. Shinde, R. Ramesh, R. Droopad, J. Yu, K. Eisenbeiser, J. Misewich, Colossal magnetoresistive manganite-based ferroelectric field-effect transistor on Si, *Applied Physics Letters*, 84 (2004) 750-752.
- [20] I. Stolichnov, S.W.E. Riestler, H.J. Trodahl, N. Setter, A.W. Rushforth, K.W. Edmonds, R.P. Champion, C.T. Foxon, B.L. Gallagher, T. Jungwirth, Non-volatile ferroelectric control of ferromagnetism in (Ga,Mn)As, *Nat Mater*, 7 (2008) 464-467.
- [21] H.K. Lau, C.W. Leung, Nonvolatile multilevel memory effect by resistive switching in manganite thin films, *Journal of Applied Physics*, 104 (2008) 123705.
- [22] A. Ruotolo, C.W. Leung, C.Y. Lam, W.F. Cheng, K.H. Wong, G.P. Pepe, Unification of bulk and interface electroresistive switching in oxide systems, *Physical Review B*, 77 (2008) 233103.
- [23] A. Ruotolo, C.Y. Lam, W.F. Cheng, K.H. Wong, C.W. Leung, High-quality all-oxide Schottky junctions fabricated on heavily doped Nb:SrTiO₃ substrates, *Physical Review B*, 76 (2007) 075122.
- [24] H.F. Wong, K. Wang, C.W. Leung, K.H. Wong, Magnetoresistance of Manganite-Cobalt Ferrite Spacerless Junctions, *IEEE Transactions on Magnetics*, 50 (2014) 1-4.
- [25] A. Urushibara, Y. Moritomo, T. Arima, A. Asamitsu, G. Kido, Y. Tokura, Insulator-metal transition and giant magnetoresistance in $\text{La}_{1-x}\text{Sr}_x\text{MnO}_3$, *Physical Review B*, 51 (1995) 14103-14109.
- [26] J. Walter, H. Wang, B. Luo, C.D. Frisbie, C. Leighton, Electrostatic versus Electrochemical Doping and Control of Ferromagnetism in Ion-Gel-Gated Ultrathin $\text{La}_{0.5}\text{Sr}_{0.5}\text{CoO}_{3-\delta}$, *ACS Nano*, 10 (2016) 7799-7810.
- [27] C. Song, B. Cui, F. Li, X. Zhou, F. Pan, Recent progress in voltage control of magnetism: Materials, mechanisms, and performance, *Progress in Materials Science*, 87 (2017) 33-82.
- [28] Q. Yang, Z. Zhou, N.X. Sun, M. Liu, Perspectives of voltage control for magnetic exchange bias in multiferroic heterostructures, *Physics Letters A*, 381 (2017) 1213-1222.
- [29] W. Yuan, Y. Zhao, C. Tang, T. Su, Q. Song, J. Shi, W. Han, Epitaxial growth and properties of $\text{La}_{0.7}\text{Sr}_{0.3}\text{MnO}_3$ thin films with micrometer wide atomic terraces, *Applied Physics Letters*, 107 (2015) 022404.
- [30] W.J. Hu, D.-M. Juo, L. You, J. Wang, Y.-C. Chen, Y.-H. Chu, T. Wu, Universal Ferroelectric Switching Dynamics of Vinylidene Fluoride-trifluoroethylene Copolymer Films, 4 (2014) 4772.
- [31] B. Chu, X. Zhou, K. Ren, B. Neese, M. Lin, Q. Wang, F. Bauer, Q.M. Zhang, A Dielectric Polymer with High Electric Energy Density and Fast Discharge Speed, *Science*, 313 (2006) 334-336.
- [32] B. Cui, C. Song, H. Mao, H. Wu, F. Li, J. Peng, G. Wang, F. Zeng, F. Pan, Magnetoelectric Coupling Induced by Interfacial Orbital Reconstruction, *Advanced Materials*, 27 (2015) 6651-6656.



Chapter 5 Electric field-induced oxygen vacancy modulation in perovskite manganite Films gated with ferroelectric polymer

5.1 Introduction

Chemical doping is frequently adopted for manipulating the transport and magnetic properties of complex oxides [1-4]. Recently, efforts have been made in studying electric-field induced manipulation of charge carriers at the oxide interfaces, through the application of voltages across high- k dielectric [5, 6] or ferroelectric materials [5-8]. By electrostatics gating, a change in the areal charge density below 10^{14} cm^{-2} can be obtained.

To achieve even stronger modulation of interfacial carriers, electrolytes or IL were used for achieving the goal by the EDL effect [9, 10]; such a device geometry can induce interfacial capacitance up to tens of $\mu\text{F}\cdot\text{cm}^{-2}$, bringing large changes in carrier densities in the order of 10^{15} cm^{-2} [10]. Aiming at more prominent changes in magnetism, several studies have operated the IL-based devices through redox reaction in the channel layer rather than electrostatic effect [11-15]. Unlike electrostatic control, the manipulation of gated materials through redox reaction can be stable even after the gate voltage is removed [16]. These studies demonstrated tunable metal-insulator transition in manganites [13, 17] as well as superconductivity in iron-based superconductors [18] and two-dimensional materials [19]. On the other hand, due to the corrosive nature of IL, thin protective layers are often required to cover the active channel [20]; alternatively the gating environment should be dehydrated or the devices are operated just above the freezing point of the IL [13]. Such obstacles have limited the applications of IL-based devices.

Many efforts have been made to investigate the electric-field-induced magnetism in LSMO through a FM top electrode [7, 21-24]. These LSMO field-effect devices are mainly governed by polarization-induced carrier modulation in the FE/FM interfaces, and accompanied with the change in transport and magnetic properties. However, most studies of these FE reversal of LSMO devices were electrostatic in nature and used oxide-based FE layers with thicknesses at least tens of nm, making it difficult to study the



interfacial changes upon the ferroelectric-gating process. In this regard, copolymer ferroelectric P(VDF-TrFE) offers an alternative choice due to its low processing temperature ($\sim 140^\circ\text{C}$) [25-27], chemical inert and compatible with group III-V dilute magnetic semiconductors such as (Ga,Mn)As for achieving the electric-field control devices [28]. By dissolving ferroelectric copolymer in the field-effect devices after switching process offer a direct probing of interfacial changes of FM through surface-sensitive probing techniques, which is ideally suitable to investigate the interfacial magnetism due to electrochemical reactions. So far, only a few investigations have been made concerning both electrostatic and electrochemical modulation of transport and magnetic properties of manganites, using FE as the gate dielectric.

In this part of the thesis, I investigate the non-volatile, electrical control in transport and magnetic properties of epitaxial LSMO thin films through a top-gated FET structure with P(VDF-TrFE) as the gate dielectric. Typical modulation of ferromagnet devices via ferroelectrics is vulnerable to dielectric breakdown during the application of large saturation voltage [21, 22, 29]. Such an issue can be avoided by pulses of low-voltages, with magnitudes smaller than that required for the switching of polarization direction in the ferroelectric. In contrary with typical electrostatic modulation through ferroelectrics, it will be shown that the electrochemical control of LSMO layer permits strong manipulation of the transport and magnetic properties through low-voltage-pulse with an assistance of P(VDF-TrFE) as dielectric layer. Detailed chemical characterization on the valency variations of the LSMO channel layer was performed, by exposing the pulsed channel through dissolving the copolymer gate using conventional organic solvent. Both electrostatic and electrochemical modulation of manganites can be achieved through controlling the magnitude of applied voltages and the number of pulses being applied. Through a combination of structural, chemical, transport and magnetic characterization, I will demonstrate that the tunability of transport and magnetic properties in LSMO layer are mainly due O_v modulations during a low-voltage gate-pulsing process. The technique offers a controllable method for modulation the transport and magnetic properties of manganites through O_v modulation, which is more robust compared with direct polarization switching that may lead to dielectric breakdown during the switching process.



5.2 Experimental details

5.2.1 Thin film growth and device fabrication

High-quality LSMO films with thickness 7.5 nm were grown on (001)-oriented STO single crystal substrates, by means of PLD from a stoichiometric target [30-32]. Samples were deposited at a substrate temperature of 700°C in an oxygen pressure of 150 mTorr. The samples were subsequently annealed *in situ* for 5 minutes with an oxygen pressure of 10 Torr, before they were cooled to room temperature with a ramp rate of 10 K/min. The thickness of LSMO thin films was estimated based on a calibration sample, and was further confirmed by XRR measurements.

The LSMO layer was patterned into the Hall bar geometry (channel length 200 μm , channel width 20 μm) by conventional photolithography and inductively coupled plasma etching. Ti (80 nm)/Au (15 nm) electrodes were deposited by electron beam evaporation under a base pressure of 5×10^{-4} Pa. For the ferroelectric copolymer gate, P(VDF-TrFE) with 7:3 molar ratio of VDF and TrFE copolymers was dissolved in diethyl carbonate. The solution was spin-coated onto patterned LSMO tracks, and was subsequently annealed at 120 °C for two hours in order to obtain the ferroelectric β phase [25, 26]. The resultant copolymer film thickness was \sim 250 nm. Top gate electrodes of Al(100 nm)/Au(30 nm) were prepared by e-beam evaporation through a stainless steel shadow mask.

5.2.2 Structural characterization

XRD and XRR measurements were conducted using a high-resolution Rigaku Smartlab X-ray diffractometer with Cu- K_{α} radiation ($\lambda = 1.5406 \text{ \AA}$). XPS was performed with a Sengyang SKL-12 electron spectrometer equipped with a VG CLAM 4 MCD electron energy analyzer and twin anode Mg K_{α} radiation (1253.6 eV) or Al K_{α} radiation (1496.3 eV) X-ray sources. The base pressure for the XPS measurement was 2×10^{-9} Torr. All binding energies in this work were calibrated with the C $1s$ peak (284.6 eV).

5.2.3 Electrical and magnetic measurements

Electrical measurements of the samples were conducted in a closed-cycle cryostat evacuated to a pressure of 10^{-4} Torr. The LSMO channel resistance was then measured



through standard four-point probe method using a Keithley 2400 sourcemeter. *R-T* and MR measurements with in-plane applied magnetic field were conducted using a Keithley 2182A nanovoltmeter and a Keithley 6221 DC/AC current source.

5.3 Results and discussions

5.3.1 Structural and ferroelectric characterization

Before investigating the LSMO-based devices, the structural properties of LSMO films grown on (001) oriented TiO₂ terminated-STO substrates were studied. Kiessig fringes in XRR measurements (Figure 5. 1 (a)) indicate a film thickness about 7.5 nm with surface roughness ~ 0.43 nm, consistent with the results obtained from AFM measurement (0.38 nm, inset of Figure 5. 1 (a)). The AFM image also exhibits an atomically flat LSMO surface with clear terraces of step height ~ 0.38 nm, consistent with the unit-cell height of LSMO along the (001) cleavage plane. Such several hundred-nm-wide terraces in LSMO are due to DI water treated STO substrate before LSMO deposition, as mentioned in Chapter 2.

The ferroelectric properties of P(VDF-TrFE) strongly depends on its crystallinity. XRD pattern of P(VDF-TrFE) on LSMO film (inset, Figure 5. 1 (b)) shows the peak for (200) and (110) planes of P(VDF-TrFE) at $\sim 19^\circ$, after annealing the sample in air at 120 °C for two hours, implying the presence of the ferroelectric β phase [27]. Ferroelectric hysteresis loop of P(VDF-TrFE) film (Figure 5. 1 (b)) measured at 100 kHz and 300 K exhibits a remnant polarization of $10 \mu\text{C}\cdot\text{cm}^{-2}$, coercive voltage of 15 V and saturation voltage of 40 V. The results demonstrate the good ferroelectric performance of the copolymer layer prepared in this work.

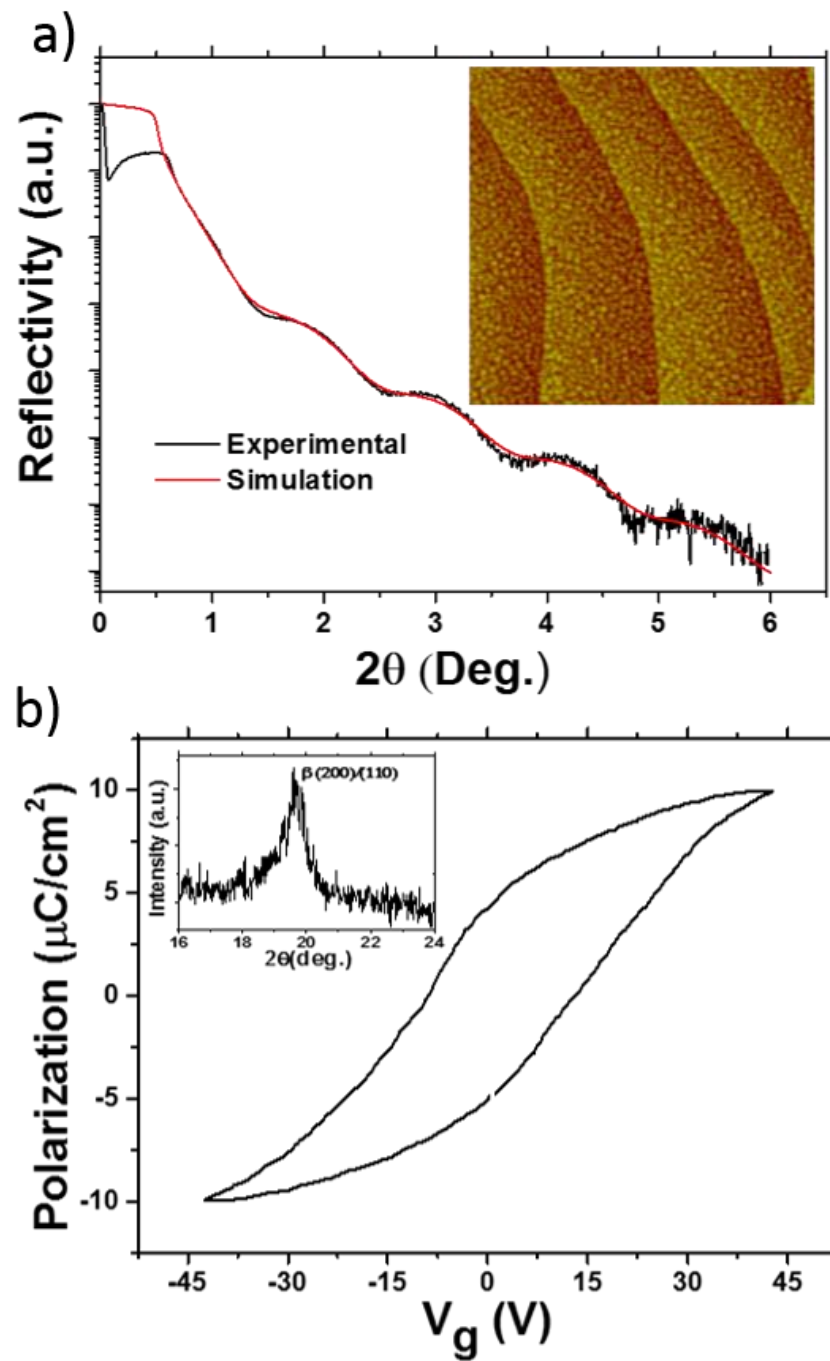


Figure 5. 1 (a) XRR measurement of LSMO film grown on TiO_2 -terminated STO (001) substrate. Inset shows AFM scan of the LSMO film (scan area = $1 \mu\text{m}^2$). (b) Polarization hysteresis loop of $\text{P}(\text{VDF-TrFE})$ prepared on glass substrate, with the inset showing the XRD θ - 2θ scan profile of $\text{P}(\text{VDF-TrFE})$ on LSMO film surface.



5.3.2 Transport characterization

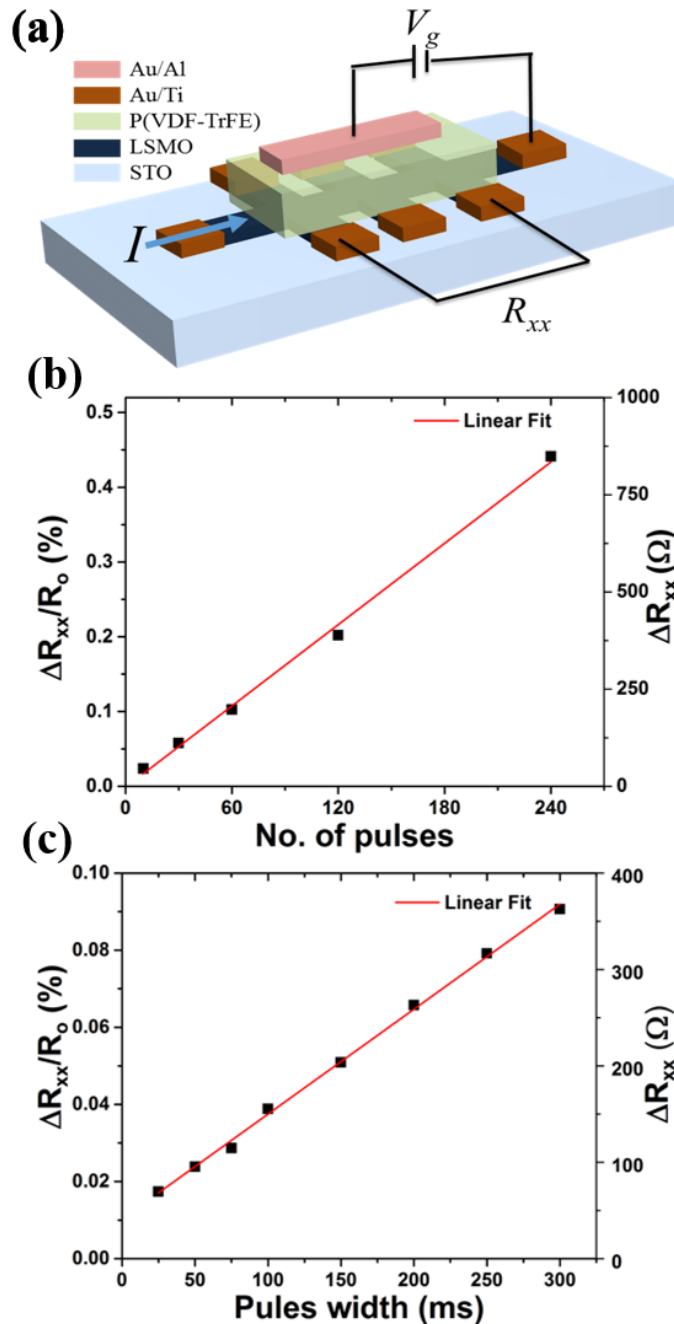


Figure 5. 2 (a) Schematics diagram of the FET device with LSMO channel and P(VDF-TrFE) gate. The plots in (b) and (c) show the resistance change $\Delta R_{xx}/R_0$ (left axis) and ΔR_{xx} (right axis) of LSMO channel as functions of different pulse parameters: (b) number of pulse cycles (for constant pulse amplitude of 10 V and width of 300 ms); (c) pulse width (for constant pulse amplitude of 10 V and pulse cycles of 60).

It was mentioned in Chapter 4 that insignificant T_C of LSMO were observed when V_g was larger than the voltage required to switch the polarization direction of P(VDF-TrFE). Rather than providing a single pulse of V_g , the tunability of electrical and magnetic



properties in LSMO devices were also examined through successive-low-pulsing cycles. In the following sections, R_{xx} is defined as the longitudinal resistance of the LSMO device as measured by four-point measurement, and V_g is the potential applied to the P(VDF-TrFE) gate with reference to the LSMO channel (drain) potential; unless otherwise stated, the V_g magnitude, pulse width and pulse cycle are equal to 10 V, 300 ms and 500 ms respectively. Figure 5. 2 (a) illustrates the resistance measurement on the LSMO device with P(VDF-TrFE) gate dielectric.

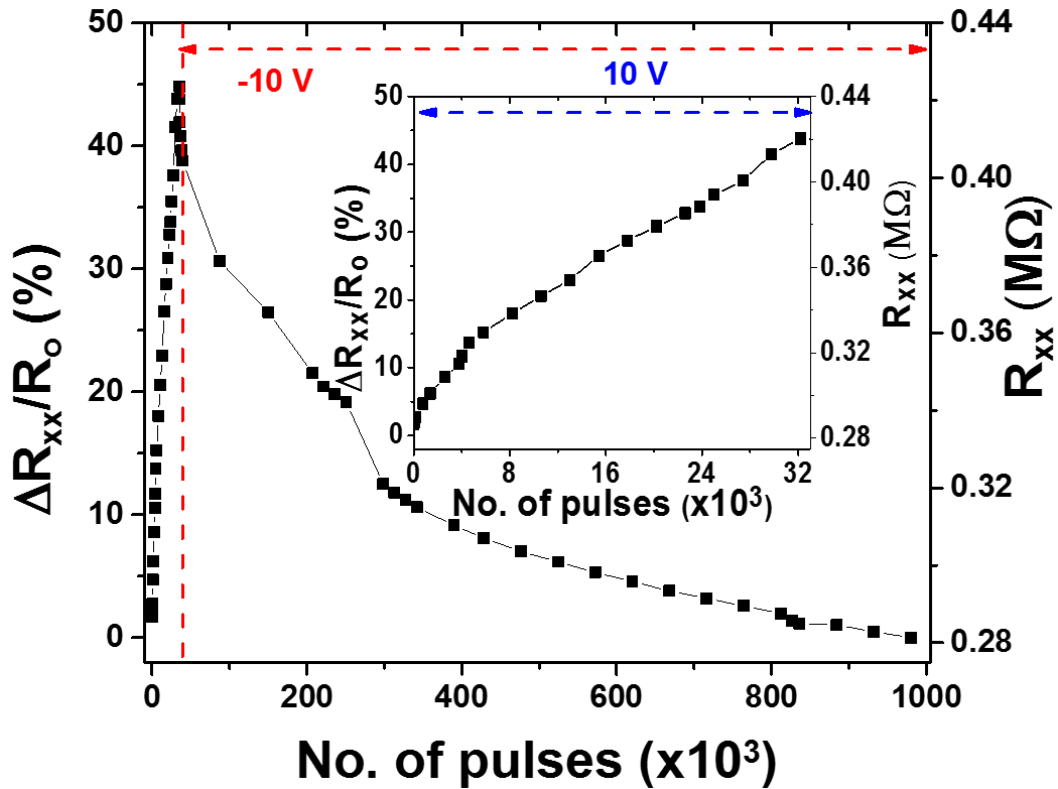


Figure 5. 3 $\Delta R_{xx}/R_o$ (left axis) and R_{xx} (right axis) in response to successive +10 V (first 30k) and -10 V (up to 10^6) pulses with constant pulse width (300 ms). Inset of figure highlights the switching-up process in LSMO $\Delta R_{xx}/R_o$ (left axis) and R_{xx} during the +10 V pulse cycles at the beginning of the measurement in the main figure.

Figure 5. 2 (b) and 5. 2 (c) present the transport properties of LSMO channel at 300 K, after undergoing various V_g pulse cycles. Here ΔR_{xx} and $\Delta R_{xx}/R_o$ (%) and are defined as $R_{xx}(n)-R_{xx}(0)$ and $(R_{xx}(n)-R_{xx}(0))/R_{xx}(0)$ respectively, where n is the number of pulses applied to the channel and $R_o = R_{xx}(n = 0)$ refers to the channel resistance at the start of the measurement before V_g was applied. The results indicate that $\Delta R_{xx}/R_o$ positively correlates with the number of pulse cycles (Figure 5. 2 (b)) and the pulse width (Figure 5. 2 (c)).



To further investigate the behavior of $\Delta R_{xx}/R_o$ in response to V_g pulses, I reversed the sign of V_g after the application of a series of positive V_g pulses. Figure 5. 3 reveals the gradual change in $\Delta R_{xx}/R_o$ at 300 K upon the application of successive positive and negative V_g pulses. Initially, $\Delta R_{xx}/R_o$ shows a continuous increase (by up to 45% from R_o) upon the application of $+V_g$ (10 V). When the sign of V_g is reversed, R_{xx} gradually returns to the initial value. One can notice in Figure 5. 3 that it is more difficult to reduce R_{xx} through the application of negative V_g , as more pulse cycles are required for returning R_{xx} back to the original level ($\sim 30k$ pulses for $+V_g$ vs. 10^6 pulses for $-V_g$).

The asymmetric switching of resistance with V_g of the same magnitude but opposite signs is reminiscent with the studies of electric-field control of transport properties in manganites through IL gating [13]; in the electrostatic regime, R_{xx} increases by 20% for $V_g = 1$ V, while $\Delta R_{xx}/R_o$ decreases only 4% for $V_g = -2$ V. In contrast, in the present case of Figure 5. 2, a change of 45 % was recorded, but clearly this is not the limit for $\Delta R_{xx}/R_o$ judging from its linearly increasing trend. It should also be mentioned that the resistance-switching process in this experiment was performed in vacuum ($<10^{-4}$ Torr).

Transport and magnetism of LSMO films depend heavily on the ratio of La^{3+} and Sr^{2+} , leading to the varying ratio of 3+ and 4+ Mn valence states [33]. Apart from controlling the growth condition of manganites films, recent work with IL modulation of manganite thin films showed the possibility to generate O_v by using large V_g , as the formation enthalpy of O_v is small [13, 17]. The V_g applied to the device in Figure 5. 2 to Figure 5. 3 is far below the saturation field for ferroelectric reversal of P(VDF-TrFE), and hence is inadequate to explain the dependence of R_{xx} modulation with low-voltage-pulse cycles and the asymmetric LSMO channel response between positive and negative V_g pulses.

It is therefore postulated that the creation and annihilation of O_v in LSMO channel, with an assistance of repeated V_g pulses, plays an important role in the electrochemical reaction within the LSMO layer [34, 35]. As discussed in previous work involving LSMO gated with IL, the electric field provided by IL is enough to drive the O_v accumulation near the LSMO interfaces, weakening the ferromagnetic properties of the LSMO channel [17]. The process can be described by the following equation:

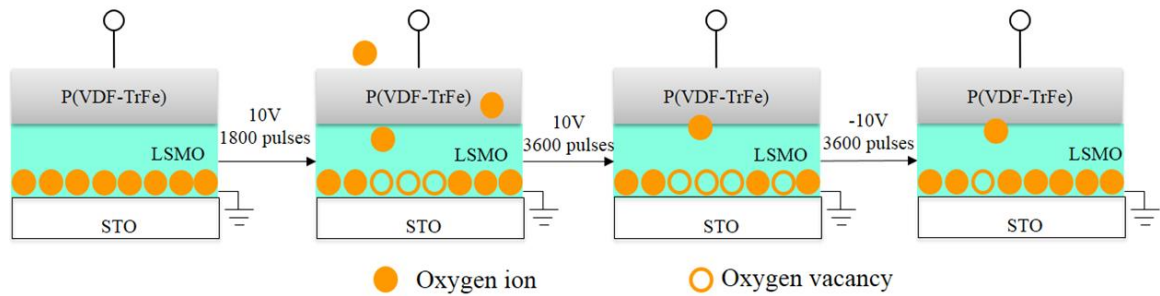
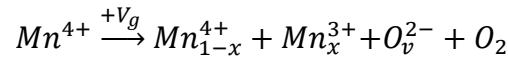


Figure 5. 4 Evolution of V_o in LSMO channel with successive positive and negative V_g pulses, according to the proposed electrochemical switching mechanism.

Figure 5. 4 depicts the schematic of the proposed model of O_v modulation in LSMO. As $+V_g$ pulses are applied, n -type carriers (in form of O_v) are created and gradually diffuse from the LSMO/P(VDF-TrFE) interface to the bulk of LSMO film. Some LSMO lattices gradually change from metallic ferromagnet phase to insulating ferromagnet phase at the interface, and the “insulating” layer is extended through the interfaces. Such an increase in the O_v concentration induces additional resistance throughout the interface region due to the p -type nature of LSMO. The scenario is reversed when $-V_g$ pulses are applied which induces the depletion (in form of annihilation of O_v) back to LSMO lattice and leads to a drop of LSMO resistance.

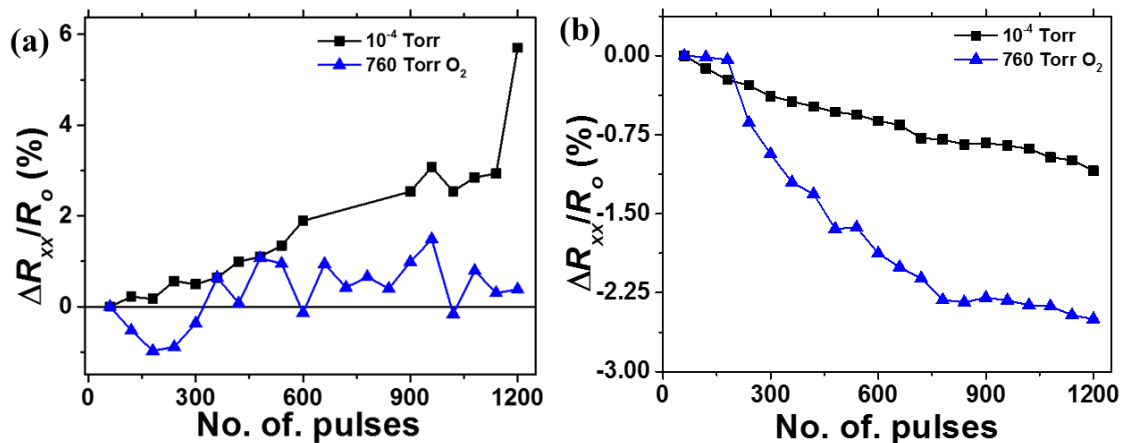


Figure 5. 5 Variation of ΔR_{xx} of LSMO channel as a function of V_g pulse number in different environment. (a) $+V_g$ cycles in vacuum (squares) and oxygen (triangles) environment. (b) $-V_g$ cycles in vacuum (squares) and oxygen (triangles) environment.



To verify the possible electrochemical variation (O_v annihilation/formation) in LSMO channel during the application of V_g pulses, the V_g dependence of ΔR_{xx} under oxygen and vacuum environment were conducted at 300 K (Figure 5. 5). One would expect the lack of any dependence between different the gas environment and $\Delta R_{xx}/R_o$ upon V_g pulsing, shall the resistance change is due to electrostatic effect. On the other hand, the electrochemical reaction associated with O_v formation (annihilation) in LSMO channel would induce larger changes in $\Delta R_{xx}/R_o$ in the vacuum (oxygen) environment. In the case of $+V_g$ pulses (Figure 5. 5 (a)), while insignificant $\Delta R_{xx}/R_o$ change is observed when it is switched in the O_2 environment, a gradual $\Delta R_{xx}/R_o$ increase is obtained if the sample is pulsed in vacuum ($\sim 10^{-4}$ Torr). The result indicates that the vacuum environment can accelerate the response LSMO channel resistance, as a consequence of the efficient removal of oxygen (i.e. creation of O_v) under the vacuum. For $-V_g$ pulses (Figure 5. 5 (b)), although a $\Delta R_{xx}/R_o$ drop is observed in both vacuum and oxygen environment, the effect is doubled in the presence of oxygen. This indicates that incorporation of oxygen into LSMO channel helps to annihilate O_v . The results are consistent with the study of electric field-induced migration of O_v modulation in VO_2 under IL gating [16].

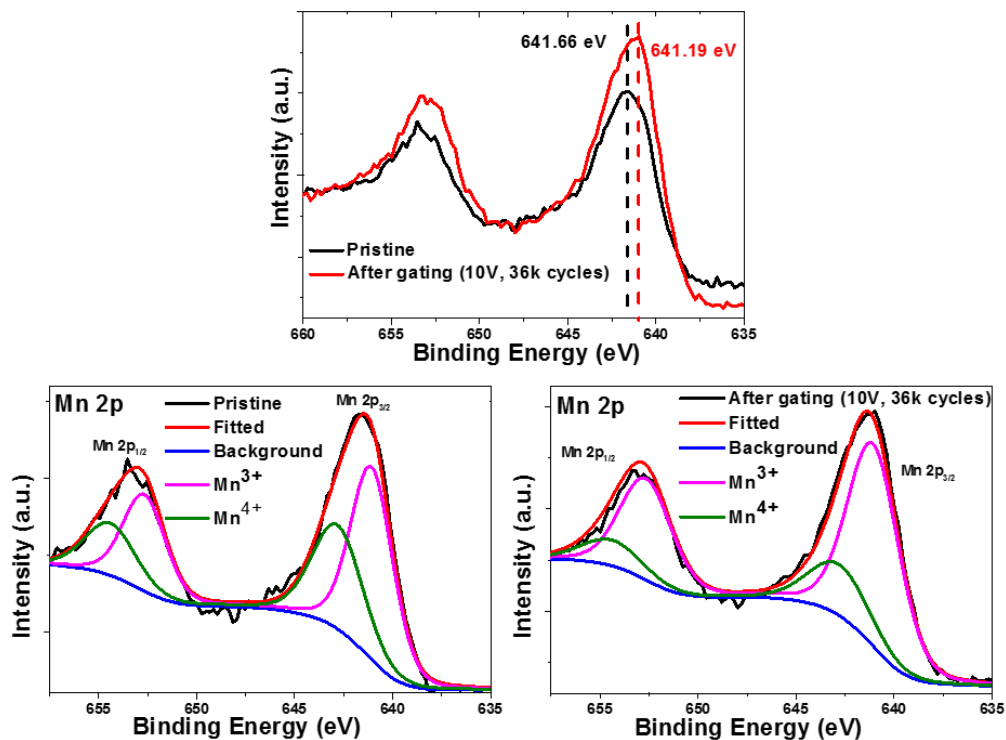


Figure 5. 6 (a) Mn 2p XPS spectra of LSMO film at pristine state and after $+V_g$ pulsing for 36,000 cycles. (b) and (c) shows the multiple peak fitting of the XPS spectra for pristine (b) and gated (c) samples.



The change in the valence state of Mn ions provides additional evidence to support the hypothesis of O_v formation in LSMO. Here, XPS was employed to analyze the LSMO channel at pristine state and after gating with 36k $+V_g$ pulses. For direct probing of the LSMO channel, the top Al electrode and the copolymer gate dielectric were removed by acetone after the application of $+V_g$ pulses, before the samples were transferred into the XPS chamber. Figure 5. 6 (a) depicts the Mn $2p$ core-level spectra of the pristine and $+V_g$ -pulsed samples. The position of the Mn $2p_{3/2}$ core-level peak in the pristine LSMO device is 641.66 eV. After pulsing the LSMO channel, the Mn $2p_{3/2}$ core-level spectra shifts towards a lower binding energy by 0.47 eV, indicating a decrease in the ratio of $Mn^{4+}/(Mn^{3+}+Mn^{4+})$ as the LSMO sample is pulsed with 36k $+V_g$ pulses [17].

To quantitatively understand the Mn valence change in the LSMO channel, the XPS spectra were assessed with multiple peak fitting by the Xpspeak software, the results of which are shown in Figure 5. 6 (b)-(c). The ratio of Mn^{4+} ions to $(Mn^{3+}+Mn^{4+})$ changes from 0.39 to 0.23 after $+V_g$ pulse cycles. The observation indicates that the oxidation state of Mn states evolves from Mn^{4+} to Mn^{3+} upon the application of $+V_g$ pulses. As the XPS were performed after the removal of the P(VDF-TrFE) layer, any polarization effect on the LSMO channel should have been removed by the time of XPS measurements. The observed valence state change of Mn ions due to V_g pulse chains is therefore electrochemical in nature.

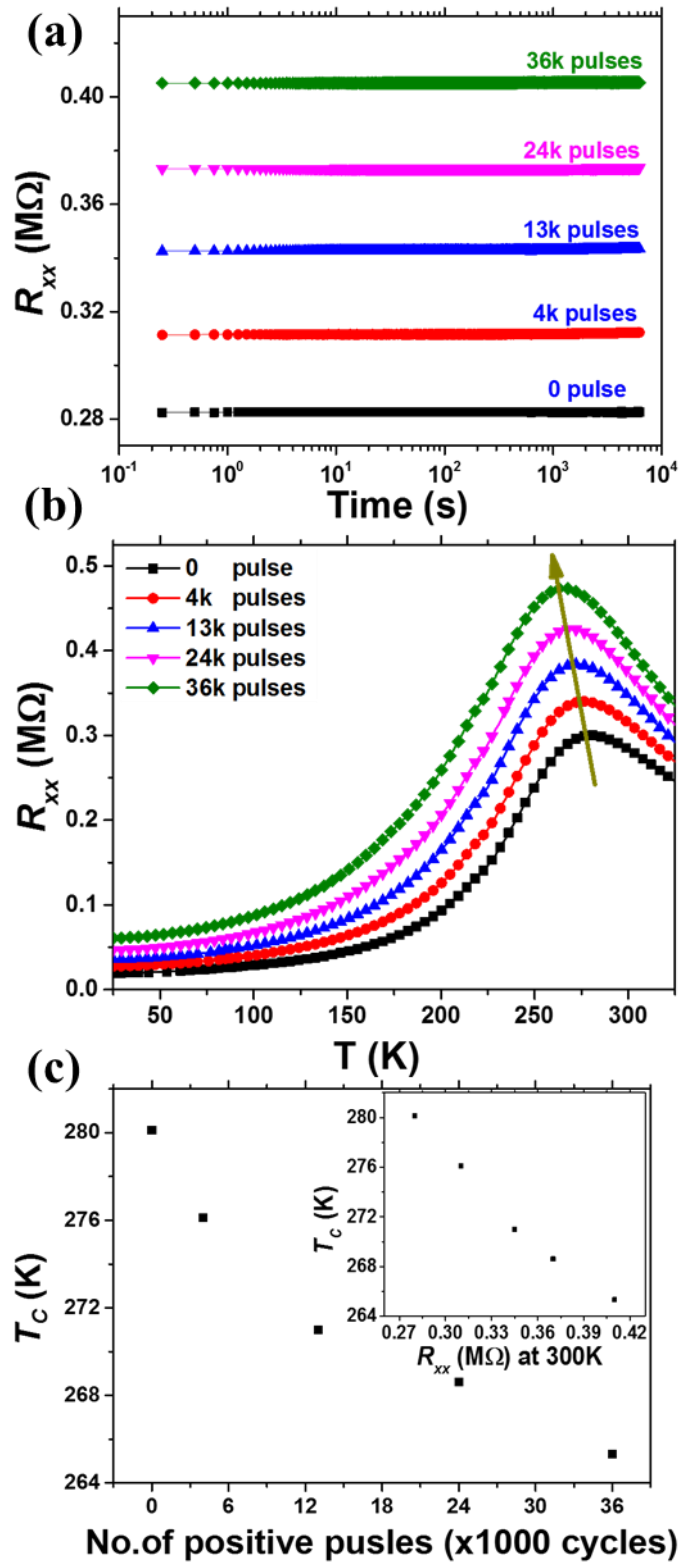


Figure 5. 7 (a) Time profile of LSMO channel resistance as a function of $+V_g$ from 0 to 36k cycles. (b) R-T measurement for sample undergone various positive V_g cycles. (c) Change in T_c as a function of positive V_g cycles (main figure) and R_{xx} at 300 K (inset).



The results in Figure 5. 5 and 5. 6 provide strong supports for the hypothesis of O_v formation and annihilation as the origin of modulated LSMO properties. $+V_g$ chains through the ferroelectric copolymer effectively drives oxygen out of the LSMO channel and creates O_v , accompanied by a valence transition of Mn^{4+} to Mn^{3+} . Enhancement of Mn^{3+} would lead to a few portions of magnetic order changing from Mn^{3+} -O- Mn^{4+} (ferromagnetic) to Mn^{3+} -O- Mn^{3+} (antiferromagnetic) interaction.

After proving the electric-field-induced O_v modulation in LSMO channel, it is worthwhile to investigate the tunability of transport and magnetic properties in LSMO channel under successive V_g pulsing. The possibility of driving the LSMO channel resistance through the application of V_g implies its potential for multilevel memory applications [30, 35]. Figure 5. 7 demonstrates the performance of LSMO channel upon the application of various $+V_g$ cycles. As shown in Figure 5. 7 (a), R_{xx} increases from 0.28 M Ω to 0.41 M Ω through the application of 36k pulses, and it remains steady once $+V_g$ is removed. Such a non-volatile resistance behavior can be explained by the O_v creation, which gives rise to additional resistance.

Meanwhile, R - T measurement is a good indicator for observing the variation of magnetic properties in LSMO upon the application of pulse voltages. Figure 5. 7 (b) depicts the temperature-dependent LSMO channel resistance after the application of $+V_g$ pulses at room temperature. Two things can be observed in the figure. Firstly, there is an increasing trend of R_{xx} at all temperatures with increasing number of $+V_g$ pulses, as evidenced by the gradual upward shift of the R - T traces. Besides, the peak position of the R - T curves (at which $dR/dT = 0$), which correspond to the metal-insulator transition temperature of LSMO, gradually shifts to lower values with more V_g pulses; for LSMO the R - T trace peak is basically equivalent to its T_C [4]. In Figure 5. 7 (c) the change in T_C is plotted as a function of applied pulses at 300 K. The application of $+V_g$ cycle gradually reduces the LSMO channel T_C from 280 K (pristine sample) to 265 K (after 36k pulses). Such an observation implies that more O_v are gradually created from LSMO channel upon the application of positive pulses.

For further investigation, the variation of the T_C with the room-temperature LSMO channel resistance (inset of Fig. 4 (c)) is plotted. The $+V_g$ cycle makes the LSMO films



more insulating at room-temperature and lead to reduced T_C . By considering the correlation between n and T_C in LSMO [7]: $\frac{\Delta n}{n} \propto \frac{\Delta T_C}{T_C}$, a shift of T_c by 15 K corresponds to a 7% variation of n .

5.3.3 Magnetic characterization

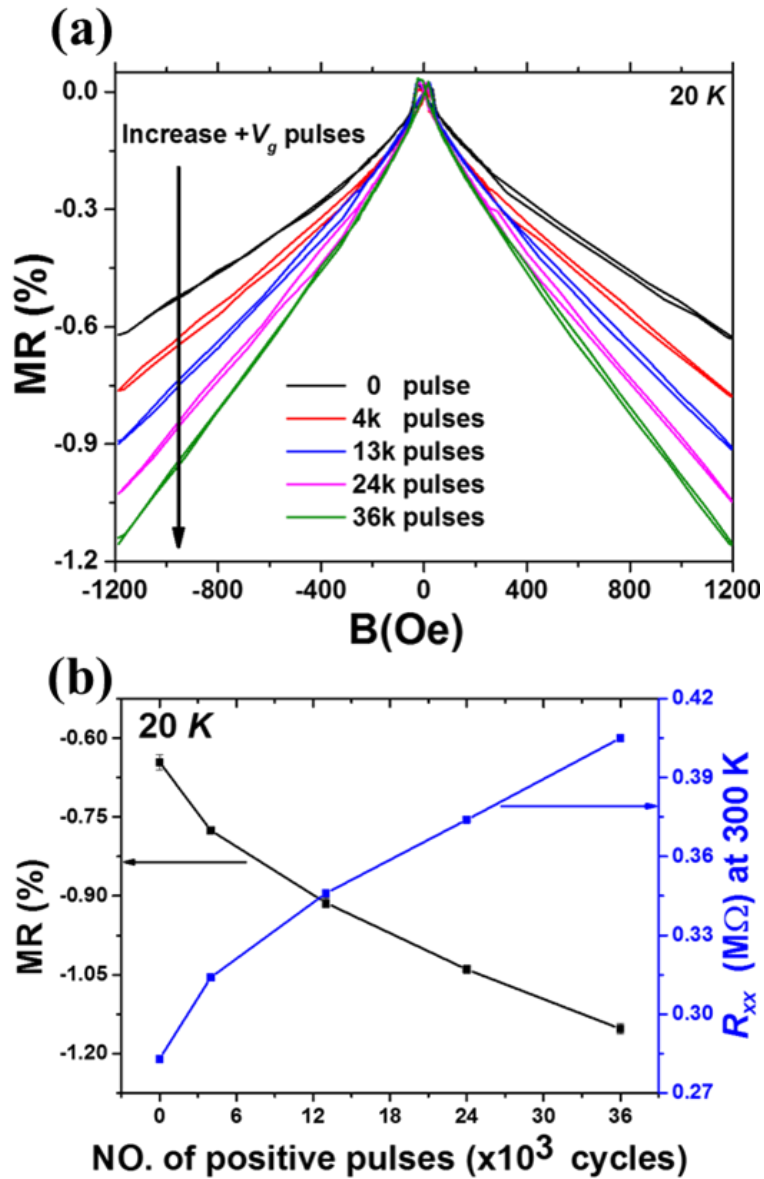


Figure 5. 8 Variation of LSMO channel magnetotransport properties at 20 K with applied $+V_g$, (a) MR behavior for LSMO channel undergone $+V_g$ pulse cycles; the inset indicates the magnified view of MR loop, after the application of 36k $+V_g$ pulses. (b) MR ratio (20 K) and R_{xx} (300 K) as a function of $+V_g$ pulse cycle at 300K.



To further study the modulation of magnetic properties in LSMO channel due to V_g pulsing, MR measurements (i.e. dependence of R_{xx} on external in-plane magnetic field B) were conducted in the LSMO channel. Figure 5. 8 (a) depicts the MR of the LSMO channel at $T = 20$ K, upon the application of $+V_g$ pulse cycles from 0 ,4, 13, 24 and 36 k at 300 K. Here the MR ratio is defined as $(R_{xx}(B) - R_{xx}(0))/R_{xx}(0)$, where $R_{xx}(B)$ and $R_{xx}(0)$ are the LSMO channel resistance with and without magnetic field. As shown in Figure 5. 8 (b), the LSMO channel exhibits increasingly negative MR characteristic from -0.65 % to -1.15 % at $B = 1200$ Oe upon the application of 36k $+V_g$ pulses, reflecting the increasingly insulating nature of the LSMO in response to accumulated $+V_g$ pulses applied. In the current case, the increase in $+V_g$ pulse cycle would lead to a decrease in T_C , and result in the increases in negative MR values. Such a trend of MR values is consistent with the scenario in which the MR effect in manganites is the largest around T_C , and becomes smaller when it is far below T_C [4]. These effects can originate from the accumulation of O_v at P(VDF-TrFE)/LSMO interfaces, which is consistent with decrease in T_C in the sample.

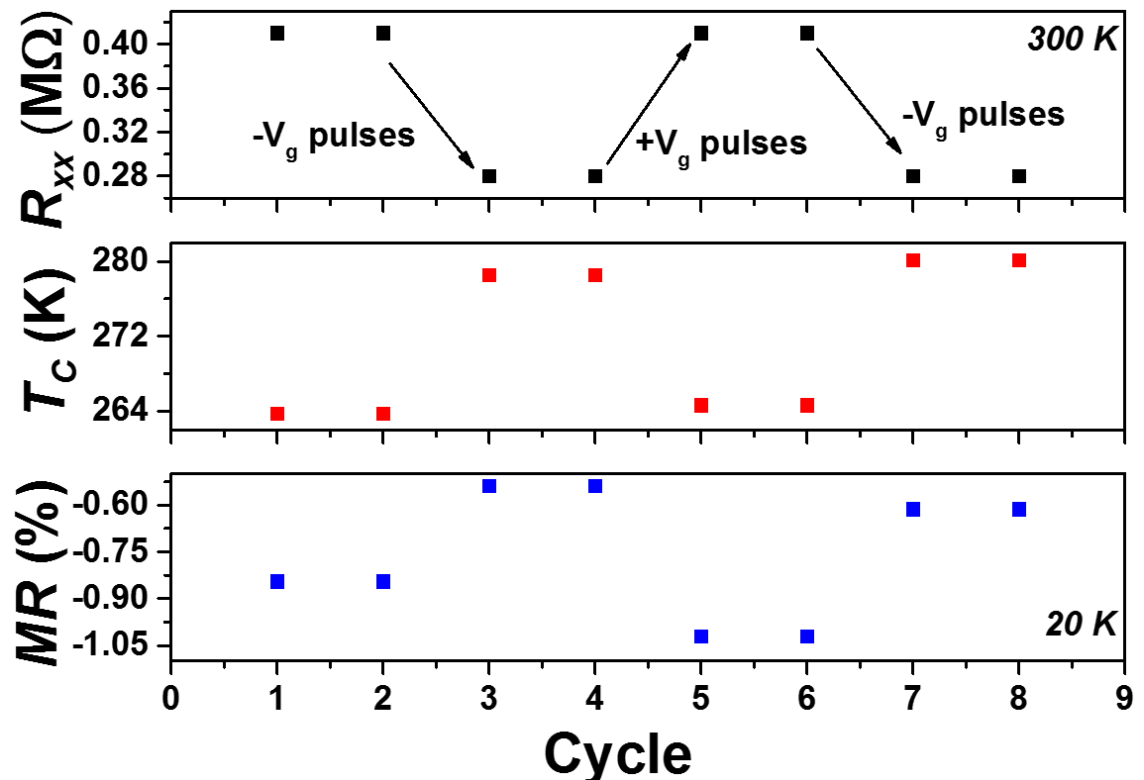


Figure 5. 9 Reversibility of LSMO channel resistance at 300 K (a), T_c of LSMO (b), and MR of LSMO channel at 20 K (c), through the application of positive and negative V_g pulses. Note that the number of pulses in each 'cycle' (x-axis of the graphs) are different (c.f. Fig. 5. 2).



To verify the reversibility of observed modulation effects in LSMO channel resistance, successive positive and negative V_g pulses were applied and the corresponding electrical properties of the LSMO channel were measured. Figure 5. 9 (a)-(c) depict the R_{xx} , T_C and MR value between ± 1200 Oe through the application of positive and negative V_g pulses. At the start of the experiment, R_{xx} is $0.41 \text{ M}\Omega$ at 300 K, and T_C of the LSMO channel is 264 K for both heating and warming cycles, while the MR values at 20 K is measured as -0.85% . With the application of $-V_g$ pulses, R_{xx} becomes $0.28 \text{ M}\Omega$ at 300 K, accompanied by an enhancement in ferromagnetic properties as reflected from the increase in T_C by 16 K. It is suggested that decrease in R_{xx} in 300 K and increase in T_C of LSMO channel is due to O_v annihilation, which is consistent with reduction of magnetic scattering at low-temperature MR measurement (-0.55%). With the further application of $-V_g$ pulses, T_C and MR value at 20 K resume previous values while the R_{xx} at room temperature is reset back to $0.41 \text{ M}\Omega$. This indicates that the gate-induced creation of O_v in LSMO channel can be achieved by the application of $-V_g$ pulse cycle. The tunability in transport and magnetic properties of these LSMO device through low- V_g pulses operates with a mechanism different from the electrostatic effect, and the results show strong support on the electrochemical switching of the LSMO film.

5.4 Conclusion

In summary, the electric-field manipulation in transport and magnetic properties of ultra-thin LSMO film through low- V_g pulsing across a P(VDF-TrFE) gate was reported. The results showed strong support on the O_v vacancy movement as the mechanism for the reversible transport and magnetic properties switching in the LSMO devices. Comparing with the modulation due to electrostatic effect through polarization reversal in P(VDF-TrFE), the electrochemical reaction process in LSMO layer offers strong tunability in both T_C and MR at 20 K. The results indicated that low-voltage gate-pulsing method is a promising candidate to enhance the manipulation of transport and magnetism in the complex oxide system.



References for Chapter 5

- [1] J. Hemberger, A. Krimmel, T. Kurz, H.A. Krug von Nidda, V.Y. Ivanov, A.A. Mukhin, A.M. Balbashov, A. Loidl, Structural, magnetic, and electrical properties of single-crystalline $\text{La}_{1-x}\text{Sr}_x\text{MnO}_3$ ($0.4 < x < 0.85$), *Physical Review B*, 66 (2002) 094410.
- [2] X.L. Wang, K.H. Lai, A. Ruotolo, A comparative study on the ferromagnetic properties of undoped and Mn-doped ZnO, *Journal of Alloys and Compounds*, 542 (2012) 147-150.
- [3] X.L. Wang, Q. Shao, A. Zhuravlyova, M. He, Y. Yi, R. Lortz, J.N. Wang, A. Ruotolo, Giant negative magnetoresistance in Manganese-substituted Zinc Oxide, *Scientific Reports*, 5 (2015) 9221.
- [4] A. Urushibara, Y. Moritomo, T. Arima, A. Asamitsu, G. Kido, Y. Tokura, Insulator-metal transition and giant magnetoresistance in $\text{La}_{1-x}\text{Sr}_x\text{MnO}_3$, *Physical Review B*, 51 (1995) 14103-14109.
- [5] C.H. Ahn, A. Bhattacharya, M. Di Ventura, J.N. Eckstein, C.D. Frisbie, M.E. Gershenson, A.M. Goldman, I.H. Inoue, J. Mannhart, A.J. Millis, A.F. Morpurgo, D. Natelson, J.-M. Triscone, Electrostatic modification of novel materials, *Reviews of Modern Physics*, 78 (2006) 1185-1212.
- [6] C.H. Ahn, J.M. Triscone, J. Mannhart, Electric field effect in correlated oxide systems, *Nature*, 424 (2003) 1015-1018.
- [7] X. Hong, A. Posadas, A. Lin, C.H. Ahn, Ferroelectric-field-induced tuning of magnetism in the colossal magnetoresistive oxide $\text{La}_{1-x}\text{Sr}_x\text{MnO}_3$, *Physical Review B*, 68 (2003) 134415.
- [8] H.F. Wong, S.M. Ng, W.F. Cheng, Y. Liu, X. Chen, D. von Nordheim, C.L. Mak, J. Dai, B. Ploss, C.W. Leung, Enhanced tunability of electrical and magnetic properties in $(\text{La,Sr})\text{MnO}_3$ thin films via field-assisted oxygen vacancy modulation, *Solid-State Electron.*, 138 (2017) 56-61.
- [9] M. Galiński, A. Lewandowski, I. Stępiak, Ionic liquids as electrolytes, *Electrochimica Acta*, 51 (2006) 5567-5580.
- [10] T. Fujimoto, K. Awaga, Electric-double-layer field-effect transistors with ionic liquids, *Physical Chemistry Chemical Physics*, 15 (2013) 8983-9006.
- [11] T.D. Schladt, T. Graf, N.B. Aetukuri, M. Li, A. Fantini, X. Jiang, M.G. Samant, S.S.P. Parkin, Crystal-Facet-Dependent Metallization in Electrolyte-Gated Rutile TiO_2 Single Crystals, *ACS Nano*, 7 (2013) 8074-8081.
- [12] Y. Zhou, J. Park, J. Shi, M. Chhowalla, H. Park, D.A. Weitz, S. Ramanathan, Control of Emergent Properties at a Correlated Oxide Interface with Graphene, *Nano Letters*, 15 (2015) 1627-1634.
- [13] J. Walter, H. Wang, B. Luo, C.D. Frisbie, C. Leighton, Electrostatic versus Electrochemical Doping and Control of Ferromagnetism in Ion-Gel-Gated Ultrathin $\text{La}_{0.5}\text{Sr}_{0.5}\text{CoO}_{3-\delta}$, *ACS Nano*, 10 (2016) 7799-7810.
- [14] D. Passarello, S.G. Altendorf, J. Jeong, M.G. Samant, S.S.P. Parkin, Metallization of Epitaxial VO_2 Films by Ionic Liquid Gating through Initially Insulating TiO_2 Layers, *Nano Letters*, 16 (2016) 5475-5481.
- [15] H. Ji, J. Wei, D. Natelson, Modulation of the Electrical Properties of VO_2 Nanobeams Using an Ionic Liquid as a Gating Medium, *Nano Letters*, 12 (2012) 2988-2992.
- [16] J. Jeong, N. Aetukuri, T. Graf, T.D. Schladt, M.G. Samant, S.S.P. Parkin, Suppression of Metal-Insulator Transition in VO_2 by Electric Field-Induced Oxygen Vacancy Formation, *Science*, 339 (2013) 1402-1405.



- [17] B. Cui, C. Song, G. Wang, Y. Yan, J. Peng, J. Miao, H. Mao, F. Li, C. Chen, F. Zeng, F. Pan, Reversible Ferromagnetic Phase Transition in Electrode-Gated Manganites, *Advanced Functional Materials*, 24 (2014) 7233-7240.
- [18] J. Shiogai, Y. Ito, T. Mitsuhashi, T. Nojima, A. Tsukazaki, Electric-field-induced superconductivity in electrochemically etched ultrathin FeSe films on SrTiO₃ and MgO, *Nat Phys*, 12 (2016) 42-46.
- [19] J.T. Ye, S. Inoue, K. Kobayashi, Y. Kasahara, H.T. Yuan, H. Shimotani, Y. Iwasa, Liquid-gated interface superconductivity on an atomically flat film, *Nat Mater*, 9 (2010) 125-128.
- [20] Y. Wang, X. Zhou, C. Song, Y. Yan, S. Zhou, G. Wang, C. Chen, F. Zeng, F. Pan, Electrical Control of the Exchange Spring in Antiferromagnetic Metals, *Advanced Materials*, 27 (2015) 3196-3201.
- [21] H. Lu, T.A. George, Y. Wang, I. Ketsman, J.D. Burton, C.-W. Bark, S. Ryu, D.J. Kim, J. Wang, C. Binek, P.A. Dowben, A. Sokolov, C.-B. Eom, E.Y. Tsymbal, A. Gruverman, Electric modulation of magnetization at the BaTiO₃/La_{0.67}Sr_{0.33}MnO₃ interfaces, *Applied Physics Letters*, 100 (2012) 232904.
- [22] S.M. Wu, S.A. Cybart, D. Yi, J.M. Parker, R. Ramesh, R.C. Dynes, Full Electric Control of Exchange Bias, *Physical Review Letters*, 110 (2013) 067202.
- [23] T. Wu, S.B. Ogale, J.E. Garrison, B. Nagaraj, A. Biswas, Z. Chen, R.L. Greene, R. Ramesh, T. Venkatesan, A.J. Millis, Electroresistance and Electronic Phase Separation in Mixed-Valent Manganites, *Physical Review Letters*, 86 (2001) 5998-6001.
- [24] B. Cui, C. Song, H. Mao, H. Wu, F. Li, J. Peng, G. Wang, F. Zeng, F. Pan, Magnetoelectric Coupling Induced by Interfacial Orbital Reconstruction, *Advanced Materials*, 27 (2015) 6651-6656.
- [25] B. Ploss, B. Ploss, Dielectric nonlinearity of PVDF-TrFE copolymer, *Polymer*, 41 (2000) 6087-6093.
- [26] D. Von Nordheim, S. Hahne, B. Ploss, Polarisation Readout and Determination of Landau Parameters of VDF-TrFE Thin Films from Dielectric Nonlinearities, *Ferroelectrics*, 453 (2013) 122-126.
- [27] W.J. Hu, D.-M. Juo, L. You, J. Wang, Y.-C. Chen, Y.-H. Chu, T. Wu, Universal Ferroelectric Switching Dynamics of Vinylidene Fluoride-trifluoroethylene Copolymer Films, 4 (2014) 4772.
- [28] I. Stolichnov, S.W.E. Riester, H.J. Trodahl, N. Setter, A.W. Rushforth, K.W. Edmonds, R.P. Champion, C.T. Foxon, B.L. Gallagher, T. Jungwirth, Non-volatile ferroelectric control of ferromagnetism in (Ga,Mn)As, *Nat Mater*, 7 (2008) 464-467.
- [29] S. Fusil, V. Garcia, A. Barthélémy, M. Bibes, Magnetoelectric Devices for Spintronics, *Annual Review of Materials Research*, 44 (2014) 91-116.
- [30] H.K. Lau, C.W. Leung, Nonvolatile multilevel memory effect by resistive switching in manganite thin films, *Journal of Applied Physics*, 104 (2008) 123705.
- [31] A. Ruotolo, C.W. Leung, C.Y. Lam, W.F. Cheng, K.H. Wong, G.P. Pepe, Unification of bulk and interface electroresistive switching in oxide systems, *Physical Review B*, 77 (2008) 233103.
- [32] W.F. Cheng, A. Ruotolo, Y.K. Chan, K.H. Wong, C.W. Leung, Spacerless metal-manganite pseudo-spin-valve structure, *Journal of Applied Physics*, 103 (2008) 103903.
- [33] C. Zener, Interaction between the d-Shells in the Transition Metals. II. Ferromagnetic Compounds of Manganese with Perovskite Structure, *Physical Review*, 82 (1951) 403-405.



- [34] Y.B. Nian, J. Strozier, N.J. Wu, X. Chen, A. Ignatiev, Evidence for an Oxygen Diffusion Model for the Electric Pulse Induced Resistance Change Effect in Transition-Metal Oxides, *Physical Review Letters*, 98 (2007) 146403.
- [35] M. Huang, A.J. Tan, M. Mann, U. Bauer, R. Ouedraogo, G.S.D. Beach, Three-terminal resistive switch based on metal/metal oxide redox reactions, *Scientific Reports*, 7 (2017) 7452.



Chapter 6 Electrical control of the transport and magnetic properties in diluted magnetic oxide of $\text{Zn}_{0.92}\text{Mn}_{0.08}\text{O}$

6.1 Introduction

Electric-field manipulation of magnetism is being intensely investigated in various ways [1-3]. The most common approach is through the magnetoelectric effect [4, 5], in which the charge carriers of the FM are controlled by the electric-field driven interfacial coupling between FM and gating materials such as FE or dielectrics. Such kind of electric-field manipulation of magnetism involves the modulation of charge carrier density in FM through electrostatic means, by controlling the dipole polarization reversal of ferroelectric materials.

It has been demonstrated that the tunability of ferromagnetism is directly related to the carrier concentration of channel materials and the capacitance of dielectrics [6, 7]. Usually, the accumulation of a large carrier density ($<10^{14} \text{ cm}^{-2}$) in ferromagnetic material is difficult because large capacitance often requires a very high electric-field strength and thin dielectrics, which easily results in the dielectric breakdown. Electric double layer transistors (EDLTs) has become a convenient technique to overcome this problem, as it allows the change in carrier density up to 10^{15} cm^{-2} [8]. EDLTs use liquid electrolytes such that electric-field-induced rearrangement of cation and anions form a 1 nm-thick EDL to produce large surface charge changes on the ferromagnetic surfaces, reaching an electric-field strength up to 10 MV^{-1} that cannot be easily achieved by high- k dielectric materials [7, 9].

As alternatives to metallic ferromagnets, DMS draw much attentions as the magnetic spins and electrical charges strongly correlate with each other, which allow the field-induced coupling between spin and charge degrees of freedom [9, 10]. Therefore, DMS with FET geometry is one of the promising methods to study the electric-field manipulation of magnetism. Electric-field control of magnetism in DMS is more interesting than that of metallic ferromagnet, since the carrier density of metallic ferromagnets is much larger than those of DMS [2, 11]. Reports on DMS of (Ga,Mn)As demonstrated that T_C , magnetic anisotropy and magnetization can be manipulated by



electric field [12, 13]. However, since T_C of (Ga,Mn)As is ~ 190 K, room-temperature manipulation of ferromagnetism in DMS has yet to be demonstrated [14].

As one of the DMS, (Zn, Mn)O is a promising candidate for the next-generation spintronic devices [15-19] due to its high T_C above 300K [20]. As reported in previous studies, the enhancement of ferromagnetism of (Zn, Mn)O films can be achieved by either increasing the Mn or electron concentration through introduction of O_v .

Up to now, several attempts on the electric-field manipulation of magnetic properties in ZnO are mainly focused on films deposited on FE substrates [21], in which both polarization and strains are induced to the films through the substrates. Since the magnetic properties of ZnO are sensitive with several factors such as strain [22], crystal quality [23], O_v [19, 24] and interfacial diffusion [25], it is difficult to isolate the electrostatic effect from these piezoelectric substrates. Moreover, the growth of ZnO on FE substrates [21] implies the need to apply high voltages (in the order of kV) and is incompatible with typical device operations. On the contrary, IL gating process can be easily integrated on different types of DMS films without concern of epitaxy matching, and has the further advantage of reducing the switching voltage below 5 V [9, 26].

In this section, I deposit $\text{Zn}_{0.92}\text{Mn}_{0.08}\text{O}$ films on Al_2O_3 substrates and investigate the electric-field manipulation of magnetotransport and magnetism of the films through the IL top gating method. The experimental results indicate that not only low-temperature magnetotransport but also perpendicular magnetization can be manipulated by electric field. My results also demonstrate that the correlation between the carrier concentration and magnetic properties of $\text{Zn}_{0.92}\text{Mn}_{0.08}\text{O}$ films.

6.2 Experimental details

6.2.1 Thin film growth and device fabrication

10 nm-thick $\text{Zn}_{0.92}\text{Mn}_{0.08}\text{O}$ thin films were deposited on (0001) Al_2O_3 single-crystal substrates by PLD, from ceramic targets of $\text{Zn}_{0.92}\text{Mn}_{0.08}\text{O}$ with stoichiometric compositions. The growth of $\text{Zn}_{0.92}\text{Mn}_{0.08}\text{O}$ thin films were carried out at 300°C with a base pressure of 5×10^{-4} Pa or better, and then cooled down to room temperature at a rate of 5 K/min. The film thickness was controlled by the deposition time and further confirmed with XRR measurements.



To study the electric-field manipulation of $\text{Zn}_{0.92}\text{Mn}_{0.08}\text{O}$, the films were patterned into Hall-bar geometries (channel width :50 μm , channel length: 110 μm) by photolithography and wet etched using diluted HCl as etchants. Au (50 nm)/Ti (5 nm) coplanar electrodes for IL gate and contact electrodes for $\text{Zn}_{0.92}\text{Mn}_{0.08}\text{O}$ were prepared by electron beam evaporation, with a base pressure of 5×10^{-4} Pa.

A capping layer of 2 nm-thick SiO_2 film was deposited by electron beam evaporation at 300 K, in order to prevent the direct contact between the IL and $\text{Zn}_{0.92}\text{Mn}_{0.08}\text{O}$ film. Prior to the gating, IL was baked at 80°C in a vacuum chamber to get rid of any water contamination. A droplet of IL was placed on the top of the film and served as the top gate electrode. The device was then immediately cooled down to 230 K for the gating process. By applying different V_g (-2 V, 0 V and 2 V), the accumulated and depleted charge carrier sin the channel surface would appear and become stable for one hour in the gating process. Then the device was immediately cooled down to 180 K, which is below the freezing point of IL (~ 210 K). Once the temperature reached 180 K, the V_g was removed. After the transport measurements, the device was heated up to 230 K for changing the V_g .

6.2.2 Structural characterization

XRD and XRR measurements were conducted using a high-resolution Rigkua Smartlab diffractometer with Cu- K_α radiation ($\lambda = 1.5406 \text{ \AA}$). XPS was performed with a Sengyang SKL-12 electron spectrometer equipped with a VG CLAM 4 MCD electron energy analyzer and twin anodes of Mg K_α radiation (1253.6 eV) or Al K_α radiation (1496.3 eV) X-ray sources. The base pressure for the XPS measurement was about 2×10^{-9} Torr. All binding energies in this work were calibrated with the C 1s peak (284.6 eV). Before performing XPS measurement, the samples were washed with acetone and isopropyl alcohol to remove the IL.

6.2.3 Transport characterization

Transport measurements, including MR (out-of-plane) and $R_{xx}-T$ measurement, were carried out in a PPMS through the standard four-point probe method. Different magnitudes of V_g were applied at 230 K through a Keithley 2400 for one hour, in order to stabilize the EDL inside IL. Then the sample was cooled down to 180 K, and V_g was removed once the temperature was reached. AHE of $\text{Zn}_{0.92}\text{Mn}_{0.08}\text{O}$ devices with different



magnitudes of V_g was measured by a Keithley 2182A nanovoltmeter and a 6221 AC/DC current source.

6.3 Results and discussions

6.3.1 Structural characterization

The crystal orientation and the phase purity of $\text{Zn}_{0.92}\text{Mn}_{0.08}\text{O}$ were characterized by XRD θ - 2θ scans (Figure 6. 1). Apart from the (0002) ZnO diffraction peak, no secondary phase of MnO or Mn_2O_3 is found. This implies the $\text{Zn}_{0.92}\text{Mn}_{0.08}\text{O}$ film has a high phase purity of hexagonal wurtzite structure, and all Mn ions are embedded into ZnO lattice without any segregation. The rocking curve of the (0002) $\text{Zn}_{0.92}\text{Mn}_{0.08}\text{O}$ diffraction peak (inset of Figure 6. 1) has a FWHM of 0.1° and is comparable with that of (0006) Al_2O_3 substrate peak (0.1°), implying that the $\text{Zn}_{0.92}\text{Mn}_{0.08}\text{O}$ film possesses high crystal quality.

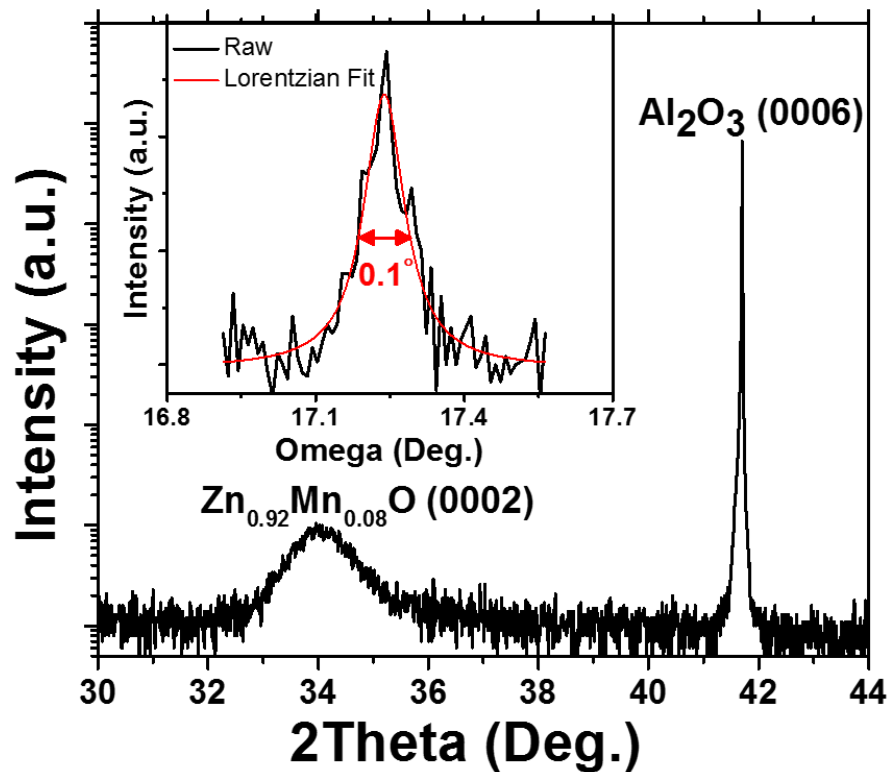


Figure 6. 1 XRD θ - 2θ scan for the $\text{Zn}_{0.92}\text{Mn}_{0.08}\text{O}/\text{Al}_2\text{O}_3$. Inset: rocking curve of (0002) $\text{Zn}_{0.92}\text{Mn}_{0.08}\text{O}$ diffraction peak.

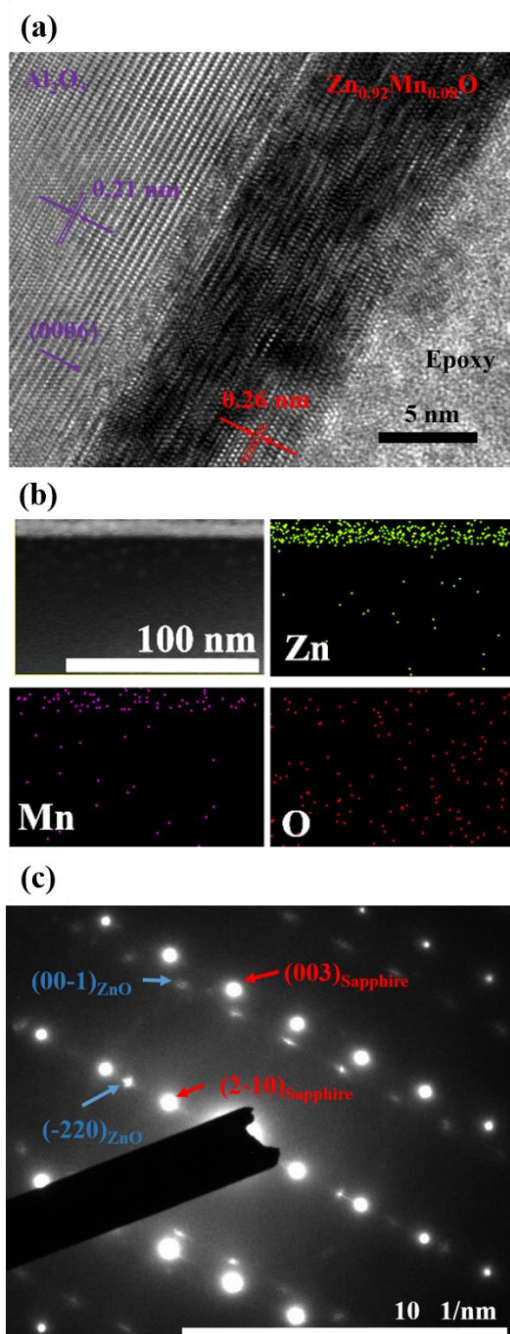


Figure 6. 2 (a) High-resolution cross-sectional TEM image of the $Zn_{0.92}Mn_{0.08}O/Al_2O_3$, the d -spacing of $Zn_{0.92}Mn_{0.08}O$ and Al_2O_3 are 0.26 and 0.21 nm respectively. (b) The elemental distribution Zn, Mn and O for the $Zn_{0.92}Mn_{0.08}O$ as examined by elemental mapping in TEM. (c) SAED pattern on the interfaces of ZnO/Al_2O_3 , which is taken at $(0001) Al_2O_3$.

Cross-sectional TEM was employed to study the quality of films and the possible existence of manganese or manganese oxide clustering. Figure 6. 2 (a) depicts the high resolution TEM image of $Zn_{0.92}Mn_{0.08}O$ film. The 10-nm thick film exhibits epitaxy with respect to the sapphire substrate and an atomically sharp interface without any interfacial



reactions. The distance between neighboring $Zn_{0.92}Mn_{0.08}O$ and Al_2O_3 atomic planes was found to be 0.26 nm and 0.21 nm, in correspondence with the crystal plane of (0002) ZnO and (0006) Al_2O_3 . No Mn metal cluster or other crystal phase was found upon inspection by HRTEM at several locations, and it was concluded that single-phased $Zn_{0.92}Mn_{0.08}O$ was obtained and the Mn ions were homogeneously dissolved in the ZnO lattice. Moreover, elemental mapping of these films (Figure 6. 2 (b)) indicates that the Mn ions are uniformly dissolved into ZnO lattice, further confirming that the films are single-phased without any Mn segregation. Figure 6. 2 (c) shows the selected area electron diffraction (SAED) pattern at the interfaces of $Zn_{0.92}Mn_{0.08}O/Al_2O_3$. Apart from the crystal planes of $Zn_{0.92}Mn_{0.08}O$ and Al_2O_3 , no any secondary phase can be found in these SAED pattern. The above structural characterizations confirmed the $Zn_{0.92}Mn_{0.08}O$ film is single-phased, and with good crystal quality and an atomically sharp interface.

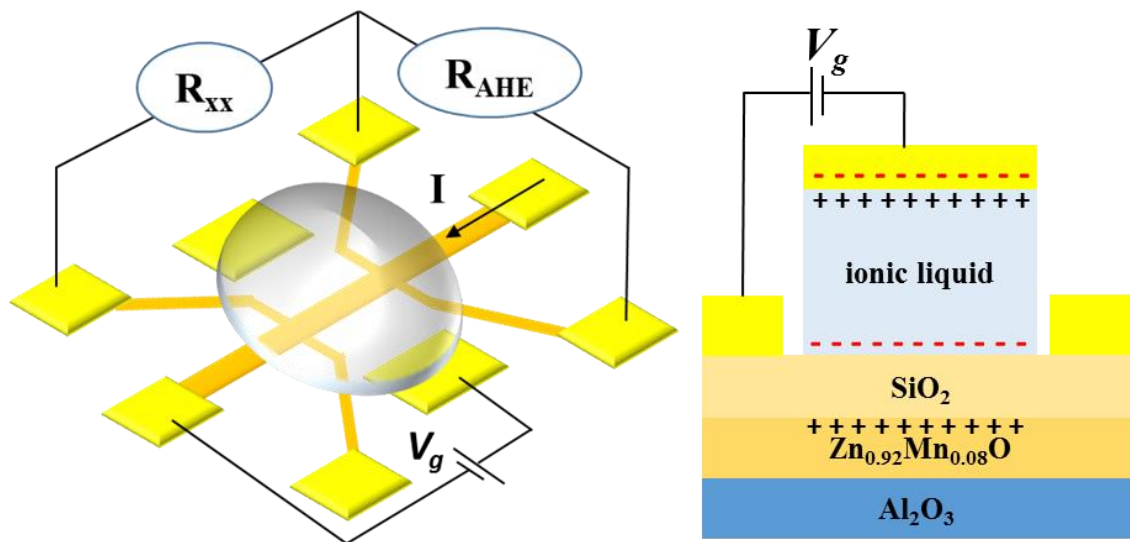


Figure 6. 3 Schematics diagram of $Zn_{0.92}Mn_{0.08}O$ device with Hall-bar pattern and IL as electrolyte.

6.3.2 Transport characterization

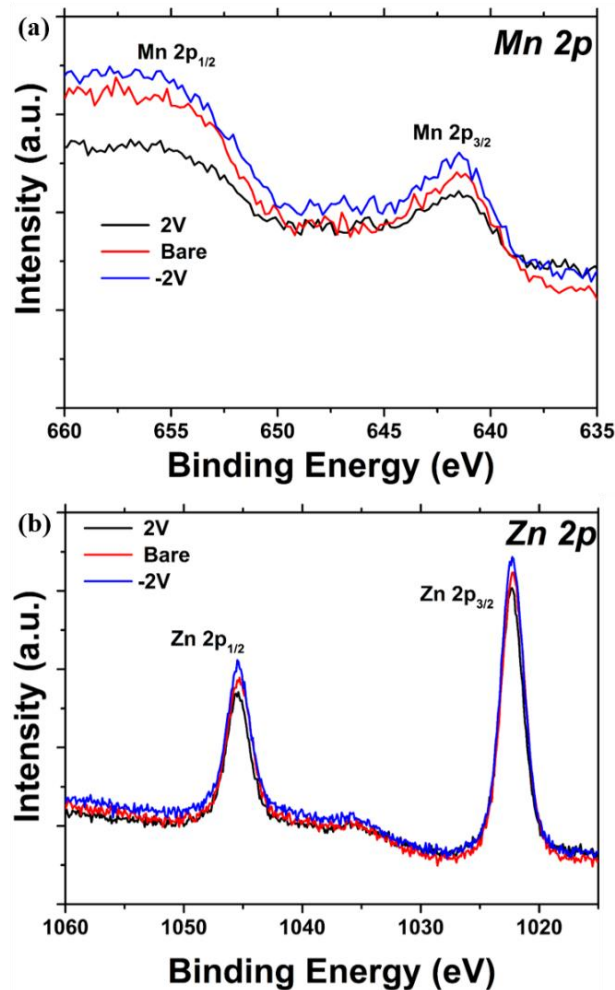


Figure 6. 4 (a) XPS core-level spectra of $\text{Zn}_{0.92}\text{Mn}_{0.08}\text{O}$, showing binding energies of (a) Mn 2p and (b) Zn 2p. Legends indicate the application of different V_g of -2, 0 and 2 V in 230 K for 1 hour before measurements.

To form the planar EDLT device (Figure 6. 3), 10 nm-thick $\text{Zn}_{0.92}\text{Mn}_{0.08}\text{O}$ films were patterned into Hall bars (channel width :50 μm , channel length: 110 μm) by wet etching, followed by electron beam evaporation of Ti (5nm)/ Au (50nm) as ZnO channel and gate electrodes. Before investigating the electric-field dependent of the transport properties in $\text{Zn}_{0.92}\text{Mn}_{0.08}\text{O}$, XPS was used to understand the chemical states and composition of the $\text{Zn}_{0.92}\text{Mn}_{0.08}\text{O}$ films. In Figure 6. 4 (a), the film gated with 0 V shows a double spectra of 641.19 eV and 655.48 eV at the core level spectrum of Mn 2p regions, indicating Mn ions are present as Mn^{2+} [27, 28]. In Figure 6. 4 (b), the core level spectrum of ZnO 2p regions shows two spectra lines at 1022 eV and 1045 eV, corresponding to Zn^{2+} 2p level of 2p_{3/2} and 2p_{1/2} respectively [27, 28]. It indicates that chemical state of Zn^{2+} is predominantly present in the sample.

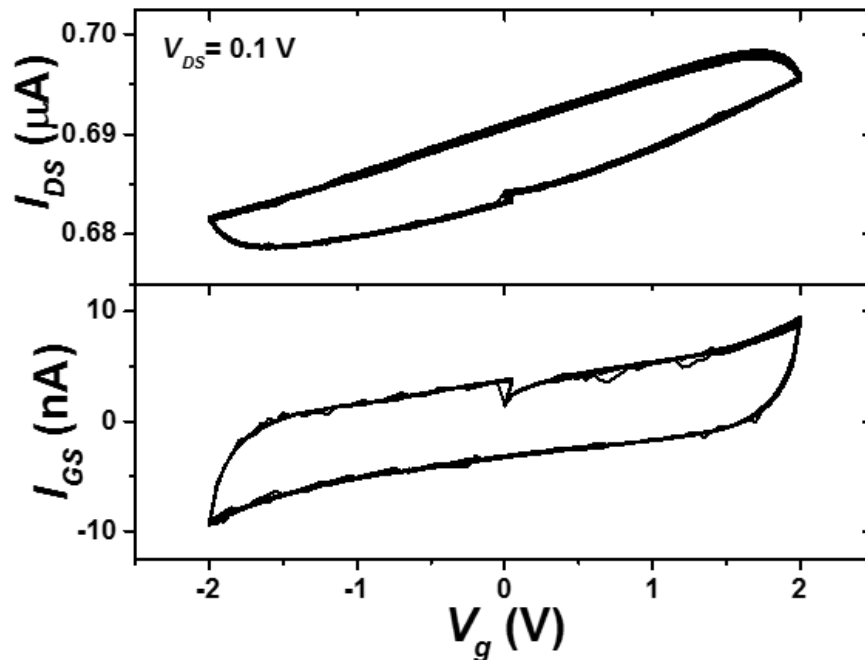


Figure 6. 5 Upper panel: $I_{DS}(V_g)$ measurement of $\text{Zn}_{0.92}\text{Mn}_{0.08}\text{O}$ using a scan rate of 100 mV/s, the curve corresponds to 50 consecutive $I(V)$ measurement. Lower panel is the corresponding leakage current across the $\text{Zn}_{0.92}\text{Mn}_{0.08}\text{O}$ EDLT.

The electric-field control of charge carrier accumulation and depletion was achieved by applying V_g to control the movement of cations and anions. By controlling the V_g , an EDL was formed over the surface to manipulate the depleted and accumulated states in the $\text{Zn}_{0.92}\text{Mn}_{0.08}\text{O}$ channel. The freezing point of IL used is about 210 K, so the EDL would be frozen after V_g is removed following the poling procedures as described in Section 6.2.1 [29]. Moreover, coplanar electrodes for IL gating were placed close to the $\text{Zn}_{0.92}\text{Mn}_{0.02}\text{O}$ channel in order to provide a strong electric-field effect. Although the deposition of 2 nm-thick SiO_2 film on the $\text{Zn}_{0.92}\text{Mn}_{0.02}\text{O}$ EDLT will reduce the electric-field effect, the generated effect was still larger than conventional high- k dielectric materials such as Al_2O_3 , HfO_2 and ZrO_2 [6].

To investigate the electric-field dependence of transport properties in ZnO EDLTs, Figure 6. 5 shows the V_g dependence of drain-source current (I_{DS}) of $\text{Zn}_{0.92}\text{Mn}_{0.08}\text{O}$ EDLT with 50 consecutive cycles, using a drain-source voltage (V_{DS}) = 100 mV. These results were collected at 230 K, at which the electrochemical reaction between $\text{Zn}_{0.92}\text{Mn}_{0.08}\text{O}$ and IL was suppressed while the ionic mobility of IL was enough to accumulate or deplete the electron charge carrier in the $\text{Zn}_{0.92}\text{Mn}_{0.08}\text{O}$ EDLTs. The $I_{DS}(V_g)$ characteristic (upper panel, Figure 6. 5 (a)) features typical behaviour of EDL capacitance with symmetric and



rectangular shapes without irreversible redox peaks, and highly repeatability between the 1st and the 50th cycles. These findings indicate that $I_{DS}(V_g)$ measurement is dominated by electrostatic doping [30].

To further prove the possibility of electrostatic reaction in $\text{Zn}_{0.92}\text{Mn}_{0.08}\text{O}$ EDLT, the bottom panel of Figure 6. 5 depicts the leakage current (I_{GS}) across the gate electrode. The leakage current recorded during the $I_{DS}(V_g)$ measurement is in the nA range, which is two order magnitude smaller than I_{DS} . This indicates that the modulation of I_{DS} under V_g bias are not due to the leakage current. Moreover, both $I_{DS}(V_g)$ and $I_{GS}(V_g)$ measurements show that the modulation of $\text{Zn}_{0.92}\text{Mn}_{0.08}\text{O}$ EDLT is reproducible and without any drifting of the I_{GS} and I_{DS} due to prolonged degradation arising from the presence of IL. The results suggest that electrochemical effect due to IL gating is not likely to happen in the experiment.

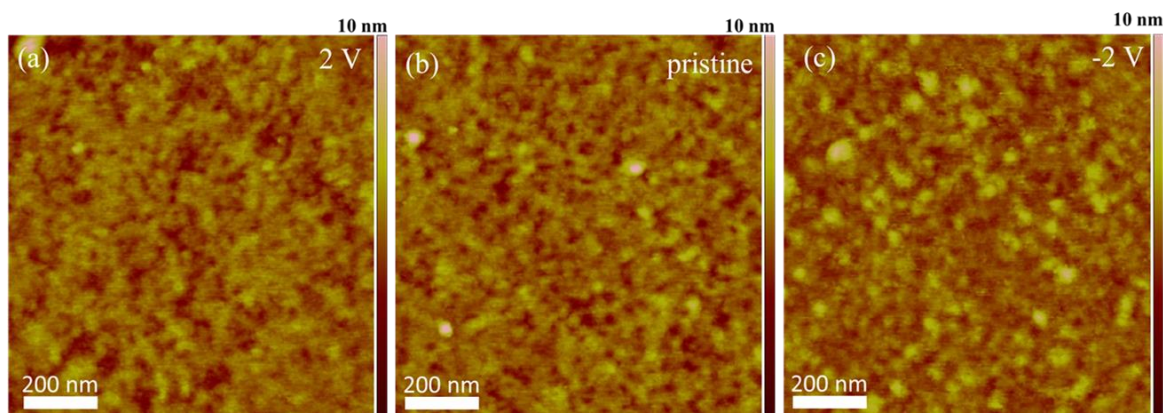


Figure 6. 6 AFM surface topography of $\text{Zn}_{0.92}\text{Mn}_{0.08}\text{O}$ EDLT with different V_g . The root mean square roughness for the samples are: (a) 0.64 nm, (b) 0.65 nm and (c) 0.66 nm.

Apart from the $I_{DS}(V_g)$ measurements, the possibility of electrochemical reactions between IL and ZnO channel was further investigated through measuring the valence change of elements (Mn and Zn), as well as potential surface morphology variations induced by the gating process. XPS spectra of pristine sample, as well as those gated with $V_g = -2\text{V}$ or 2V IL at 230 K for 1 hour, are shown in Figure 6. 4 (a)-(b). Noting that migration of cations and anions in IL is a dynamic process, a reasonable time is required for the formation of stable EDL layer under a fixed V_g . The Zn 2p and Mn 2p core-level spectra show no apparent change in the shape and peak values, indicating no valence change in Mn, Zn and O upon gating with different V_g . This implies that the IL gating effect on ZnO channel is an electrostatic one with volatile behaviour. On the other hand,



after removal of the IL by isopropyl alcohol, AFM images (Figure 6. 6) gated with different V_g show similar surface morphologies (r.m.s roughness: 0.64 nm (2V), 0.65 nm (pristine) and 0.66 nm (-2V), further suggesting the non-electrochemical nature of the observed changes in Zn_{0.92}Mn_{0.08}O after the gating process. The above measurements demonstrate the non-destructive nature of the IL gating process on ZnO samples studied.

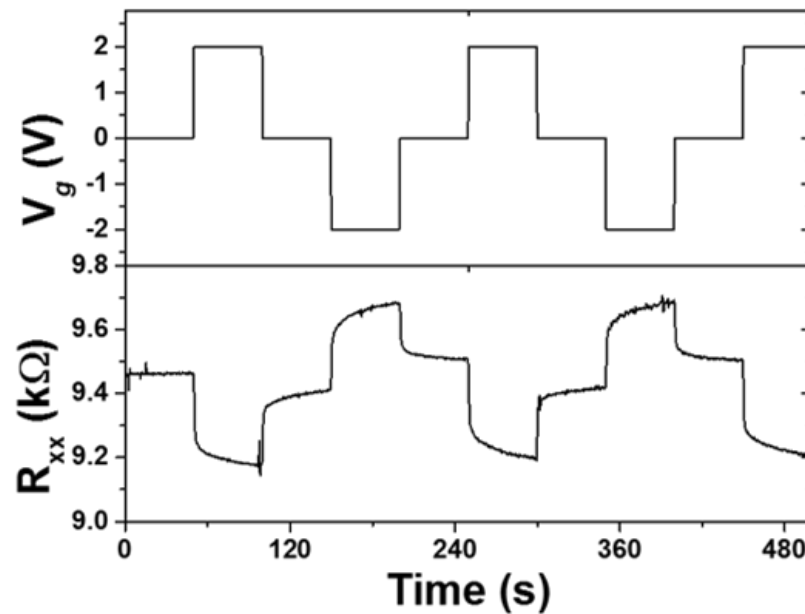


Figure 6. 7 R_{xx} -time curve with different V_g (2, 0, -2V).

After establishing the electrostatic nature of the resistance modulation of Zn_{0.92}Mn_{0.08}O, the transport properties of Zn_{0.92}Mn_{0.08}O EDLT were measured. Figure 6. 7 records the R_{xx} of Zn_{0.92}Mn_{0.08}O EDLT as a function of time, by applying alternating V_g of 2, 0 and -2 V at 230 K and measuring R_{xx} at the same temperature. R_{xx} decreases sharply upon the application of $V_g = 2$ V, which is consistent with injection of electrons at the ZnO surface. When V_g is set to 0 V, the modulation of R_{xx} disappears, although a slightly decrease in R_{xx} is observed as compared with the pristine state. On the contrary, a sharp increase in R_{xx} is achieved when applying a V_g of -2V, which is consistent with the scenario for the depletion of electrons at SiO₂/Zn_{0.92}Mn_{0.08}O interface. We note that the modulation of R_{xx} cannot reach a steady value: considering that the migration of IL is a slow process, it requires 10-30 mins to form a stable EDL upon applying V_g [29]. Moreover, R_{xx} cannot return to the original values, since the external electric field is required to alter the direction of EDL [29]. The influence of I_{GS} is negligible since the I_{DS} is higher than I_{GS} by two order of magnitude.

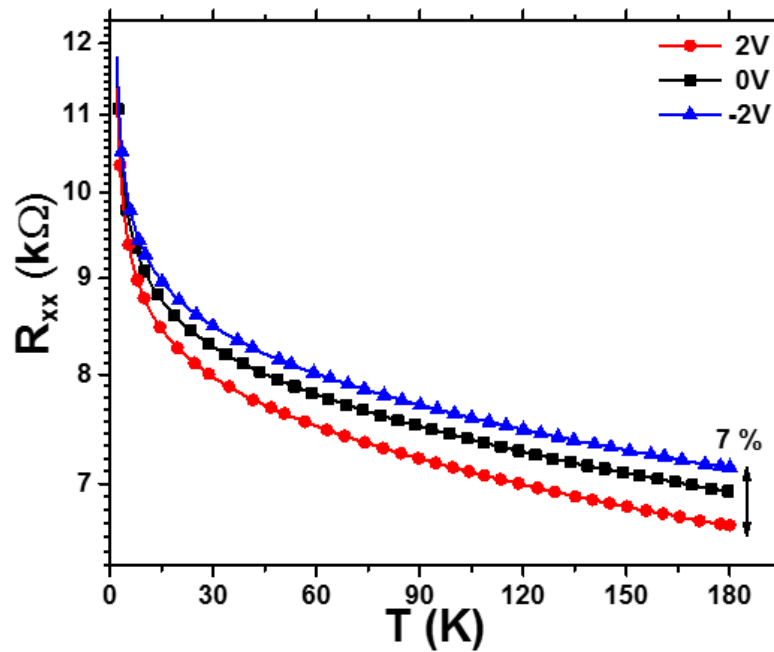


Figure 6. 8 R_{xx} - T of R_{xx} in $\text{Zn}_{0.92}\text{Mn}_{0.08}\text{O}$ EDLT for $V_g = -2$ (blue triangles), 0 (black squares) and 2 V (red circles).

R_{xx} - T measurements were also performed. Firstly, V_g was applied at 230 K for 1 hour for the charging process, followed by cooling the device to 180 K with the same V_g . Figure 6. 8 depicts the R_{xx} - T measurement of $\text{Zn}_{0.92}\text{Mn}_{0.08}\text{O}$ EDLT for $V_g = -2, 0$ and 2 V. All measurements indicate semiconducting behaviour, showing an increase in R_{xx} as T decreases. As V_g increases from -2 V to 2 V, R_{xx} of $\text{Zn}_{0.92}\text{Mn}_{0.08}\text{O}$ shows a decrease by 7% at 180 K, which could be understood as the consequence of electron accumulation at the $\text{SiO}_2/\text{Zn}_{0.92}\text{Mn}_{0.08}\text{O}$ interface.

The temperature dependence of ρ_{xx} , n and μ_e of $\text{Zn}_{0.92}\text{Mn}_{0.08}\text{O}$ EDLT were further examined using Hall effect measurements (Figure 6. 9). Negative Hall coefficients of the samples reveal that the conduction is due to electron-doping of $\text{Zn}_{0.92}\text{Mn}_{0.08}\text{O}$ devices, and can be attributed to the excess of O_v inside the $\text{Zn}_{0.92}\text{Mn}_{0.08}\text{O}$ channel. Clearly, high and low levels of ρ_{xx} and n are observed for the whole temperature range with different V_g , indicating that accumulation and depletion of electron carriers by IL are responsible for the significant modulation in R_{xx} . Moreover, ρ_{xx} , n and μ_e at different V_g show strong temperature dependences, indicating that the semiconducting behaviour is still dominant. The slight decrease in n from 180 to 20 K is mainly attributed the frozen charge carriers at low temperatures [18]. However, it is noted that the μ_e dependence on temperature for



$V_g = \pm 2$ V overlap with one another, suggesting no obvious relationship between μ_e and V_g in the $\text{Zn}_{0.92}\text{Mn}_{0.08}\text{O}$ EDLT.

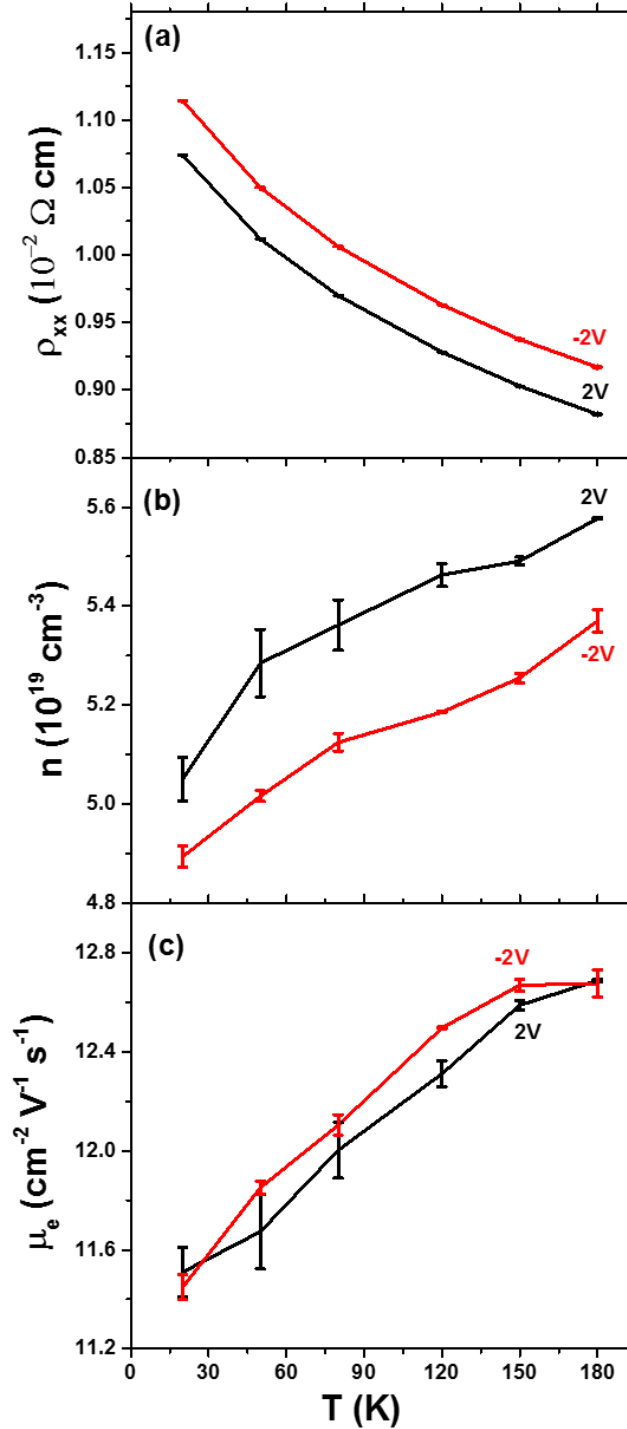


Figure 6. 9 Temperature dependences of various Hall measurement parameters in $\text{Zn}_{0.92}\text{Mn}_{0.08}\text{O}$ EDLT for $V_g = -2$ and 2 V: ρ (a), n (b) and μ_e (c).



6.3.2 Magnetic characterization

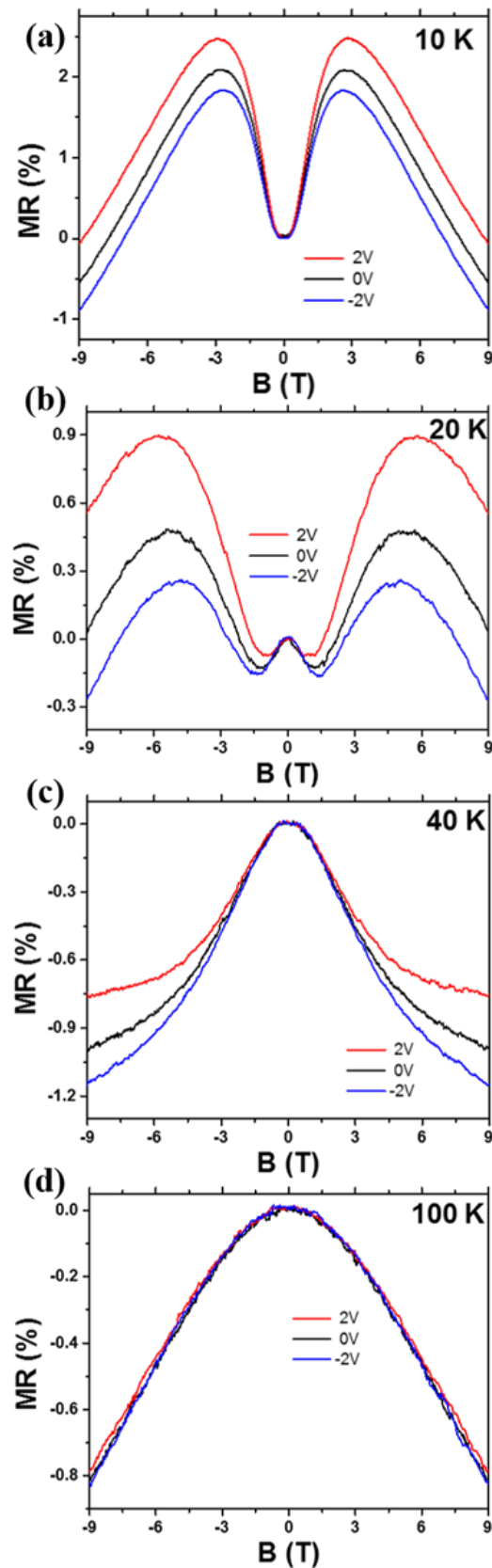


Figure 6. 10 MR of $\text{Zn}_{0.92}\text{Mn}_{0.08}\text{O}$ EDLT for different V_g at 10 K (a), 20 K (b), 40 K (c) and 100 K (d).



Magnetotransport measurement is a tool to understand the interaction between Mn impurity ions and the ZnO lattices, since the Mn ions can contribute to the interaction between the localized spins and electron carriers in ZnO lattices [31]. Figure 6. 10 show the MR of Zn_{0.92}Mn_{0.08}O EDLT under different V_g (-2, 0 and 2 V) and temperatures, with the magnetic field applied in the out-of-plane direction. Here $MR=(R_{xx}(H)-R_{xx}(0))/R_{xx}(0)$, where $R_{xx}(H)$ and $R_{xx}(0)$ are the R_{xx} values in external field H and without external magnetic field, respectively. At 10 and 20 K, the device shows a transition from a positive-MR behavior at low-field regime (3 T at 10 K, and 3-6 T at 20 K) to a negative-MR at large magnetic fields (~9 T). On the other hand, only negative-MR can be observed at higher temperatures (40 K and 100 K).

The opposite MR signs originate from different magnetic-field transport behavior. Positive MR originates from spin-splitting of conduction band induced by s - d exchange interaction in the DMS (spin-dependent scattering) [15, 17], leading to an increase in MR. On the other hand, negative MR is due to the exchange interaction between Mn^{2+} and O_v , which is the so-called magnetic polarons [18]. The interaction between O_v -Mn complexes would form random orientation of magnetic polarons (AF). As the temperature decreases, these random orientations of magnetic polarons start to freeze out. A large magnetic field is required to align these magnetic polarons along the same direction. As a result, a significant drop in MR is found in the DMS. As the interaction between $Mn-O_v$ -Mn will be ferromagnetic, the overlap of these neighboring bound magnetic polarons formed a long-range FM interaction.

Moreover, MR could be modulated by applying different V_g . At 10 K (Figure 6. 10), the device exhibits positive-MR at around 3 T and negative-MR at 9 T. The peak positive MR increases from 1.83 to 2.47% and the negative-MR (measured at 9 T) decreases from -0.047 to -0.87% when the V_g increased from -2 to 2 V.

Comparing MR values for different V_g , an increase in positive-MR and decrease in the absolute negative-MR is applicable for all measurement temperatures in relation to the increase in carrier concentration, as V_g is set from -2 to 2 V. As predicted by the impurity-band exchange model for carrier-mediated ferromagnetism in DMS, the increase in electron concentration leads to the short distance between neighboring Mn sites assisting the overall overlapping chance of the neighboring bound magnetic polarons. Such an increase in carrier concentration would decrease the overall content of AF interaction



between Mn- O_v complex, and lead the increase in FM interaction [15, 32]. Therefore, the observed magnetotransport behaviour is consistent with carrier-mediated ferromagnetism model.

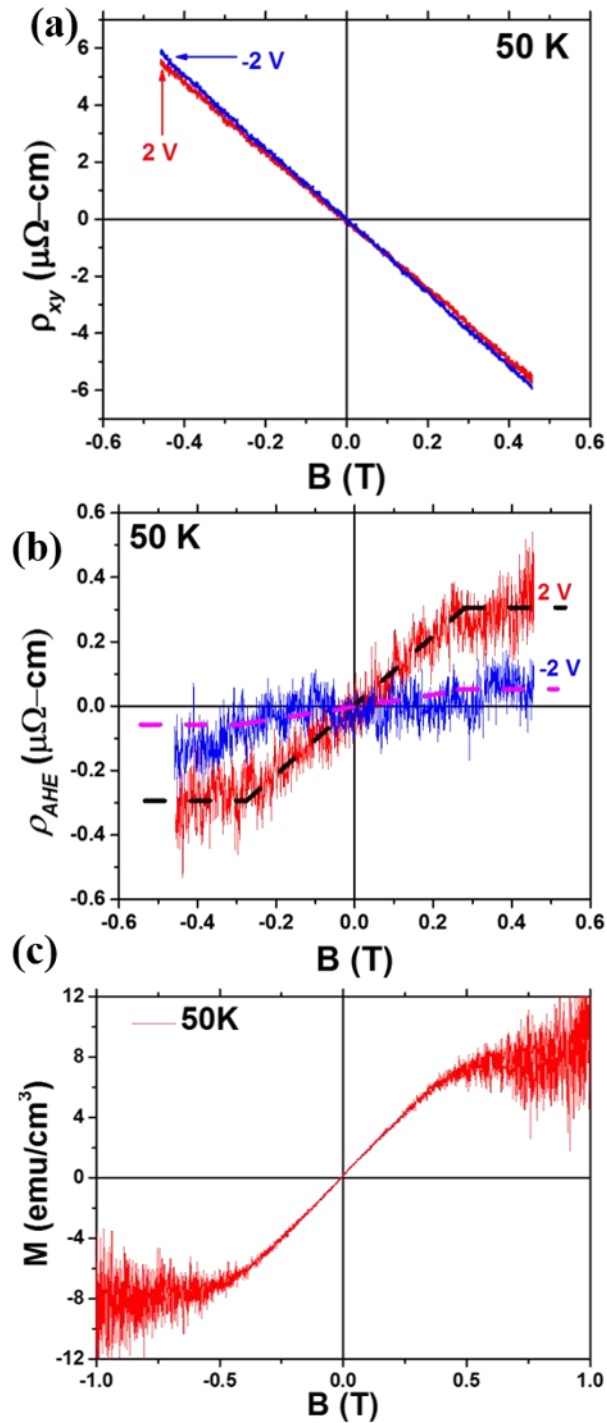


Figure 6. 11 (a) Hall resistivity of 10-nm thick $Zn_{0.92}Mn_{0.08}O$ EDLTs measured at 50 K as a function of magnetic field. (b) AHE after subtracting the linear contribution from ordinary Hall resistivity. Dashed lines are guides to the eye. (c) Hysteresis loop of a 250 nm-thick $Zn_{0.92}Mn_{0.08}O$ film at 50 K.



AHE was also employed to study the changes in ferromagnetic properties under electric gating through IL, since R_{AHE} is proportional to the perpendicular component of magnetization [33]. Figure 6. 11 (a) shows the ρ_{xy} as a function of out-of-plane magnetic field at 50 K. In ferromagnetic materials, the ρ_{xy} consists of two contributions that can be expressed as follows [33]:

$$\rho_{xy} = \rho_{OHE} + \rho_{AHE}$$

where ρ_{OHE} and ρ_{AHE} are the ordinary and anomalous Hall contributions originate from the Lorentz force acting on the charge carrier and magnetization of DMS respectively. ρ_{xy} as obtained from the slope of Figure 6. 11 (a) yields an electron concentration of $4.92 \times 10^{19} \text{ cm}^{-3}$ and $5.19 \times 10^{19} \text{ cm}^{-3}$ at $V_g = -2$ and 2 V , respectively; the increases in carrier concentration with $V_g = 2 \text{ V}$ is consistent with previous results. The correlation between ρ_{AHE} and V_g is a direct evidence to prove the existence of interaction between carrier concentration and ferromagnetism in Zn_{0.92}Mn_{0.08}O. As depicted in Figure 6. 11 (b), after subtracting the linear contribution from ρ_{OHE} , ρ_{AHE} increases from 0.1 to $0.3 \mu\Omega\text{cm}$ upon the application of V_g of -2 and 2 V , indicating that the increases in carrier concentration is accompanied by the increase in ferromagnetism of Zn_{0.92}Mn_{0.08}O. The enhanced ρ_{AHE} is therefore a key evidence to prove that the carrier concentration can increase the exchange interaction between conduction electrons and localized spin of magnetic impurities [34].

Figure 6. 11 (c) show the M-H curve of 250 nm-thick Zn_{0.92}Mn_{0.08}O films measured at 50 K. The strength of AHE can be understood by the comparison of anomalous Hall conductivity (σ_{AHE}) which can be expressed in this following equation [33]:

$$\sigma_{AHE} = \frac{\rho_{AHE}}{\rho_{xx}^2 + \rho_{AHE}^2}$$

where ρ_{xx}^2 is defined as the longitudinal resistivity of Zn_{0.92}Mn_{0.08}O devices at 50 K. The obtained σ_{AHE} with $V_g = 2$ and -2 V are 3×10^{-3} and $7.26 \times 10^{-4} \Omega^{-1}\text{cm}^{-1}$, comparable with the reported values of n -type Co doped TiO₂ [9].

The magnetotransport and AHE measurements reveal that the magnetic properties of Zn_{0.92}Mn_{0.08}O EDLT strongly correlates with the electron carrier concentration. The isovalent substitution of Mn²⁺ by Zn²⁺ into the ZnO lattice would not induce any spin-



polarized carriers in the $Zn_{0.92}Mn_{0.08}O$ [18]. The formation of spin-polarized electrons is due to the O_v in the $Zn_{0.92}Mn_{0.08}O$, while magnetic alignment is due to the $Mn^{2+} - O_v - Mn^{2+}$ interactions [18]. Upon switching V_g from 2 to -2 V, the conductivity and electron carrier concentration is increased, implying that more donor electrons can be introduced into $Zn_{0.92}Mn_{0.08}O$ via IL gating. In the negative MR (large field) regime, the increase in electron carrier concentration leads to increase the overlapping probability of each polaron ($Mn^{2+} - O_v - Mn^{2+}$), and causes a decreased contribution in the magnetic scattering due to paramagnetic states or the antiferromagnetic interaction mediated through O_v , as finally reflected from the increases in MR for high field regime [18]. The enhanced ρ_{AHE} with the switching V_g from -2 to 2 V is consistent with the accumulation of electron carriers, which increases the ferromagnetic interaction mediated through O_v [9].

6.4 Conclusion

In summary, the electric-field manipulation $Zn_{0.92}Mn_{0.08}O$ was reported, using IL as the top gate electrode. Structural characterization such as XPS and AFM measurements proved that the electrical modulation of $Zn_{0.92}Mn_{0.08}O$ were due to electrostatic effect from IL. Transfer curve measurements revealed a reversible modulation of R_{xx} at different V_g . In addition, electrical-field control of MR and AHE further revealed that the enhanced tunability of magnetotransport and ferromagnetism in $Zn_{0.92}Mn_{0.08}O$ was correlated with the increase in electron concentration via IL gating. This work provided a reversible approach towards manipulating the electrical and ferromagnetic properties in DMS via electric field, which would significantly contribute to the development of spintronic devices with low-power dissipation.



References for Chapter 6

- [1] C. Song, B. Cui, F. Li, X. Zhou, F. Pan, Recent progress in voltage control of magnetism: Materials, mechanisms, and performance, *Progress in Materials Science*, 87 (2017) 33-82.
- [2] F. Matsukura, Y. Tokura, H. Ohno, Control of magnetism by electric fields, *Nat. Nanotech*, 10 (2015) 209-220.
- [3] Q. Yang, Z. Zhou, N.X. Sun, M. Liu, Perspectives of voltage control for magnetic exchange bias in multiferroic heterostructures, *Physics Letters A*, 381 (2017) 1213-1222.
- [4] X. Hong, A. Posadas, A. Lin, C.H. Ahn, Ferroelectric-field-induced tuning of magnetism in the colossal magnetoresistive oxide La_{1-x}Sr_xMnO₃, *Physical Review B*, 68 (2003) 134415.
- [5] P. Borisov, A. Hochstrat, X. Chen, W. Kleemann, C. Binek, Magnetolectric Switching of Exchange Bias, *Physical Review Letters*, 94 (2005) 117203.
- [6] D. Chiba, T. Ono, Control of magnetism in Co by an electric field, *Journal of Physics D: Applied Physics*, 46 (2013) 213001.
- [7] M. Galiński, A. Lewandowski, I. Stępnia, Ionic liquids as electrolytes, *Electrochimica Acta*, 51 (2006) 5567-5580.
- [8] A.S. Dhoot, C. Israel, X. Moya, N.D. Mathur, R.H. Friend, Large Electric Field Effect in Electrolyte-Gated Manganites, *Physical Review Letters*, 102 (2009) 136402.
- [9] Y. Yamada, K. Ueno, T. Fukumura, H.T. Yuan, H. Shimotani, Y. Iwasa, L. Gu, S. Tsukimoto, Y. Ikuhara, M. Kawasaki, Electrically Induced Ferromagnetism at Room Temperature in Cobalt-Doped Titanium Dioxide, *Science*, 332 (2011) 1065-1067.
- [10] T. Zhao, S.R. Shinde, S.B. Ogale, H. Zheng, T. Venkatesan, R. Ramesh, S. Das Sarma, Electric Field Effect in Diluted Magnetic Insulator Anatase Co:TiO₂, *Physical Review Letters*, 94 (2005) 126601.
- [11] S. Cheng, C. Bin, P. Jingjing, M. Haijun, P. Feng, Electrical control of magnetism in oxides, *Chinese Physics B*, 25 (2016) 067502.
- [12] D. Chiba, A. Werpachowska, M. Endo, Y. Nishitani, F. Matsukura, T. Dietl, H. Ohno, Anomalous Hall Effect in Field-Effect Structures of (Ga,Mn)As, *Physical Review Letters*, 104 (2010) 106601.
- [13] P. Balestriere, T. Devolder, J. Wunderlich, C. Chappert, Electric field induced anisotropy modification in (Ga,Mn)As: A strategy for the precessional switching of the magnetization, *Applied Physics Letters*, 96 (2010) 142504.
- [14] D. Chiba, F. Matsukura, H. Ohno, Electric-field control of ferromagnetism in (Ga,Mn)As, *Applied Physics Letters*, 89 (2006) 162505.
- [15] L.-T. Chang, C.-Y. Wang, J. Tang, T. Nie, W. Jiang, C.-P. Chu, S. Arafin, L. He, M. Afsal, L.-J. Chen, K.L. Wang, Electric-Field Control of Ferromagnetism in Mn-Doped ZnO Nanowires, *Nano Letters*, 14 (2014) 1823-1829.
- [16] H.S. Hsu, C.P. Lin, H. Chou, J.C.A. Huang, Room temperature anomalous Hall effect in Co doped ZnO thin films in the semiconductor regime, *Applied Physics Letters*, 93 (2008) 142507.
- [17] K.R. Sapkota, W. Chen, F.S. Maloney, U. Poudyal, W. Wang, Magnetoresistance manipulation and sign reversal in Mn-doped ZnO nanowires, *Scientific Reports*, 6 (2016) 35036.
- [18] X.L. Wang, Q. Shao, A. Zhuravlyova, M. He, Y. Yi, R. Lortz, J.N. Wang, A. Ruotolo, Giant negative magnetoresistance in Manganese-substituted Zinc Oxide, *Scientific Reports*, 5 (2015) 9221.



- [19] Q. Shao, P.S. Ku, X.L. Wang, J.A. Zapien, C.W. Leung, F. Borgatti, A. Gambardella, V. Dediu, R. Ciprian, A. Ruotolo, Chemical states and ferromagnetism in heavily Mn-substituted zinc oxide thin films, *Journal of Applied Physics*, 115 (2014) 153902.
- [20] V.A. Coleman, C. Jagadish, Chapter 1 - Basic Properties and Applications of ZnO, *Zinc Oxide Bulk, Thin Films and Nanostructures*, Elsevier Science Ltd, Oxford, 2006, pp. 1-20.
- [21] Q.-X. Zhu, M.-M. Yang, M. Zheng, R.-K. Zheng, L.-J. Guo, Y. Wang, J.-X. Zhang, X.-M. Li, H.-S. Luo, X.-G. Li, Ultrahigh Tunability of Room Temperature Electronic Transport and Ferromagnetism in Dilute Magnetic Semiconductor and PMN-PT Single-Crystal-Based Field Effect Transistors via Electric Charge Mediation, *Advanced Functional Materials*, 25 (2015) 1111-1119.
- [22] C. Peng, Y. Wang, Z. Cheng, G. Zhang, C. Wang, G. Yang, Tuning magnetism by biaxial strain in native ZnO, *Physical Chemistry Chemical Physics*, 17 (2015) 16536-16544.
- [23] Y.H.L. G. Z. Xing, Y. F. Tian, J. B. Yi, C. C. Lim, Y. F. Li, G. P. Li, D. D. Wang, B. Yao, J. Ding, Y. P. Feng, and T. Wu, Defect-induced magnetism in undoped wide band gap oxides: Zinc vacancies in ZnO as an example, *AIP Advances*, 1 (2011) 022152.
- [24] X.L. Wang, K.H. Lai, A. Ruotolo, A comparative study on the ferromagnetic properties of undoped and Mn-doped ZnO, *Journal of Alloys and Compounds*, 542 (2012) 147-150.
- [25] Insights into the room temperature magnetism of ZnO / Co₃O₄ mixtures, *Journal of Applied Physics*, 103 (2008) 083905.
- [26] H. Ji, J. Wei, D. Natelson, Modulation of the Electrical Properties of VO₂ Nanobeams Using an Ionic Liquid as a Gating Medium, *Nano Letters*, 12 (2012) 2988-2992.
- [27] W.B. Mi, H.L. Bai, H. Liu, C.Q. Sun, Microstructure, magnetic, and optical properties of sputtered Mn-doped ZnO films with high-temperature ferromagnetism, *Journal of Applied Physics*, 101 (2007) 023904.
- [28] L.W. Yang, X.L. Wu, G.S. Huang, T. Qiu, Y.M. Yang, In situ synthesis of Mn-doped ZnO multileg nanostructures and Mn-related Raman vibration, *Journal of Applied Physics*, 97 (2005) 014308.
- [29] Y. Wang, X. Zhou, C. Song, Y. Yan, S. Zhou, G. Wang, C. Chen, F. Zeng, F. Pan, Electrical Control of the Exchange Spring in Antiferromagnetic Metals, *Advanced Materials*, 27 (2015) 3196-3201.
- [30] A. Molinari, P.M. Leufke, C. Reitz, S. Dasgupta, R. Witte, R. Kruk, H. Hahn, Hybrid supercapacitors for reversible control of magnetism, 8 (2017) 15339.
- [31] T. Fukumura, Z. Jin, A. Ohtomo, H. Koinuma, M. Kawasaki, An oxide-diluted magnetic semiconductor: Mn-doped ZnO, *Applied Physics Letters*, 75 (1999) 3366-3368.
- [32] J.M.D. Coey, M. Venkatesan, C.B. Fitzgerald, Donor impurity band exchange in dilute ferromagnetic oxides, *Nat Mater*, 4 (2005) 173-179.
- [33] N. Nagaosa, J. Sinova, S. Onoda, A.H. MacDonald, N.P. Ong, Anomalous Hall effect, *Reviews of Modern Physics*, 82 (2010) 1539-1592.
- [34] S.-J. Han, J.W. Song, C.-H. Yang, S.H. Park, J.-H. Park, Y.H. Jeong, K.W. Rhie, A key to room-temperature ferromagnetism in Fe-doped ZnO: Cu, *Applied Physics Letters*, 81 (2002) 4212-4214.



Chapter 7 Conclusions and future work

7.1 Summary of results

In this thesis, different methods for achieving the electric-field manipulation of magnetism in LSMO and $\text{Zn}_{0.92}\text{Mn}_{0.08}\text{O}$ devices were studied. In particular, O_v modulation in LSMO and electrostatic gating of $\text{Zn}_{0.92}\text{Mn}_{0.08}\text{O}$ have demonstrated potential in the development of electric-field-driven memory devices. This work can be concluded as follows:

1. Ferroelectric-driven manipulation of transport and magnetic properties of ultrathin LSMO FET was studied. The results suggested that upon the application of electric field, the polarization direction of P(VDF-TrFE) could be reversed, which in turn led to a 15% change LSMO R_{xx} at 300K. Besides, results of such heterostructures showed insignificant changes of T_C upon the reversal of P(VDF-TrFE), implying that the electric-field effect provided from P(VDF-TrFE) polarization was too weak for the purpose.
2. Electric-field-induced O_v modulation of ultrathin LSMO epitaxial films, through the application of low-voltage pulses across P(VDF-TrFE) top gate dielectric layer, was presented. Results from XPS measurements and switching tests in different gas environment revealed that the low-voltage-pulsing method favored the O_v creation (annihilation), as positive (negative) V_g pulses were applied in vacuum (oxygen environment). Upon the application of multiple low-positive-voltage pulses, O_v were created, resulting in the decrease in LSMO T_C from 280 to 265 K. This corresponded to a change in carrier concentration by 7 %. Successive switching cycles in the T_C and MR at 20 K implied that the O_v can be manipulated through the pulsed voltage with different signs and pulse cycles. These results also demonstrated that electrochemical reaction in LSMO channel offered a higher tunability in the T_C of LSMO, comparing with the measurement results obtained from the ferroelectric reversal in P(VDF-TrFE). Such a controllable O_v in LSMO through the application of low-voltage-pulses offered a promising route to enhance the transport and magnetic properties of transition metal oxides.



3. The final work was about the electric-field manipulation of $\text{Zn}_{0.92}\text{Mn}_{0.08}\text{O}$ thin films using IL as the top gate electrode. XPS and AFM measurements provided evidence that electrolyte gating in $\text{Zn}_{0.92}\text{Mn}_{0.08}\text{O}$ thin films were electrostatic in nature. Enhancement of negative MR in the low-temperature regime and perpendicular magnetization components through the AHE measurements were achieved, as a results of the increase in carrier concentration via the accumulated electrons towards the $\text{SiO}_2/\text{Zn}_{0.92}\text{Mn}_{0.08}\text{O}$ interface. These results demonstrated that the electrostatic gating effect was a promising method to manipulate the magnetic properties of DMS.

7.2 Future directions

Beside investigating FM, electric-field-induced magnetism in multilayered devices have also attracted lots of attention [1]. For example, previous studies of AF faced significant challenges due to lack of techniques to probe its magnetic behavior [2-5]. Until recently, the magnetism of AF would be probed through the adjacent FM. Such an interfacial coupling between AF and FM, otherwise known as EB, would cause the shift of hysteresis loop and also enhanced coercivity [6].

Based on the presented achievements of electric-field-induced- O_v creation/annihilation in the LSMO channel [7], one could extend the work to investigate the electric-field-control EB in the epitaxial heterostructure of manganites, using LSMO as FM and SrMnO_3 , LaMnO_3 or BiFeO_3 as AF. These perovskites possess good lattice matching and allows epitaxial growth of corresponding multilayers. Through IL gating methods, the high change of carrier density doping could induce the variation of magnetism in AF layer, which could induce the change in magnetization and Neel temperature in AF layer. The IL-gating process can achieve strong carrier concentration manipulation, leading to enhanced changes of magnetism and allows one to explore new phenomena at the interfacial level.

**References for Chapter 7**

- [1] V. Baltz, A. Manchon, M. Tsoi, T. Moriyama, T. Ono, Y. Tserkovnyak, Antiferromagnetic spintronics, *Reviews of Modern Physics*, 90 (2018) 015005.
- [2] V. Laukhin, V. Skumryev, X. Martí, D. Hrabovsky, F. Sánchez, M.V. García-Cuenca, C. Ferrater, M. Varela, U. Lüders, J.F. Bobo, J. Fontcuberta, Electric-Field Control of Exchange Bias in Multiferroic Epitaxial Heterostructures, *Physical Review Letters*, 97 (2006) 227201.
- [3] Y. Wang, X. Zhou, C. Song, Y. Yan, S. Zhou, G. Wang, C. Chen, F. Zeng, F. Pan, Electrical Control of the Exchange Spring in Antiferromagnetic Metals, *Advanced Materials*, 27 (2015) 3196-3201.
- [4] P. Borisov, A. Hochstrat, X. Chen, W. Kleemann, C. Binek, Magnetoelectric Switching of Exchange Bias, *Physical Review Letters*, 94 (2005) 117203.
- [5] S.M. Wu, S.A. Cybart, P. Yu, M.D. Rossell, J.X. Zhang, R. Ramesh, R.C. Dynes, Reversible electric control of exchange bias in a multiferroic field-effect device, *Nat. Mater.*, 9 (2010) 756-761.
- [6] S.M. Wu, S.A. Cybart, D. Yi, J.M. Parker, R. Ramesh, R.C. Dynes, Full Electric Control of Exchange Bias, *Physical Review Letters*, 110 (2013) 067202.
- [7] H.F. Wong, S.M. Ng, W.F. Cheng, Y. Liu, X. Chen, D. von Nordheim, C.L. Mak, J. Dai, B. Ploss, C.W. Leung, Enhanced tunability of electrical and magnetic properties in (La,Sr)MnO₃ thin films via field-assisted oxygen vacancy modulation, *Solid-State Electron.*, 138 (2017) 56-61.